1-1-2010

Visualisation of flow pattern and measurement of liquid distribution in a random packed column using electrical resistance tomography (ERT)

Nazar Aoda
Ryerson University

VISUALISATION OF FLOW PATTERN AND MEASUREMENT OF LIQUID DISTRIBUTION IN A RANDOM PACKED COLUMN USING ELECTRICAL RESISTANCE TOMOGRAPHY (ERT)

By

NAZAR AODA

Bachelor of Chemical Engineering

University of Technology, Baghdad, Iraq, 1991

A Thesis

Presented to Ryerson University in Partial Fulfillment of the Requirements for the Degree of Master of Applied Science in the Program of Chemical Engineering

Toronto, Ontario, Canada, 2010

Author’s Declaration

I hereby declare that I am the sole author of thesis. I authorize Ryerson University to lend this thesis to other institute or individuals for the purpose of scholarly research.

Nazar Aoda

I further authorize Ryerson University to reproduce this thesis by photocopying or by other means, in total or in part, at the request of other institutions or individuals for the purpose of scholarly.

Nazar Aoda

ABSTRACT

VISUALISATION OF FLOW PATTERN AND MEASUREMENT OF LIQUID DISTRIBUTION IN A RANDOM PACKED COLUMN USING ELECTRICAL RESISTANCE TOMOGRAPHY (ERT)

Nazar Aoda

MASc, Chemical Engineering, Ryerson University, Toronto, 2010

The aim of this research is to use Electrical Resistance Tomography technique (ERT) to measure factors that affect local mass transfer at various axial locations in a random packed column with diameter 0.3m and bed height 150cm filled with 2 cm plastic spheres. These factors are: liquid maldistribution, velocity profiles, and flow pattern. The system was designed to run in a trickling down-flow mode and a full liquid up-flow mode. Experiments were performed at flow rates of 3, 6, and 9 gpm (or 0.27 x 10^{-2}, 0.54 x 10^{-2} and 0.8 x 10^{-2} m^3/m^2 s) and under normal operating conditions of 25C^o and atmospheric pressure.

The liquid maldistribution factors were measured via ERT technique and the conventional liquid collection method. Both measurements were conducted at various fluid flow rates at different bed heights. The results of ERT were in very good agreement with the conventional method. The standard deviation values were 17% and 21% at flow rates 3 and 6 gpm respectively.

The numerical values of velocity for full liquid up flow at 3 gpm were 0.83cm/s, 1.2cm/s and 1.11 cm/s for different heights of 30, 60 and 90 cm respectively and the numerical values of velocity for trickle down flow at 3 gpm were 16.5 cm/s, 22.5 cm/s and 24 cm/ for different heights of 30, 60 and 90 cm respectively.

The values of the liquid maldistribution factor for flow rate 3 gpm were 0.43(30cm), 0.33(60cm) and 0.30 (90cm) and for flow rate 6 gpm were 0.33(30cm), 0.27(60cm) and 0.22 (90cm). By comparison with findings of many studies conducted on liquid distribution in packed bed column, a good agreement was observed on the relation of Mf and flow rates and bed heights.

Acknowledgment

I would like to express my deepest gratefulness to Dr. Huu Doan and Dr. Jiangning Wu for their continuous support, encouragements and guidance throughout this endeavor. Their exceptional supervision not only ensured the successful fulfillment of this study but also brought great improvement of my comprehension skills, which I will enjoy forever.

Many thanks go to all of my friends, and colleagues for their helpful advices and wonderful ideas. Special thanks go to Mr. Ali Hemmati, Mr. Danny Boothe and Mr. Tondar Tajrobehkar for their support during the experimental set-up and timely assistance.

Finally, I am grateful to my wife, whose encouragement and support have become my motivation to do and finish this work.

Nazar Aoda

Table of Contents

List of Figures

List of Tables

CHAPTER 1

1. INTRODUCTION

Packed columns are widely used in separation processes such as distillation, absorption and liquid-liquid extraction due to their low pressure drop, high capacities and efficiencies. In the last thirty years, tray columns have been replaced with packed columns. This choice has resulted in a successful development of efficient packings that provide a high absorption capacity per unit volume of packing (Aroonwilas and Tontiwachwuthikul, 1998; Aboudheir et al., 2003).

A typical packed column comprises of a vertical cylindrical container loaded with packing material. In general, the two fluids move counter currently through the column. Liquid enters the top of column and flows downward while contacting with the upward flowing vapor phase. Packing type can be divided into two categories: random and structured. The packing material is designed to increase the interfacial area for mass transfer between the fluids. Every packing should possess a number of important characteristics, such as, a large wetted surface area per unit volume of packed space which allows a large interfacial area for mass transfer, a large void volume for low pressure drop and good wetting characteristics, which give good mass transfer.

In this research the flow maldistribution was studied by estimating maldistribution factor for different packed bed heights, and different liquid flow rates using electrical resistance tomography (ERT) and conventional liquid collection method.

Liquid maldistribution is an important factor in the design, scale-up and operation of packed bed column (Sun et al., 2000). Among the factors affecting liquid distribution in packed beds one will find the initial liquid distribution (ensured by the use of a proper distributor), the packing and fluids characteristics, the pre-wetting conditions and the flow rates. Those factors have been widely studied and reported in literature (Atta et al., 2007; Marcandelli et al., 2000). Many of these studies however, dealt mostly with small sized columns and were performed using liquid

collectors. These techniques are intrusive and can perturb the local flow texture (in this method three packed bed height were employed, the height of the bed was reduced by removing some packings from the top of the bed) as well as the liquid collectors can only give access to the macroscopic flow rate distribution at the exit of the column. As the flow distribution inside the column is not necessarily reflected by the exit distribution, the use of a liquid collector could lead to improper conclusions (Babu et al., 2007). That is the reason why tomographic techniques are preferable, which are non intrusive and suited to obtain a large number of local measurements. In the present study, the information obtained with a liquid collector is compared with that obtained using electrical resistance tomography.

CHAPTER 2

2. LITERATURE REVIEW

2.1 Introduction

Packed columns are popular in the chemical industry due to their low pressure drop, high capacities and efficiencies. They have been widely used in industrial separation processes, such as distillation, absorption and extraction.

Achieving an even flow distribution in a large packed bed is critical to their performance. Flow maldistribution leads to an unwanted residence time in the packed bed, the adverse effect of liquid maldistribution (non-uniform liquid distribution) has long been recognized and several experimental and theoretical studies have been carried out on the subject. One of the sources of liquid maldistribution is the high liquid wall flow. The formation of liquid wall flow is mainly due to the higher void fraction in the wall region. The orientation of packing near the column wall is also important for the determination of wall flow (Sie and Calis, 1996).

The separation efficiency of a packed column is normally expressed by the height equivalent to theoretical plate (HETP) (Treybal, 1987). It is therefore of great interest to the industrial designer to be able to predict the HETP accurately. However, HETP values available in the literature are widely scattered. For 25 mm metal Pall ring packing, a 2-3 fold variation in the HETP has been reported from different researchers (Bolles and Fair, 1982; Hoek et al., 1986; Kister, 1992). The main reason for the large variations in HETP is generally believed to be the non-uniformity of liquid distribution in packed columns. As reported by Nutter et al. (1992), 50~ 75% decrease in packing performance can be caused by a poor liquid distribution. The non-uniform liquid distribution is usually referred to as liquid maldistribution. Ideally, both the liquid and vapor phases should be uniformly distribution in the packing for the maximum efficiency (Kouri and Sohlo, 1987, 1996; Stichlmair and Stemmer, 1987; Olujic and de Graauw, 1989). This chapter presents a survey of the previous studies on the liquid distribution, flow pattern and their effect on the mass transfer efficiency, as well as process tomography technique.

2.2 Liquid Flow Patterns in Random Packed Columns

In a packed bed, various flow regimes are distinguished, depending on gas and liquid flow rates, fluid properties and packing characteristics. According to Charpentier (1976), the four main flow regimes observed are trickle flow, pulsing flow, mist flow and bubble flow. The flow regime boundaries with respect to gas and liquid flow rates are schematically shown in Figure 2-1, each flow regime corresponds to a specific gas-liquid interaction thus having a great influence on parameters as liquid hold-up, pressure drop, and mass and heat transfer rates.

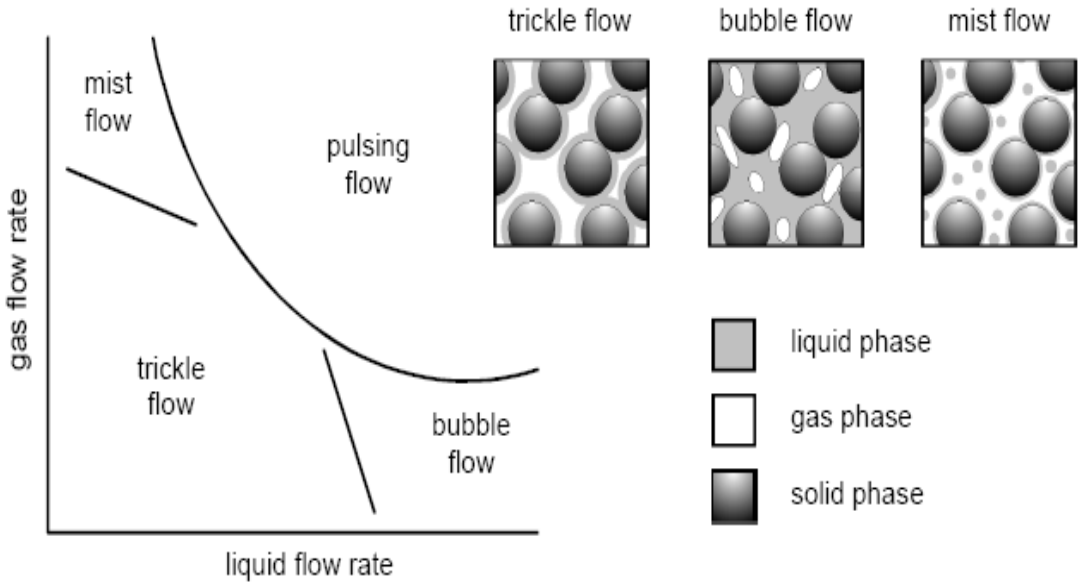

Figure 2-1: Schematic illustration of the location of the trickle, mist, bubble and pulsing flow regimes with respect to gas and liquid flow rates (Charpentier, 1976).

2.2.1 Trickle Liquid Flow

The trickle flow regime prevails at relatively low gas and liquid flow rates. The liquid flows as a laminar film and/or in rivulets over the packing particles, while the gas passes through the remaining void space. At high gas and low liquid flow rates, transition to mist flow occurs. The liquid mainly travels down the column as droplets entrained by the continuous gas phase. In the trickle flow regime, the liquid is present as films, rivulets, pendular structures and liquid pockets (Ravindra et. al., 1997), the latter two being highly stagnant in nature as shown in Figure 2-2.

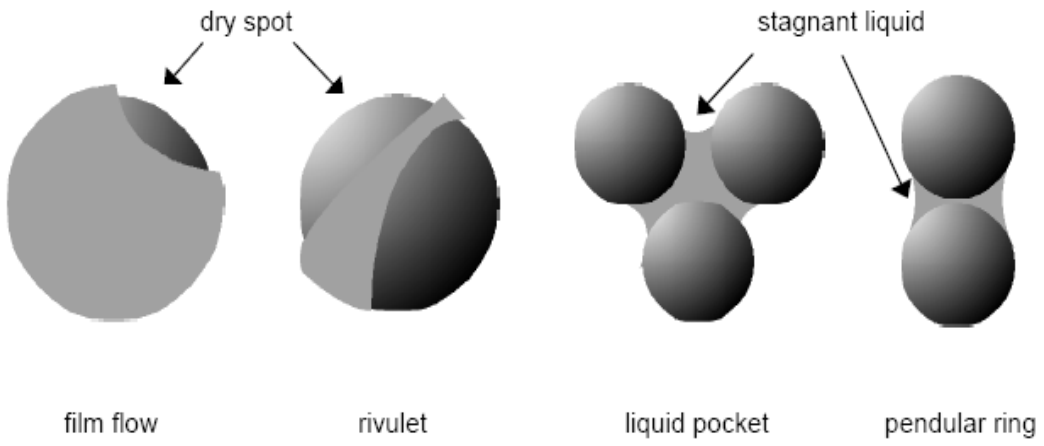

Figure 2-2: Schematic illustration of the several liquid flow textures encountered during trickle flow operation (Ravindra et. al., 1997).

2.2.2 Pulsing Liquid Flow

The flow regime termed pulsing flow prevails at higher gas and liquid flow rates compared to trickle flow. This flow regime is characterized by the passage of liquid rich bubbly waves called pulses, followed by relative quiet periods resembling trickle flow. The pulses are characterized by high particle-liquid mass transfer rates (Rao and Drinkenburg, 1985). Since the gas is dispersed as bubbles inside the pulses, high gas-liquid interfacial areas and gas-liquid mass transfer rates arise (Fukushima and Kusaka, 1977). Inside the pulses, wetting is complete and hence already developed hot spots are periodically flushed with liquid.

2.2.3 Bubble Liquid Flow

The bubble flow regime appears at high liquid flow rates and low gas flow rates, and is opposite in composition to mist flow. The liquid is the continuous phase and the gas moves in the form of dispersed bubbles (Charpentier, 1976).

2.3 Liquid Distribution through a Random Packed Column

A number of forms of non-ideal flow are present in continuous flow systems such as distillation columns, solvent extraction columns and heat exchangers. In general, deviations from ideal flow can be classified in two types. In one type the elements of the flow travel through the apparatus at different velocities, causing channeling and dead zones. In doing so, the flow must remain at least partially segregated with little or no cross mixing within the apparatus. The other deviation (non-segregated flow or axial dispersion) refers to the extent of the local mixing in the direction of flow (Burdett et al., 1981).

Channeling is a simple segregated flow and is developed when the elements of the flow take independent paths through the apparatus as depicted in Figure 2-3(a). In the case that the channels are infinitely thin, channeling approaches laminar flow. Another form of channel flow,

show in figure 2-3(b), is backflow (Mak et al., 1991). Unlike channeling, in backflow some of the channels combine both forward and backward flow resulting in higher fluid velocities than the net average velocity.

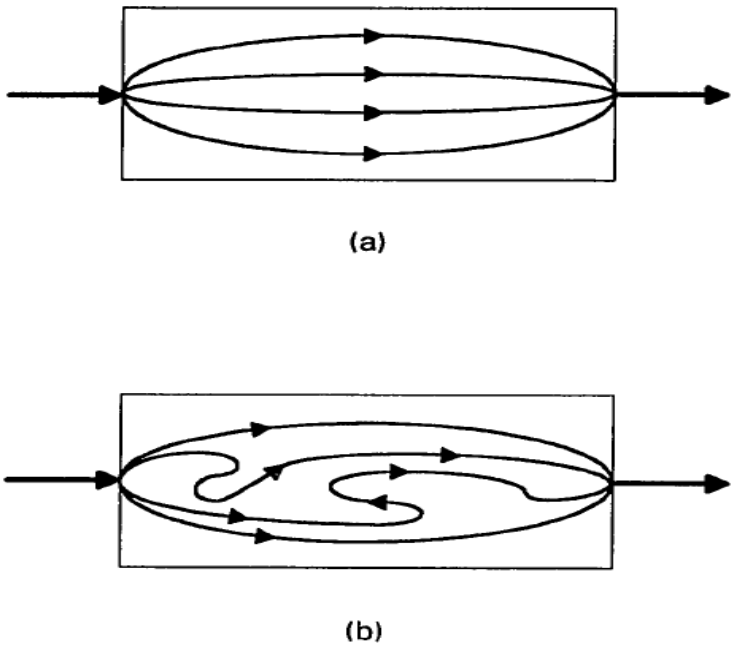

Figure 2-3: Segregated flow (a) channeling, (b) backflow

2.3.1 Liquid Maldistribution in Random Packed Columns

Baker et al. (1935) were the first to undertake a comprehensive experimental study on the liquid flow distribution in random packed columns. They measured the liquid distribution by collecting the liquid at the bottom of the column using a specially designed support plate which divided the column cross section into four equal cross-sectional area concentric rings, with each collecting section amounting to 25% of the column cross sectional area. The authors examined the liquid distribution in packed columns of different diameters using broken stones, spheres, saddles, etc. as packings. The ratio of column diameter to the packing diameter (D_c/d_p) was found to have a significant effect on the liquid distribution in packed columns. The general trend was that the proportion of liquid accumulated on the column wall increased with the decrease of Dc/dp ratio.

Scott (1935) studied the liquid distribution in a column filled with 12.7 mm Lessing rings, 6.35mm and 12.7 mm graded cokes, respectively. All experiments were carried out with water introduced at the top of the column as a point source, and there was no gas or air stream passing up the column. By measuring the liquid flow rates at different locations over a horizontal plane at the bottom of the column, the author demonstrated that the liquid showed a tendency to spread towards the column wall. It was also found that the liquid wall flow increased with the increase of the packed bed height. It was reported that the reason for the liquid to accumulate at the column wall was due to the orientations of the packings in the near wall region.

Porter and Templeman (1968) investigated the liquid spreading as it trickled down a random packed column. A Plexiglas ™ square box containing the random packing was used in the experiments. Water was introduced into the column from the top and there was gas stream circulating through the column. Most of the experiments were carried out with 12.7 mm ceramic Raschig rings but some measurements were also made with 12.7 mm Intalox saddles, 15.9 mm metal pall rings, and 25.4 mm Raschig rings. The liquid distribution in the packing was obtained by measuring the rate of liquid flow from small sampling areas at the bottom of the column. The authors found that the liquid distribution in the packing was far from uniform.

It was observed that the liquid rivulets were formed as the liquid flowed down the column. These rivulets sometimes could run into one another and coalesce to form larger rivulets, and sometimes could break up into smaller rivulets.

Bemer and Zuiderweg (1978) measured the liquid spreading and flow patterns in a 0.2 m column as a function of the wet ability of the packing, packing size, bed height, flow rate and liquid surface tension. Water or water –butanol mixtures were fed into the packed column as a point source in the absence of a gas stream. The support plate was divided into 177 sampling section to measure the liquid flow distribution at the bottom of the column. The radial spreading was found to be dependent only on the packing size. Little or no effect could be found of liquid surface tension on the spreading. However, this finding is contrary to the conclusions of Onda et al. (1973) who found that liquid spreading increased with the increase of liquid surface tension.

A more detailed study on the liquid distribution in the random packing was published by Hoek et al. (1986). A Plexiglas ^{TM} column of 0.5 m diameter with various bed heights up to 2m was employed in their experiments. The random packings used were glass Raschig, stainless steel Pall rings, as well as ceramic and polypropylene Intalox saddles. The superficial liquid velocities used were 5, 10 and 15 mm/s. There was no gas stream used. To study the flow distribution on the scale of packing elements, they divided the bottom support plate into 657 square (16x16mm) liquid catching cells and 24 cells touching the column wall. The liquid flow rate from each cell was measured separately and thus the flow distributions across the column cross section could be obtained. They showed that small scale maldistribution was not influenced by the packed bed height and the initial liquid distribution and thus could be regarded as the inherent property of the packing (Hoek et al., 1986). This aspect of the flow distribution has also been found by Albright (1984) in his simulation of liquid flow in a packed column. He concluded that every packing has a natural liquid flow distribution. An initial distribution that is better than the natural one will degrade to it quickly. Conversely, a poor initial liquid distribution, caused by the ill-design and / or mal-performance of the liquid distributor, will ultimately improve to the natural flow pattern after a certain packed bed height, though sometimes at a very slow rate.

The height required to attain the natural flow pattern depends on the type and size of packings, the random structure of a packed bed, the design of the liquid distributor, and the flow rates of process fluids.

Kouri and Sohlo (1987, 1996) studied the liquid and gas flow distribution as a function of packed bed heights, liquid and gas flow rates, and the initial inlet profiles of the liquid and gas in a 0.5 m diameter column. The random packings examined were ceramic Intalox saddles and plastic Pall rings. The main emphasis of their work was on the interaction between the countercurrent gas and liquid phases. They observed that the liquid distribution over the bulk region of the packed bed became more uniform as the gas flow rate was increased provided that the initial gas distribution was uniform.

They also found that the developing length for the liquid to reach the fully developed flow pattern depended on the gas flow rate. When there was no gas circulating through the packed column, the packed length of 2.0 m was required for the liquid to approach the fully developed state for 25mm Pall rings at the liquid flow rate of 2.5 kg/m^2s,but this length was reduced to about 1.0~1.5m as the gas flow rate increased to 2.7 kg/m^2s.

The effect of gas flow on the liquid distribution in packed columns was also observed by Dutkai and Ruckenstein (1970). In a study of liquid spreading in a packed column of 0.15 m diameter, they demonstrated that the liquid spreading coefficient increased with the gas loading up to 70% of flooding.

Kouri and Sohlo (1996) introduced the gas only in the central part of the column with diameter 0.5m, which occupied about 64% of the column cross sectional area, they found that a bed height less than 0.5 m was sufficient to smooth out the non-uniform initial distribution of gas, and concluded that the uniform gas distribution may be assumed throughout the column.

As can be seen, the problems of liquid maldistribution in packed column have long been recognized and have been a subject of extensive studies.

2.3.2 Effect of Liquid Mal-distribution on Mass Transfer

Mass transfer in packed columns has been studied extensively due to its importance in many industrial processes such as absorption and stripping. The mass transfer coefficients have been correlated in terms of the gas and liquid loadings, and physical properties of the system. The effect of the packing itself on the mass transfer has been included in terms of its specific surface area and nominal diameter.

Liquid mal-distribution in a packed column tends to reduce the mass transfer efficiency. Manning and Cannon (1957) examined the effect of liquid maldistribution on the packing separation efficiency. They demonstrated that as little as 1% of liquid channeling may cause 44% efficiency loss. They also pointed out that liquid maldistribution effect on separation efficiency depended on the number of theoretical plates and the relative volatility of the system being separated.

Mullin (1957) also found that the liquid maldistribution has a detrimental effect on the packed column separation efficiency. To investigate this, the author modeled the packed column as two parallel columns and set different liquid flow rates in each of the columns but keeping the gas flow rate the same. These two columns were conceptually divided by an impermeable membrane, so no exchange of mass occurred between the two columns. Through a McCabe – Thiele plot, the author demonstrated that the slope of the operating line decreased due to the liquid maldistribution and therefore the operating line moved towards the equilibrium line. More stages were thus required for a given separation when compared to the uniform flow distribution case.

Huber and Hiltbrunner (1966) further developed the concepts of Manning and Cannon (1957) and Mullin (1957) by allowing cross mixing of liquid and vapor. The radial cross mixing is the result of the side-movement of liquid and vapor due to the deflection of packing elements. Liquid maldistribution in the packing causes concentration gradients along the column cross section. On the other hand the cross mixing cancels out the difference in concentrations.

Based on their studies, they concluded that in columns with a ratio of D_c /d_p less than 10, the cross mixing is large enough to compensate for the maldistribution effect and only very serious liquid flow maldistribution would cause a significant separation efficiency loss. On the other hand, when this ratio is greater than 30, the lateral mixing may not be effective enough to offset the influence of liquid maldistribution. Therefore, in a large diameter packed column, the liquid maldistribution problem is more serious than that in a small diameter column.

More recently, Zuiderweg et al. (1993) proposed a zone/stage model to calculate the effect of the maldistribution on the efficiency of a packed column. In this model, the packed column is divided radially into a number of concentric zones, with each zone being of the same width and height. The height of a zone is chosen to be equal to the HETP, which is a function of the system properties and the packing and can be determined in a laboratory scale column. The width of each zone is arbitrarily set to be 2-3 times the packing diameter.

The calculation is divided into two steps. The first step is to calculate the liquid flow distributions based on the diffusion model and a uniform flow pattern is assumed for the vapor phase. The second step is the mass transfer calculation based on the equilibrium stage concept. The mass transfer calculation is iterative with end conditions based on the overall material balance being satisfied. With this model, they studied the effect of different kinds of initial liquid distributions on the separation efficiency. The general conclusion derived from their work is that the overall efficiency is very sensitive to the initial liquid distribution, especially in large diameter packed columns.

Stichlmair and Stemmer (1987) took a different approach to model the mass transfer process in a packed column in the presence of liquid maldistribution. In their experiments, they used hot water and air as the working system. The temperature profiles of the water at different packed bed height were measured. The behavior of temperature profiles should be similar to that of the concentration profiles in a real mass transfer system based on the analogy between heat and mass transfer.

The shape of the temperature profile indicates the degree of liquid maldistribution. For example, if the temperature profiles are horizontal lines, this implies that there is no maldistribution present in the liquid and gas phases. Based on the temperature profiles, they calculated the number of transfer units by considering the packed column as a large number of hypothetic parallel channels with different gas and liquid loads. In each channel, the plug flow patterns were assumed in both the liquid and gas phases. They concluded that liquid maldistribution has a severe effect on separation efficiency. Up to 50% of the mass transfer efficiency may be lost due to liquid maldistribution even with good initial liquid distribution.

2.4 Tomography Technique History and Applications

The concept of Tomography was first published as early as 1826, by Abel, a Norwegian physicist, for an object with axi-symmetrical geometry. In 1917, Radon discovered a way to mathematically reconstruct any function from its projections, and in 1972 Hounsfield invented the first x-ray computed tomographic scanner, which used the Radon transform to reconstruct an object from its X-ray projections (Kak and Slaney, 1991).

Godfrey Hounsfield and Allen Cormack were jointly awarded the Nobel Prize in 1979 for their pioneering work on X-ray Tomography. A number of applications of tomographic imaging of process equipment were described in the 1970's, but generally these involved using ionizing radiation from X-ray or isotope sources, and were not satisfactory for the majority of process applications on a routine basis because of the high cost involved and safety constraints. Most of the radiation-based methods used long exposure times which meant that dynamic measurements of the real time behavior of process systems were not feasible.

In the mid-1980s work started that led to the present generation of process tomography systems. At Manchester University there began a project on Electrical Capacitance Tomography for imaging multi-component flows from oil wells. About the same time a group at the Morgantown Energy Technology Center in the USA was designing a Capacitance Tomography system for measuring the void distribution in gas fluidized beds. The capacitance transducers used for both

these systems were only suitable for use in an electrically non-conducting situation. There was rapid progress in several centers with Sheffield University and Royal Hallamshire Hospital, Sheffield, in the UK as well as Wisconsin University and Rensselaer Polytechnic Institute in the USA taking major roles. The success of this early work encouraged the setting up in (1988) of a European Concerted Action on Electrical Impedance Tomography for Medical applications (CAIT) (Williams and Beck, 1995).

2.4.1 Electrical Resistance Tomography Application

Electrical Resistance Tomography (ERT) is one of the most common techniques in the process tomography. The word 'tomography' is a well-defined term, which means a cross-sectional image of a particular area, while, process tomography means a cross-sectional image of a process (Dickin and Wang, 1996).

Electrical Resistance Tomography (ERT) is a measurement technique for obtaining information about the contents of process column, vessels and pipelines. Multiple electrodes are arranged around the boundary of the vessel at fixed locations in such a way that they make electrical contact with the fluid inside the vessel but do not affect the flow or movement of materials (Mann et al., 1997).

ERT is a simple and robust measurement technique with a wide range of research and development applications demonstrated, including measurement and control of bubble columns, investigation of mixing processes, study of a solid-liquid filtration process and monitoring the performance of a hydro-cyclone.

Grieve et al., (1999) reported a feasibility study on applying ERT to a commercial 1.5 m^3 pressure vessel. A temporary 16-electrode ring ERT sensor was fitted to the filter, and brine slurry was filtered under a pressure of 1 bar (g) nitrogen for approximately 2 hours. After drying, the cake was rewetted with brine via a single entry point, and filtration was repeated several

times. The images clearly showed a feature corresponding to the position of a crater caused by the brine feed point, which could be viewed through the sight glass in the top of the vessel.

Vlaev et al., (2000) described solid-liquid filtration monitoring by means of a 16-electrode ring ERT sensor on a 1m diameter filter. ERT was able to measure the conductivity changes accompanying the rise and fall of liquor level above the filter cake. The image showed a loss of symmetry if the ERT sensor is displaced from the horizontal. The ERT sensor can, thus, provide potential information on correct assembly and ongoing mechanical integrity of the filtration system. ERT was also demonstrated to detect malformation and unevenness in a forming filter cake.

Grieve et al., (2001) conducted a scale-up of this application to a 36-m^3 production pressure filtration vessel at the agrochemicals manufacturing site of Syngenta Ltd (Huddersfield, United Kingdom). The stated purpose of the work is to provide real-time information on end point of filtration and drying, imperfection in the filter cake, and solvent displacement of the mother liquor. This study demonstrated that an ERT sensor could be retrofitted to a large pressure filter without the need to modify the internal structure of the unit. It also demonstrated that ERT could be certified to comply with intrinsic safety regulations rendering the technology suitable for the most hazardous and flammable atmosphere. The design of the electrodes suffered from a number of weaknesses, which were resolved through a number of design iterations.

Williams et al., (1998) demonstrate the measurement of gas and solids distribution in a 30-L laboratory stirred vessel equipped with 4 planes of ERT sensors (each consisting of 16 stainless steel electrodes on the circumference of the vessel and other additional electrodes mounted on the impeller shaft). The result from the gas dispersion measurements of the four cross-sectional conductivity maps were stacked together and linearly interpolated between adjacent maps. A color scale was used to distinguish the conductivity, and, hence, gas hold-up variations within the volume. Red, yellow/green, and blue correspond with high, medium, and low gas hold-up.

Ricard et al., (2005) designed and built a laboratory-scale apparatus to evaluate the suitability of ERT for modeling and analysis of pharmaceutical mixing processes. A 3.5 L vessel was

constructed from glass with geometry designed to mimic pilot plant vessels and operating conditions. The jacketed vessel was fitted with 65 platinum electrodes (4 rings of 16 electrodes and an earth electrode) and provided operation over a wide range of temperatures, good optical access, good chemical compatibility, and minimal electrode protrusion. This work focused on mixing and progress of a chemical reaction.

The image reconstruction algorithm produces the electrical conductivity distribution on a 316-pixel circular grid. The pixel data were used to determine t_{99}, which is the time to reach 99% homogeneity. In general the mixing-time measurements showed good reproducibility and followed the expected trend. The data obtained were compared with correlations from literature, and good agreement was found.

In addition to mixing times, Ricard et al., (2005) used ERT to monitor the hydrolysis of ethyl acetate to assess the suitability of the technology to monitor chemical reactions. The change in electrical conductivity over time is proportional to conversion because of the consumption of sodium hydroxide and the large difference in mobility of OH^- and $CH_3CH_2^-$ ions. To compare the ERT data with that from another on-line measurement technique, a Raman probe was used to follow the reaction. The Raman spectra were analyzed by Iterative Target Transform Factor Analysis. They found good agreement between the average bulk conductivity measured by the ERT system and the data obtained from the on-line spectroscopic measurements. This demonstrates the applicability of ERT to monitor the conversion of a dynamic chemical process.

Stanley et al., (2005) demonstrated the application of ERT to a precipitation reaction in a pilot-scale vessel (2.3 m^3). The vessel was equipped with 8 planes of ERT sensors (each consisting of 16 stainless steel electrodes), which gives 8 × 316, or 2,528 pixels. The reaction under investigation was the semi-batch precipitation of barium sulfate from barium chloride and sodium sulfate. The measurements were presented as time-wise conductivity profiles showing the mean, 5th and 95th percentile pixel conductivities and 3-dimensional conductivity images. Measurements were collected for with and without agitation. There was a marked contrast in the results with and without agitation with the conductivity profiles displaying very different features. The 3-dimensional reconstructed images also displayed different features; in the case of

the agitated system, the feed plume appears as a region of high conductivity, whereas in the case of the un-agitated system, the reverse is observed—the feed plume appears as a region of low conductivity. The authors postulated that the region of high conductivity representing the feed plume in the agitated case was because of the presence of dissociated barium and chloride ions, which were unmixed and, therefore, un-reacted with sodium sulfate. In the un-agitated case, the authors suggest that the lack of agitation causes a high concentration of barium chloride at the feed addition point leading to immediate formation of precipitate with sodium sulfate. This causes an ion deficit around the feed point, giving rise to a low-conductivity plume. Barium chloride added after this will not come into contact with sodium sulfate for some time and relies on convective mixing induced by the feed to transport it to regions where sodium sulfate is present and primary nucleation can occur.

Wang et al., (2001) reported the application of ERT to identify the flow regime and maximum interfacial area in a laboratory-scale bubble column. Features indicative of air concentration and bubble fluctuations were extracted using mean conductivity and derivatives from a sequence of dynamic images. Furthermore, these parameters were used with a close-loop Proportional Integral Derivative (PID) controller to maintain the flow with the maximum interfacial area in the bubble column using the bandwidth of bubble fluctuation.

Bolton et al., (2005) used ERT to qualitatively demonstrate the flow pattern through a radial flow-packed bed reactor to confirm the design intent. A physical model of the proposed new radial flow reactor design was constructed. It had an internal diameter of 914 mm and a cylindrical flow collector of a 1000 mm height was located in the centre of the reactor. The lower 800 mm of the collector was perforated with small diameter circular holes representing 29% of the surface area. The reactor was packed to a height equal to the top of the central collector with a narrow outer annulus of 10 mm diameter spheres and the remainder was packed with 3 mm diameter spheres. A disc was placed on top of the collector to aid flow distribution and a final layer of 10 mm diameter spheres was added above the combination of 3 and 10 mm diameter spheres. A flow distributor was located above the packed bed reactor to provide a uniform flow of water over the cross-sectional area. Verification of CFD results was an integral part of the study. They showed that the overall flow patterns agreed qualitatively well with the CFD results.

2.4.2 Other types of Tomography Techniques Applications

Other types of tomography techniques also possess great potential applications that have been applied include Gamma-ray tomography, X-ray tomography, electrical capacitance tomography (ECT), and nuclear magnetic resonance imaging (MRI) (Williams and Beck, 1995).

The use of Gamma-ray for industrial process measurements dates back to at least 1962,that a gamma scan can be used to diagnose mechanical problems, such as tray damage or process-related problem, such as flooding of column , when a radiation scan was performed to distillation column (Severance, 1981). Gamma-ray Grid Scan Technique was used to provide information about the average density along a packed column (Bowman, 1991, 1993). Gamma-ray GT was also used to determine distribution of fluidized solids in a fluidized catalyst cracking (Azzi et al., 1991).

Smith et al., (1995) studied the hydrodynamic properties of slurry bubble column and three-phase fluidized bed using an X-ray imaging technique. In particular they measured the bubble sizes, velocities, and hold-up within column. The technique was a radiographic, in which X-ray pulses were passed through a reactor, amplified by a cesium-iodide image intensifier, and then captured on a video camera, the video camera was synchronized with the X-ray pulses. The solid phase in the reactor was zirconia of diameter 38 μm. The liquids used were water and water-glycerol mixtures. The fluidizing gas was typically nitrogen, although helium was used for some of the high-pressure experiments.

Electrical capacitance tomography (ECT) was applied to a trickle-bed reactor by Reinecke and Mewes (1996). The imaging system consisted of three planes of electrodes each segmented into 16 electrodes. The set of measurement electrodes of is 30-mm tall. The two sets of guard electrodes are each 100-mm tall. The electrodes can be moved axially to image different planes. The image frequency is 100 Hz, with a total of 104 capacitance measurements required per image. The column used was constructed of acrylic and was 120 mm in diameter. The packed section contained two meters of 10-mm-dimeter ceramic sphere. Air and water flowed co-currently downward through the column at ambient pressure during the studies. The results of

the ECT imaging of a trickle-bed included images representing the flow in the column. Pulse flow was observed at various liquid and gas rates.

Gladden and Alexander, (1996) used nuclear magnetic resonance imaging (MRI) to characterize the pore spaces in a packed bed of particles. A 4.5-cm-inner-diameter glass column containing 6-mm glass spheres and water was imaged. A three-dimensional data set was acquired that was used to identify the pores. From this information, the pore size distribution and the pore volume as a function of pore surface area were calculated.

The work Sederman et al., (1997) incorporated short (4.5 cm) and tall 970 cm) packed beds. Five-millimeter-diameter glass sphere were used in both. They also used nuclear magnetic resonance imaging (MRI) in their study. The columns were filled with de-ionized water, all air bubbles removed, and a seal was formed to prevent air from entering the system during imaging. A constant flow of water passed through the column as the images were obtained. The focus of this study was to obtain velocity images. The flow velocity was then correlated with structure of the bed to visualize the flow around individual glass spheres.

CHAPTER 3

3. ERT TECHNIQUE

3.1 ERT Operating Principle and Structure

The basic principle of ERT is to install a number of sensors around the pipe or vessel to be imaged (Williams and Beck, 1995). This reveals information on the nature and distribution of components within the sensing zone. The sensor output signals depend on the position of the component boundaries within their sensing zones (Huang et al., 1992)

Figure 3-1 illustrates the schematic diagram of a typical ERT system, consisting of three main parts as a sensor system / process column, a data acquisition system (DAS) and a host computer / image reconstruction system.

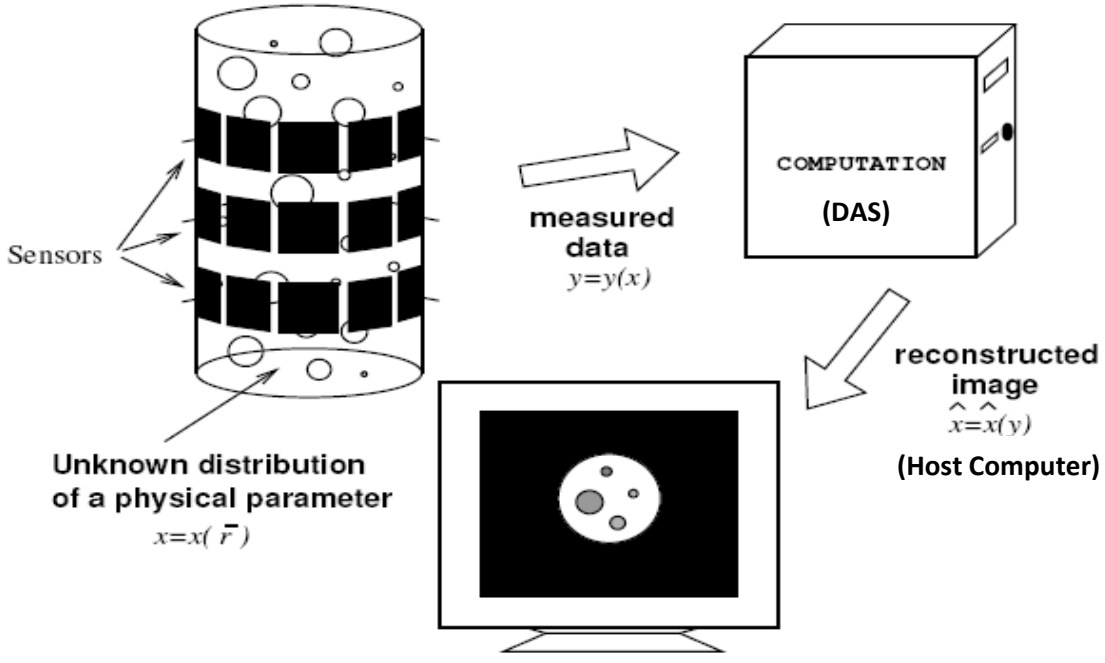

Figure 3-1: The structure of a typical electrical resistance tomography system

Most tomographic techniques are concerned with extracting information to form a cross-sectional image. A computer is used to reconstruct a tomographic image of the cross-section being observed by the sensors. The image data can be analyzed quantitatively for subsequent use to improve process control.

3.2 Sensors geometry and construction

Tomography technology is based on using measurement signals from a sensor surrounding the periphery of an object, such as process vessel or pipeline to provide information on the nature and distribution of the components within the sensing zone.

All tomographic techniques are concerned with extracting the information to form a cross-sectional image, which can then be analyzed to monitor and possibly control the process. There are a number of sensing methods can be employed based on the measurement of transmission, diffraction, or electrical phenomena (Bukhari and Yang, 2004).

The most common electrode geometry, shown in Figure 3-2, electrodes arranged at equal intervals around the boundary of a circular vessel. Alternative arrangements include electrodes arranged around a square cross-section and a vertical series of electrodes. The electrodes are connected to the data acquisition system by a co-axial cable which assists in reducing the effect of extraneous environmental noise and interference. The outer sheath of the co-axial cable is coupled to the feedback path of a voltage buffer to provide further noise immunity and the inner core is capacitively coupled to the input of the voltage buffer.

The material for electrode construction depends largely on the process application. The material should be more conductive than the fluids being imaged to prevent problems due to contact impedance. Typically the electrode material is stainless steel, brass or silver palladium alloy. The dimensions of the electrodes are a function of the vessel diameter, range of conductivity to be measured, velocity of materials and the required imaging speed (ITS, 2006).

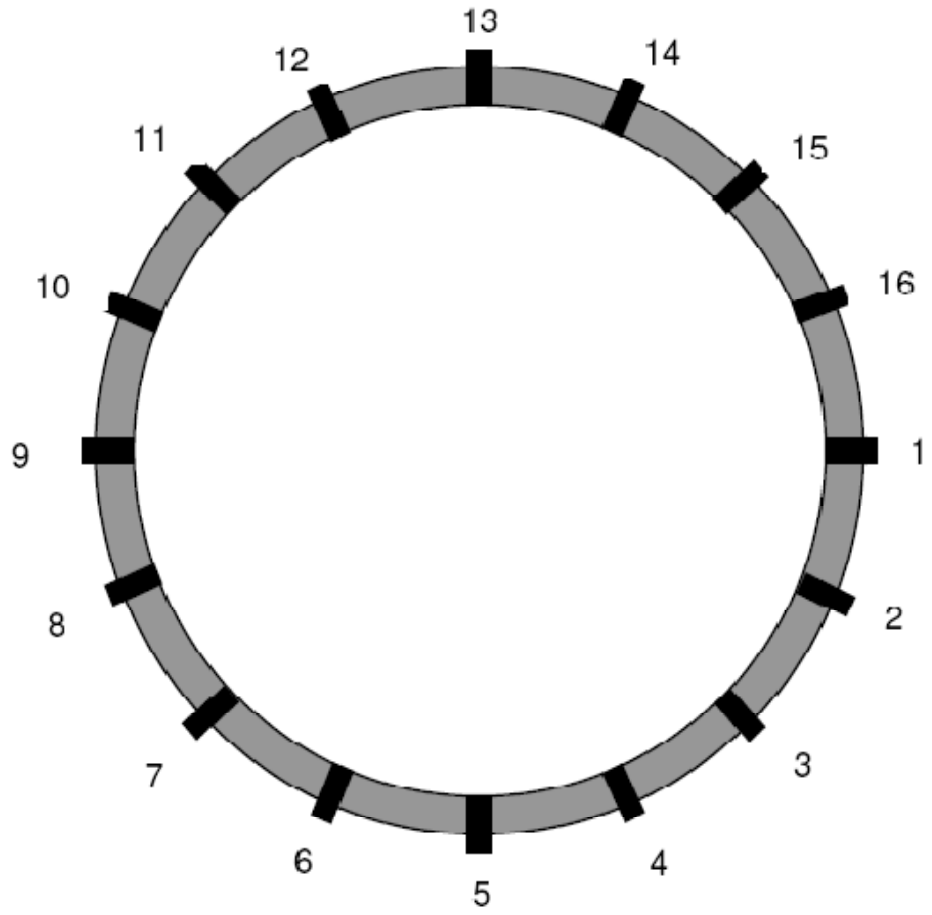

Figure 3-2: Schematic diagram of electrode arrangement and placement

3.3 Data Acquisition System (DAS)

The Data Acquisition System (DAS) is responsible for obtaining the quantitative data describing the state of the conductivity distribution inside the pipeline. The data must be collected quickly and accurately in order to track small changes of conductivity in real-time thus allowing the image reconstruction algorithm to provide an accurate measurement of the true conductivity distribution. Data Acquisition System is shown in a schematic form in Figure 3-3, commencing at the bottom left corner with the voltage generator (1); and then, in a clockwise direction, the electrode current injection unit (2) which drives each electrode on the process vessel, and its control module (3). This is followed by the voltage measurement, demodulation and filtering unit (4) (Holden et al., 1998).

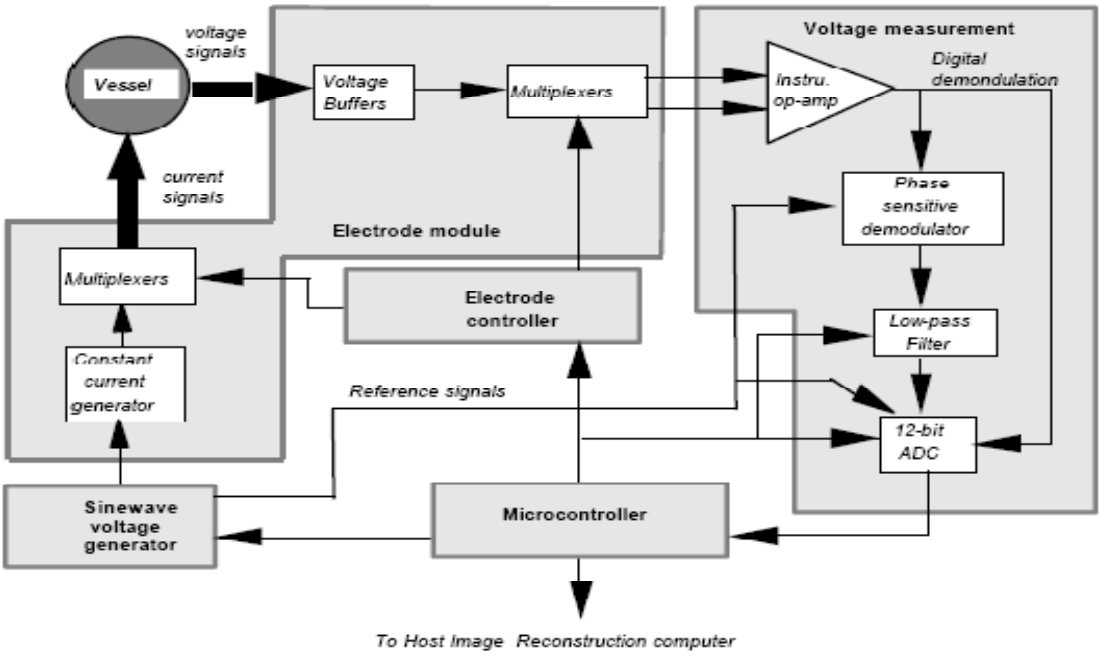

Figure 3-3: Structure of the Data Acquisition System (Holden et al., 1998)

3.4 Host Computer / Image Reconstruction System

The ITS System 2000 software utilizes a Linear Back Projection (LBP) image reconstruction algorithm. This offers fast processing times in comparison to other algorithms.

All tomographic techniques are concerned with extracting the information to form a cross sectional image, which can then be analyzed to monitor and possibly control the process. The output signal from the sensors will be sent to the computer via an interfacing system. The computer will receive the signal from the respective sensors to perform data processing and finally construct a cross-section flow image in the pipe through image reconstruction algorithms. The tomographic imaging of objects provides an opportunity to unravel the complexities of structure without invading the object (Dyakowski, 1996).

The measurement system is driven by a Microsoft Windows interface that can be used for both measurement and data analysis (on and offline). The Windows approach offers the ability to set up multiple experiments and to easily compare current and historical data.

3.5 Data Measurement Strategies

The measurement strategy or sensor configuration for measuring the conductivity distribution within the vessel is of paramount importance. Figure 3-4 illustrates some of the sensor configurations. In all cases, the voltage measurements pass through a multiplexer into a differential input amplifier which amplifies the potential difference between the two input voltage signals. The amplifier has the ability to reject common-mode signals such as electrical noise. The sine-wave output of the differential amplifier is then fed into a programmable gain amplifier (PGA) to accommodate the wide dynamic range of voltage signals obtained from the many pairs of electrodes. A phase-sensitive demodulator (PSD) is employed after the PGA to demodulate the voltage signals prior to low-pass filtering (Dickin and Wang, 1996).

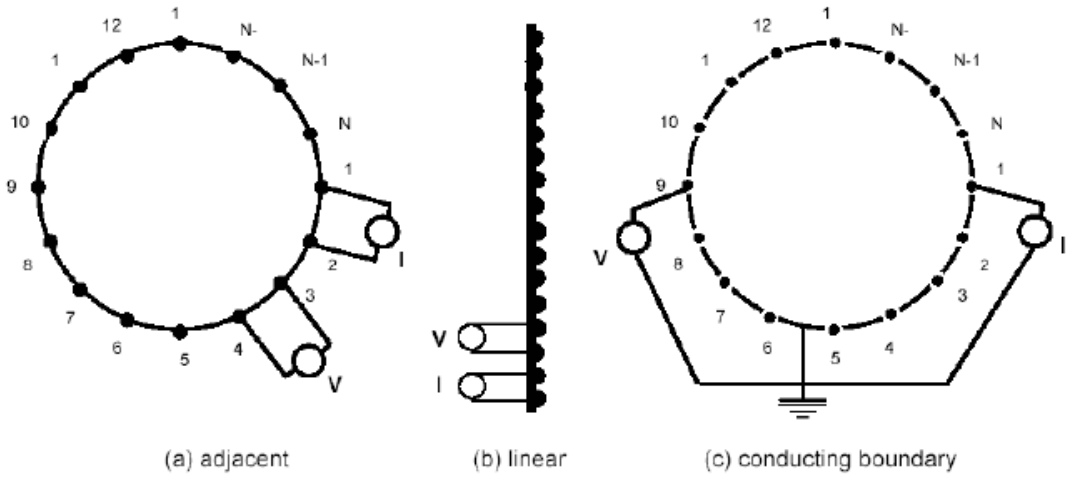

Figure 3-4: Illustrates of the sensor configurations.

1. Normal Adjacent

Normal adjacent configuration is recommended measurement strategy for sensors with insulating boundaries with 16 electrodes arranged at equal intervals around the periphery of the sensor. Current is applied through two neighboring electrodes (e.g. electrodes 1 and 2), The voltages are measured from the remaining pairs of neighboring electrodes (e.g. electrodes 3 and 4), Current is then applied through the next pair of electrodes and the voltage measurements are repeated. The procedure is repeated until all the independent measurements have been made. Yields N2 measurements, where N is the number of electrodes. Of these only N (N-1)/2 are independent. To avoid electrode/electrolyte contact impedance problems, the voltage is not measured at a current injecting electrode and the total number of independent measurements M is reduced to N (N-3)/2. A 16-electrode sensor gives 104 independent measurements.

2. Linear Measurement

Linear measurement is used when a vertical series of electrodes mounted either on a linear rod or fixed along the inside of a vessel.

3. Conducting Boundary

Conductivity boundary arrangement is applied to pipelines and vessels with conducting boundaries, e.g., stainless steel pipes. The relatively large surface area of the conducting boundary is employed as the current sink to reduce the common-mode voltage across the voltage across the measurement electrodes. The earthed conducting boundary also acts as a shield, reducing the effects of electromagnetic interference.

3.6 Image Reconstruction

Following the acquisition of data from the boundary of the object to be imaged it is necessary to process this data using an appropriate image reconstruction algorithm. For an ERT system the reconstructed image will contain information on the cross-sectional distribution of the electrical conductivity of the contents within the measurement plane. A square grid with 20 x 20 = 400 pixels represents the vessel interior cross-section. Some of these pixels will lie outside the vessel circumference as shown in Figure 3-5 and the image is therefore formed from the pixels inside the vessel. The circular image is constructed using 316 pixels from the 400 pixel square grid (ITS, 2006).

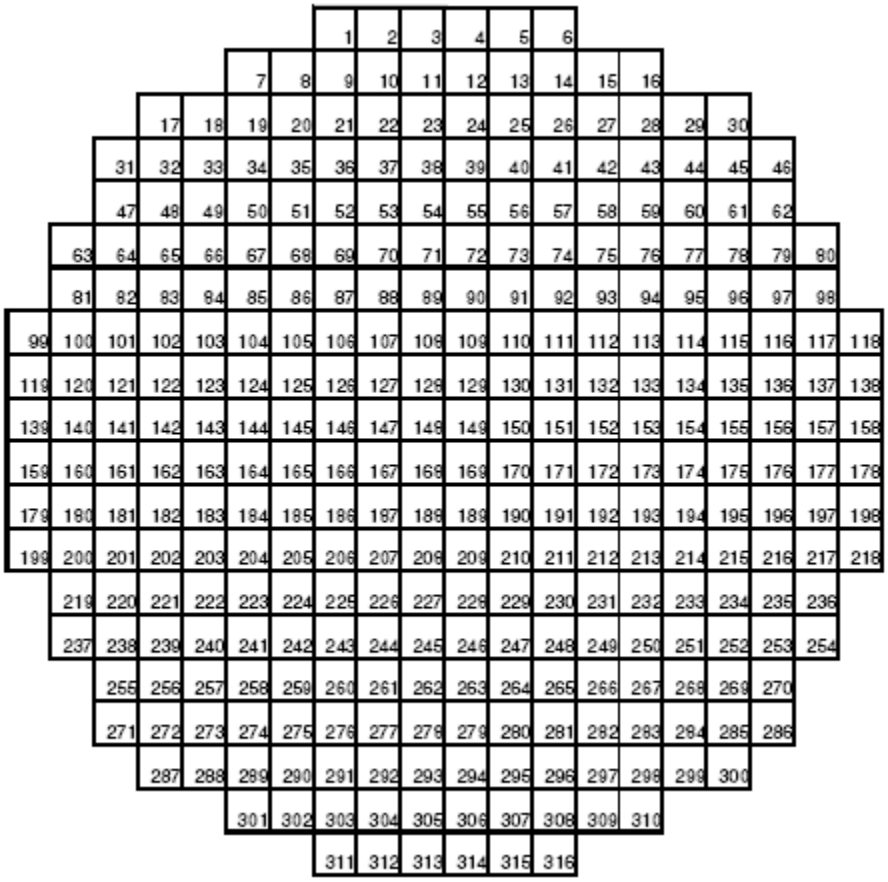

Figure 3-5: Image reconstruction grid (ITS, 2006)

3.6.1 The Forward Problem Image Construction

The forward problem i.e. the changes in electrical measurements which will result when the electrical conductivity of one pixel only in the cross-section is changed by a known amount. This can be done in a number of ways including direct measurement although it is much more commonly performed by computation.

3.6.2. The Inverse Problem Image Construction

The inverse problem is to determine the conductivity distribution σ (x, y) from a finite number of boundary voltage measurements. There are three important reconstruction techniques (Tapp and Williams, 2000): Linear Back Project (LBP), Newton-Raphson Method (MNR), and Parametric Model Technique (PM).

The inverse problem in ERT is non-linear due to the equipotential lines curving in a way which depends on the spatial conductivity distribution. Before the inverse problem can be solved, it is necessary to solve the forward problem - forward because σ (x, y) is known everywhere inside the sensor (i.e. the task is to find the boundary voltage measurements, given the injection current I applied to the electrodes and the conductivity distribution σ (x, y) at all points) - by the calculation of a sensitivity map which describes the behavior of the sensor (Wang, 2002).

3.6.3 Linear Back Projection

The linear back-project is used because it is very simple and computationally fast, due to the fact that the reconstruction process is reduced to matrix-vector multiplication (Barber and Brown, 1984). Figure 3-6 illustrates how the back-project images can be assembled to form an image of the conductivity distribution. In practice back-projection is a weighted back-projection shown in Figure 3-7.

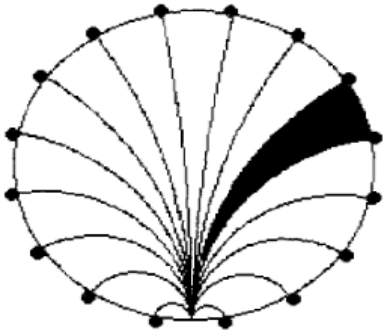

Figure 3-6: The normalized boundary value is back-projected into the region

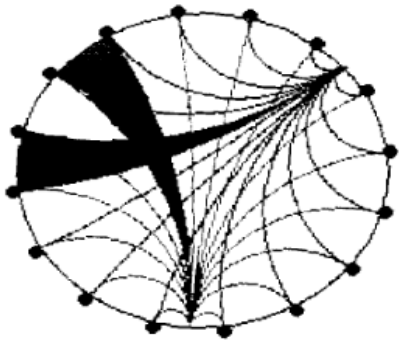

Figure 3-7: Back-projections are added together to produce an estimate of conductivity changes

CHAPTER 4

4. EXPERIMENTAL METHODOLOGY

4.1 Experimental Setup

A flow diagrams of the experimental setup used in this study is illustrated in Figure 4-1 and Figure 4-2 for trickle down flow and full liquid up flow respectively. A picture of the experimental setup is shown in Figure 4-3.

The experimental system consisted of two main sections: (1) the column and its accessories, (2) electrical resistance tomography system.

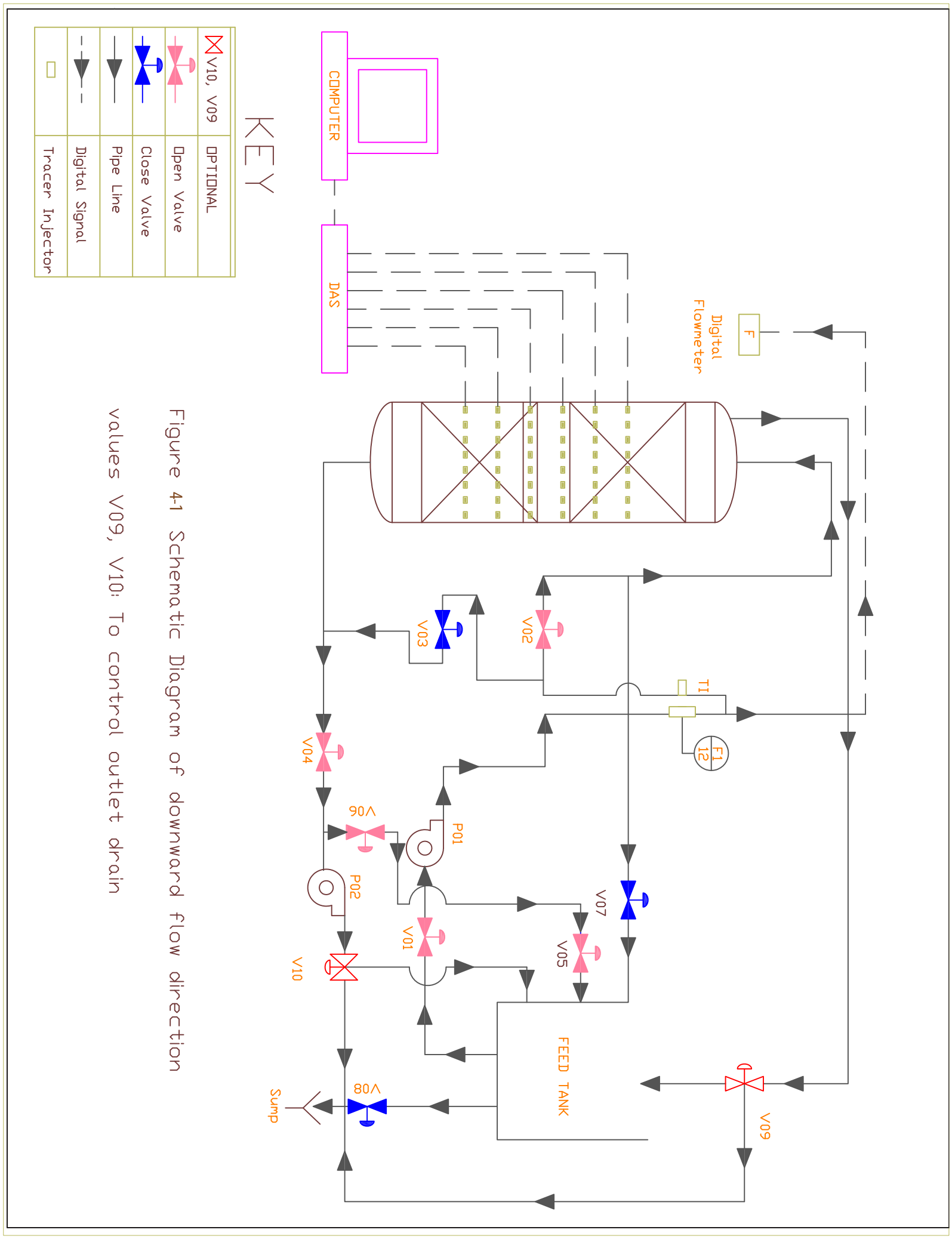

Figure 4-1 Schematic Diagram of downward flow direction values V09, V10: To control outlet drain

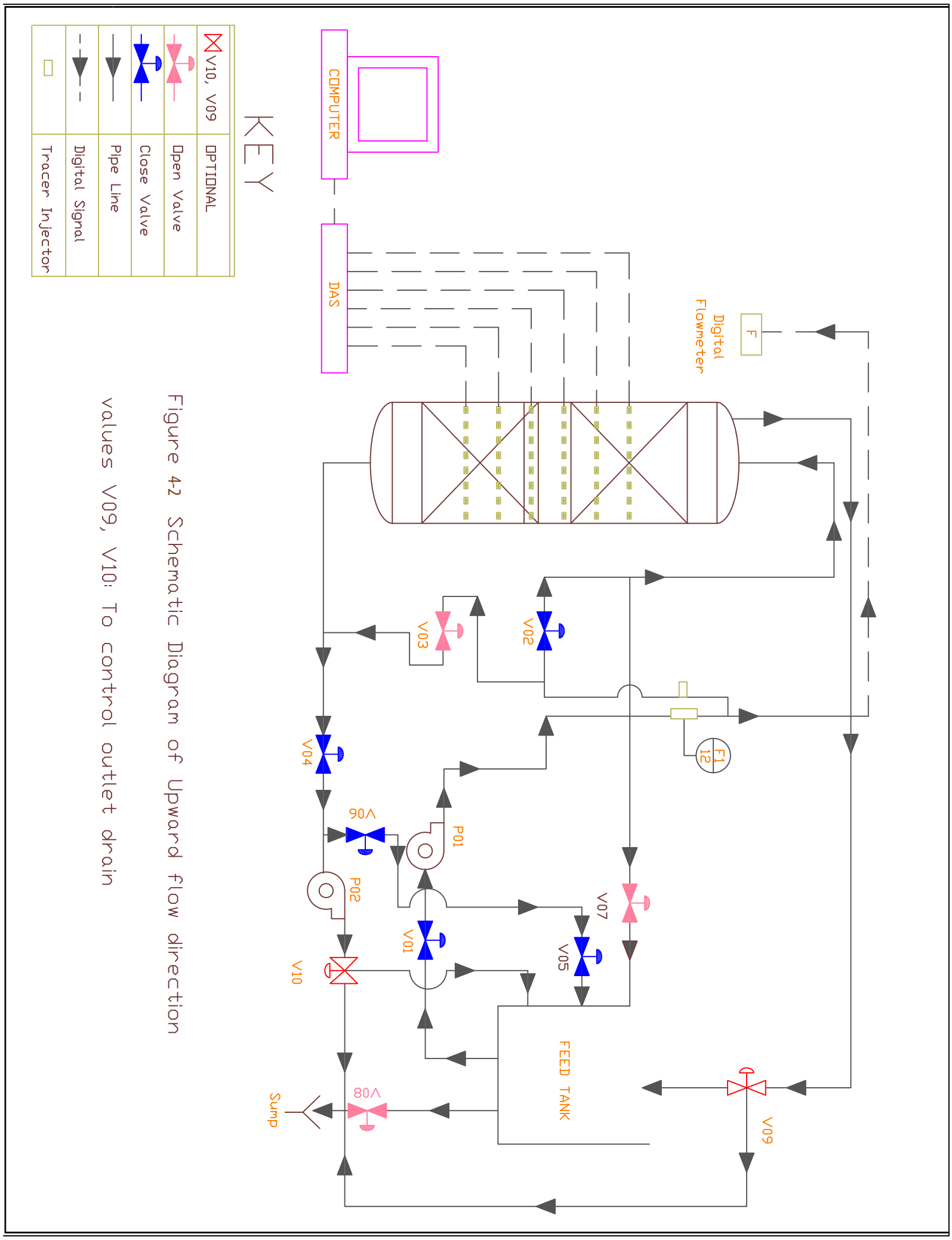

Figure 4-2 Schematic Diagram of Upward flow direction

values V09, V10: To control outlet drain

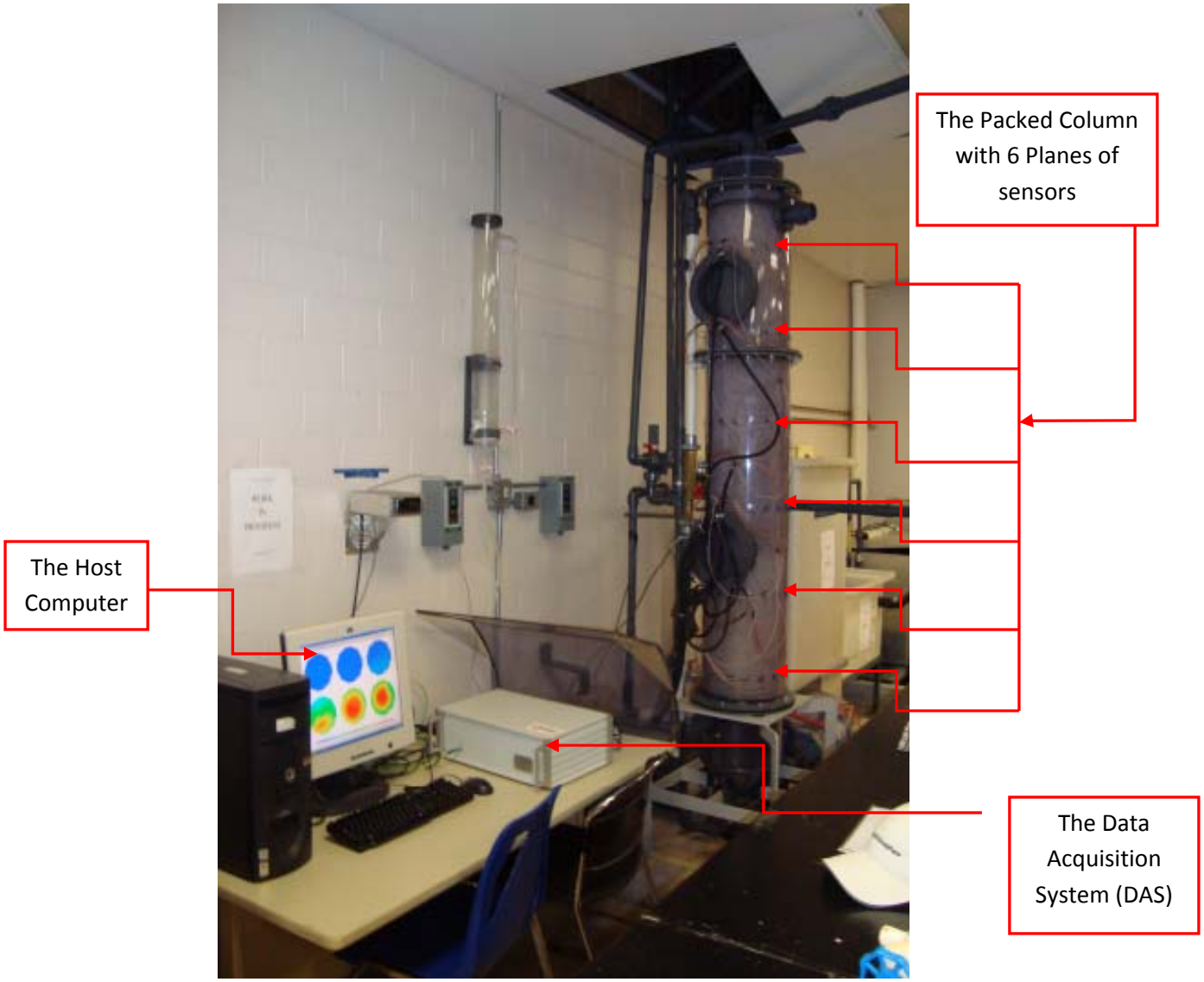

Figure 4-3: The Picture of the Experimental Setup

The packed column used in this study have an inside diameter of 0.3 m and a bed height 1.5 m. The column was constructed of transparent PVC to allow visual observation of the liquid flow inside the column. The column was divided into three sections: (a) a top section used for liquid-distributor connection and liquid-feed; (b) a 1.5 m high packed section and a bottom part for liquid collector and/or liquid feed (c) liquid collector. Figure 4-4 provides a detailed schematic of the column and its relevant dimensions. The column was filled with 2.0 cm plastic spheres.

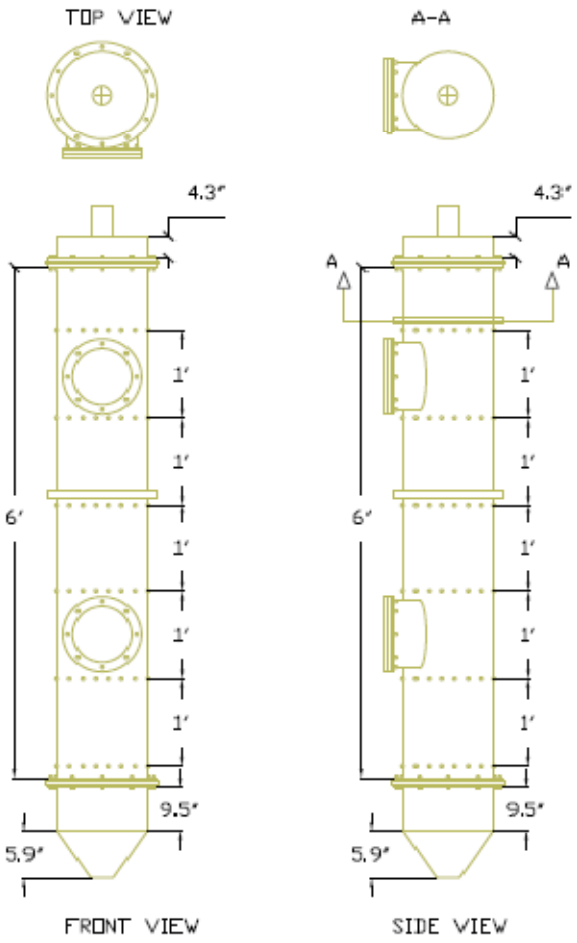

Figure 4-4: Schematic diagram of the experimental column

A 25-delivery-point distributor was employed as liquid distributors. Figure 4-5 below shows the multipoint distributor.

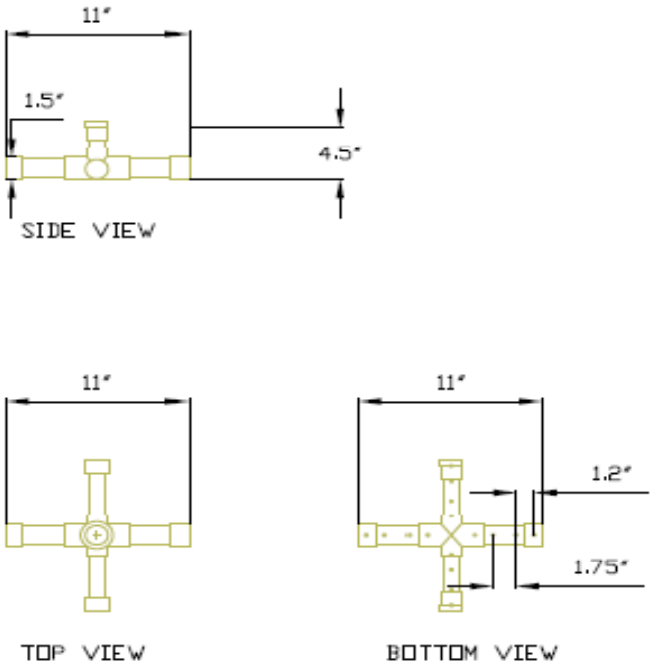

Figure 4-5: Multipoint liquid distributor.

The 25-delivery-point distributor was cross type distributor with six liquid delivery points in each arm and one liquid delivery point on the intersection of arms. The size of the liquid delivery nozzles was 0.3 cm. The distributor was installed at the top of the column in very close proximity of the packing to prevent water spreading to the column walls.

4.2 Electrical Resistance Tomography (ERT) System

The ERT system consists of three components; the sensor electrodes, the data acquisition system (DAS), and the host computer/image reconstruction system.

The electrode arrays consisting of six sensor planes were placed at equal intervals around the boundary of a circular column as shown in the Figure 4-6. The intervals were 0.30 m between the planes. Each sensor plane contains 16 stainless steel electrodes, and each electrode was 20 mm high, 30 mm wide and 1 mm thick.

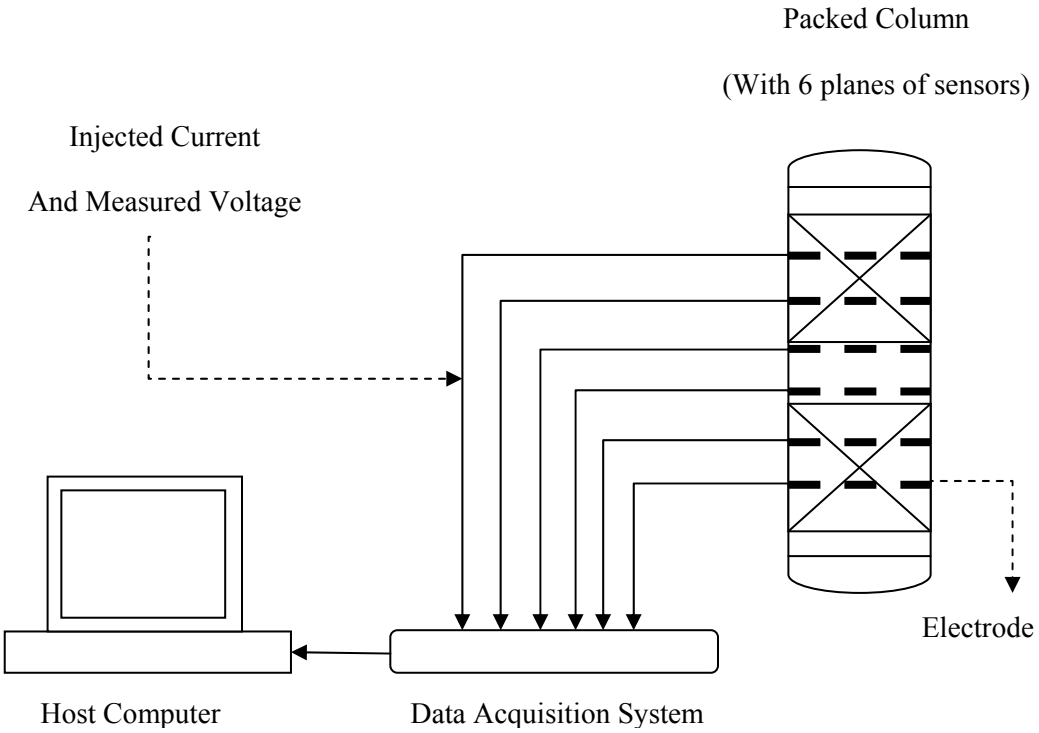

Figure 4-6: Schematic diagram of electrical resistance tomography system

The planes were numbered from top to the bottom. The electrodes were connected to the DAS (Industrial Tomography System, ITS, Manchester, UK) using a network of co-axial cables terminating with four 36-pin centronix connectors.

The Data Acquisition System (DAS) is responsible for obtaining the quantitative data describing the state of the conductivity distribution inside the column. The data must be collected quickly and accurately in order to track small changes of conductivity in real-time thus allowing the image reconstruction algorithm to provide an accurate measurement of the true conductivity distribution.

The P2000 has an injection current range of 0 to 75 mA which is divided into 3 broad bands (0-1.5, 1.5-15, 15-75) with 256 step changes possible. Also, to accommodate a wide range of material conductivities and to improve the accuracy for slowly changing processes, a range of injected current frequencies is provided. The P2000 can operate within the frequency range 75 to 153.6 kHz (in 12 steps). A P2000 ERT system (Industrial Tomography System – ITS, Manchester, UK) was used in this research.

The main specifications of the DAS were: frequency, 75-153.6 kHz; injecting current range, 0-75 mA (peak-peak); frame speed, <20ms; output voltage range, 10V to +10V; and voltmeter sensitivity, 0.0488 mV. The ERT system operates to a spatial resolution around 5% of the column diameter, using 16 equispaced electrodes (Holden et al., 1998). The DAS measurements, connected to a computer (Pentium 4, CUP 2 GHz, and 512 MB of Ram) via a nine-pin communication port, can be recorded through ITS ‘ERTWIN’ software (Industrial Tomography System – ITS, Manchester, UK) for control, image reconstruction, and data storage.

4.3 Experimental Procedure

The system is designed to be run in trickling down-flow mode (from top to bottom) and full liquid up-flow mode (from bottom to top). Experiments were performed at flow rates of 3,6, and 9 gpm (0.27×10^{-2}, 0.54×10^{-2} and 0.8×10^{-2} m^3/m^2 s) for the full liquid flow mode and 3 and 6 gpm (0.27×10^{-2} and 0.54×10^{-2} m^3/m^2 s) for the trickle flow mode. A 350 L feed tank filled with tap water and a pump fed water to the column. Switching between both types of flow modes by opening or closing valves as showing in the Figure 4-1 and Figure 4-2. The amount of flow rate was controlled manually by adjusting valve 2.

ERT system configuration settings used in the study as follow:

1. Sampling interval = 100 ms
2. Maximum no of frames = 161
3. Samples per frame = 8
4. Frame per download = 1
5. Injection current = 15 mA

Experiments were performed whereby a high conductivity tracer was introduced into the inlet feed by direct injection using a syringe containing 100 ml of sodium chloride (concentration c, 100g/L, conductivity, 200 mS/cm) to the tracer injector as showing in Figure 4-7 and Figure 4-8.

The ERT system produces a cross-sectional image using a P2000 windows-based software package that communicates to the DAS via a standard serial port connector. The software enables the user to calibrate the DAS, collect the voltage measurement, reconstruct (in real-time) the tomographs as well as reviewing past data. The software is versatile in that the data can be represented in a number of ways as shown in Figure 4-7.

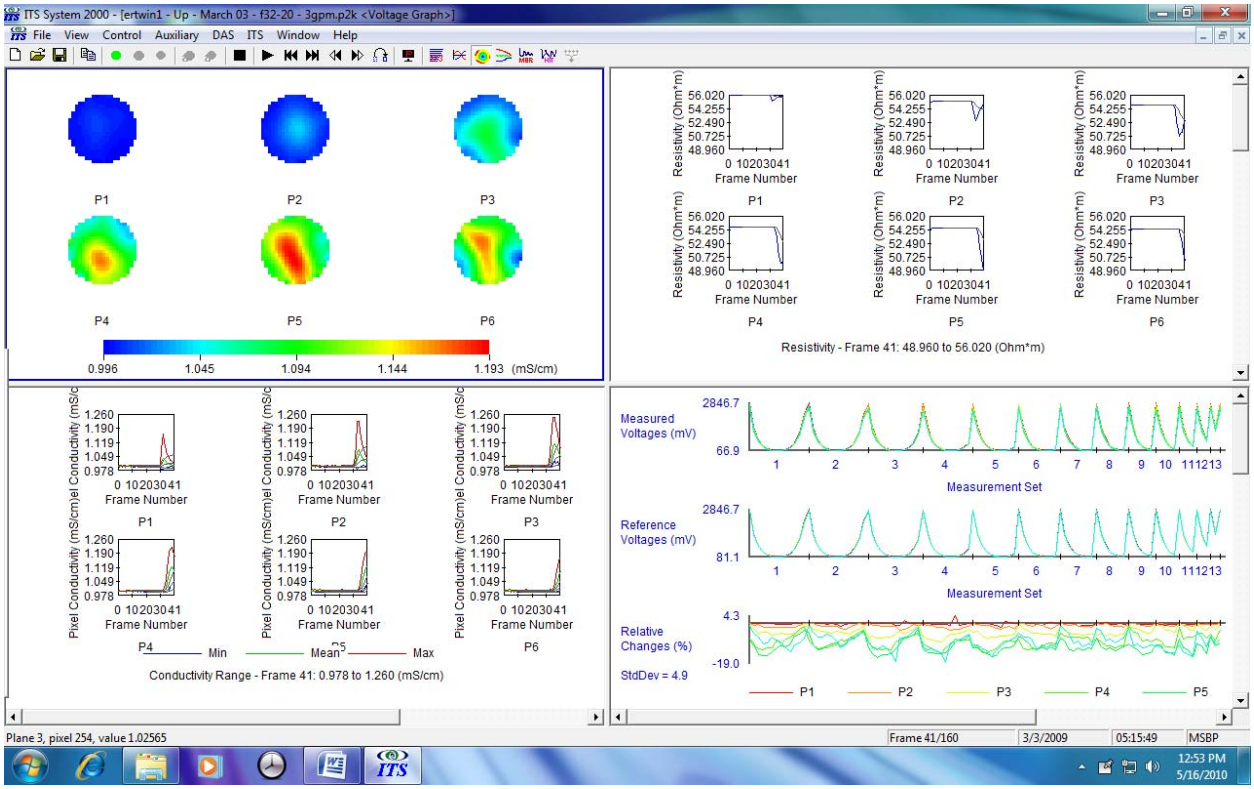

Figure 4-7: Screen shot of ITS windows-based software

The window is separated into four quadrants showing (starting from the top left moving clockwise) the reconstructed tomographs (six planes), the bulk resistance for each plane, measurement voltage data and conductivity data for each plane. All the data presented through the software is exportable enabling post-experimental data analysis. Measurements were collected from the six planes of electrodes.

Figure 4-8 and Figure 4-9 show an example of the generated tomographic images from the six measurement planes some time after injection of the high conductivity tracer for 3 gpm of full liquid flow and trickle flow.

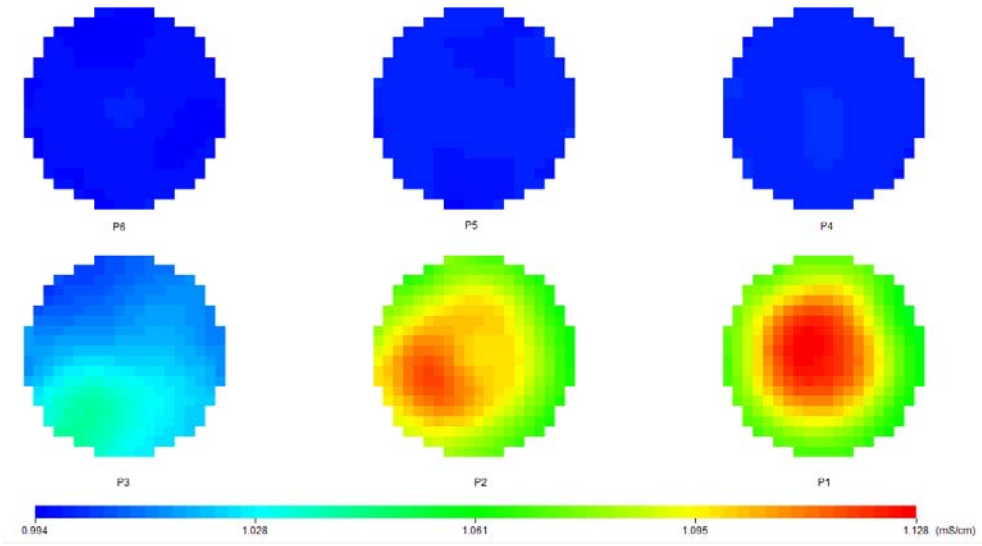

Figure 4-8: Tomographic images for 3 gpm of full liquid up-flow (P1: at the bottom, P6 at the Top)

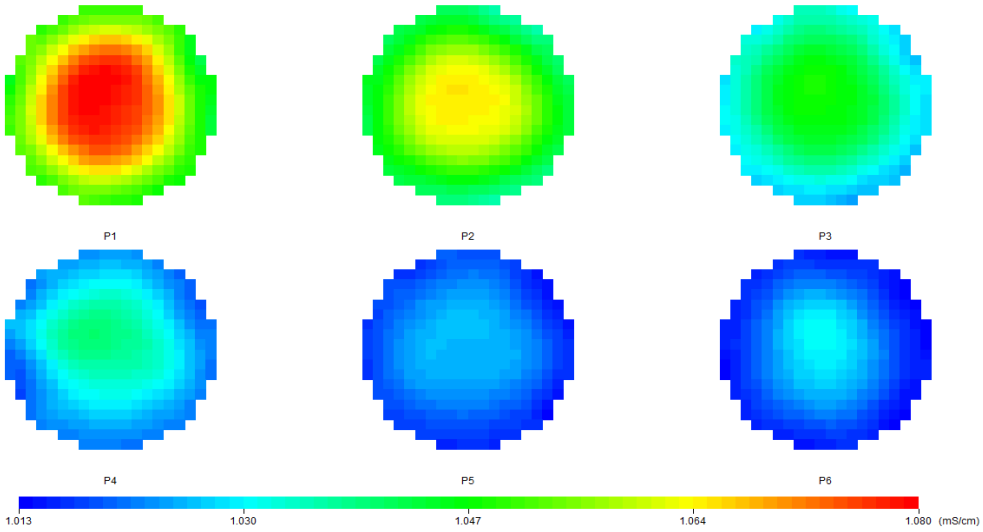

Figure 4-9: Tomographic images for 3 gpm of trickle down-flow (P1: at the top, P6 at the bottom)

In the Figure 4-8, the bottom right image corresponds to the measurement plane at the bottom of the column (plane 1) and subsequent images from right to left and bottom to top representing measurements planes towards the top of the column with the top left image corresponding to the measurement plane at the bottom of the column (plane 6).

In the Figure 4-9, the top left image corresponds to the measurement plane at the top of the column (plane 1) and subsequent images from left to right and top to bottom representing measurements planes towards the bottom of the column with the bottom right image corresponding to the measurement plane at the bottom of the column (plane 6).

The images show in the Figure 4-8 and Figure 4-9 can be export as numerical data in MS Excel format file by using ‘File/ export data’ parameter in the menu bar of P2000 software window as shown in Figure 4-7. The time that the tracer is within each measurement of group1, 3 gpm for bottom to the top flow can be calculated from the exported data shown in Table 4-1. From the data set in Table 4-1, using cross correlation method, the axial velocity component and liquid distribution factor were calculated as shown in next chapter.

Table 4-1: Exported pixel trace data of 3 gpm for bottom to the top flow

	Conductivity (mS/Cm) of Group 1 in 6 Planes					
Time, S	**G1,P6**	**G1,P5**	**G1,P4**	**G1,P3**	**G1,P2**	**G1,P1**
1	0.999596	0.999538	0.999648	0.99992	1.00003	1.00022
2	0.999382	0.999379	0.999663	0.999836	1.00019	0.999647
3	0.999504	0.999063	0.999919	0.999561	0.999848	1.00024
4	0.998827	0.999456	0.999936	0.99997	1.00037	0.999718
5	0.998315	0.9992	1.00009	0.999367	1.00006	0.999595
6	0.998629	0.999544	1.00016	0.99973	1.00006	0.999885
7	0.998407	0.999196	0.999604	0.999556	1.00011	0.999717
8	0.998125	0.99953	0.999726	0.999274	0.99999	1.00017
9	0.998285	0.999113	0.999724	0.999896	1.00036	1.00015
10	0.998223	0.999113	1.00008	0.999785	1.00029	1.00032
11	0.997875	0.999219	0.99994	0.999737	1.0003	1.00036
12	0.997683	0.99911	0.999709	0.999741	1.00075	1.00055
13	0.997873	0.998726	0.999894	0.999844	1.00033	1.00059
14	0.997766	0.9991	1.00007	0.999923	1.00026	1.00064
15	0.997663	0.99913	0.999583	0.999609	1.00023	1.00064
16	0.997598	0.999245	1.00017	0.999615	1.00029	1.00108
17	0.997059	0.999102	0.999828	0.999139	1.00012	1.00038
18	0.9977	0.998776	0.999477	0.999303	1.00052	1.00051
19	0.997193	0.998877	0.999695	0.999713	1.00066	1.00087
20	0.997167	0.998678	1.00025	1.00072	1.00039	1.00098
21	0.997243	0.99937	1.00005	0.999736	1.00003	1.00077
22	0.997467	0.998887	1.00001	0.999743	1.00073	1.00077
23	0.996606	0.999044	1.00021	0.999816	1.00037	1.00076
24	0.99674	0.998473	0.999921	0.999898	1.00088	1.00038
25	0.996102	0.998825	0.999666	0.99955	1.00038	1.00104
26	0.996643	0.998989	0.999326	1.00039	1.00074	1.00107
27	0.996312	0.999029	0.999771	1.0001	1.00067	1.00105
28	0.996513	0.998777	1.00024	0.999815	1.00054	1.00209
29	0.996429	0.998858	0.999872	0.999889	1.00085	1.00862
30	0.996556	0.998937	0.999745	0.99971	1.00096	1.03812
31	0.996255	0.998605	0.999768	1.00027	1.00064	1.08574
32	0.99638	0.998444	1.00018	0.999905	1.0008	1.12256
33	0.996222	0.998437	1.00033	1.00015	1.00088	1.13943
34	0.996269	0.998824	1.00035	1.00004	1.00092	1.14314

4.4 Velocity Profile Measurement

Measuring the fluid velocity in a packed column is a complicated task. Although Darcy Law has been extensively used by many researchers to evaluate fluid velocities in porous matrix but applying this concept to packed column was not the motive of this study. In this study a novel technique to conduct velocity profile measurement was developed. The velocity was measured by means of pixel-pixel cross correlation of electrical resistance tomography after two dimension images had been reconstructed. The method to cross-correlate two adjacent planes is explained below as shown in Figure 4-10:

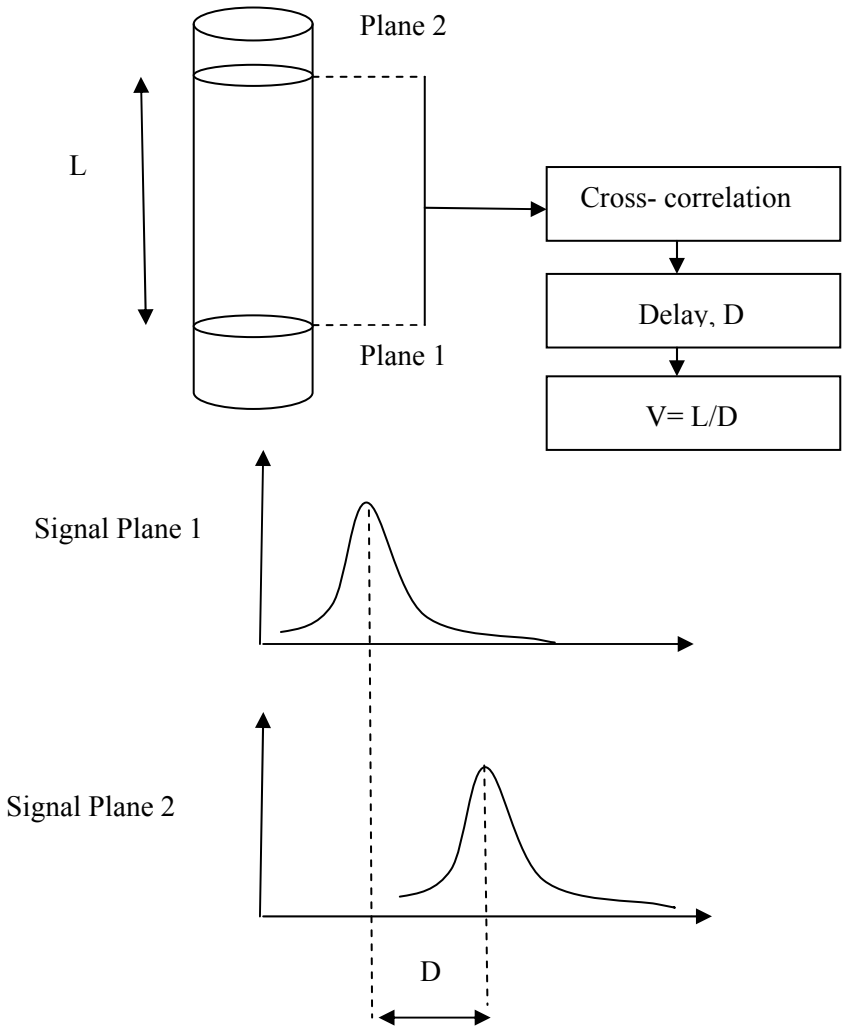

Figure 4-10: Velocity measurement by cross-correlation of ERT signals.

Figure 4-10 shows the schematic of a packed column with two adjacent planes. The injected tracer would be injected to plane 1 side in the inlet flow. The electrodes send signal to the data acquisition system indicating the time at which the tracer passes through that plane. The tracer then hits the second plane of electrodes after a delay as shown in two plots of signals for plane 1 and plane 2 in the Figure 4-10. By knowing this delay time velocity of the fluid within the column can be calculated by the following expression:

$$V = L / D \quad \ldots\ldots\ldots\ldots\ldots\ldots\ldots\ldots\ldots\ldots\ldots\ldots\ldots\ldots\ldots\ldots \quad (4.1)$$

Where L is the distance between the electrode planes and D is the time delay.

The fore-mentioned methodology was adapted to correlate between the pixels in adjacent planes. The tomographic image of each electrode generated by the ITS ERT system had a 20 x 20 matrix of reconstructed conductivity values. The generated images were of square grids with 400 pixels. To keep the similarity of generated images with the circular column, the square grid was transformed to a circular grid. This transformation resulted into a total of 316 pixels instead of 400. An example of transformed pixels for circular grid is shown below in Fig. 4-11

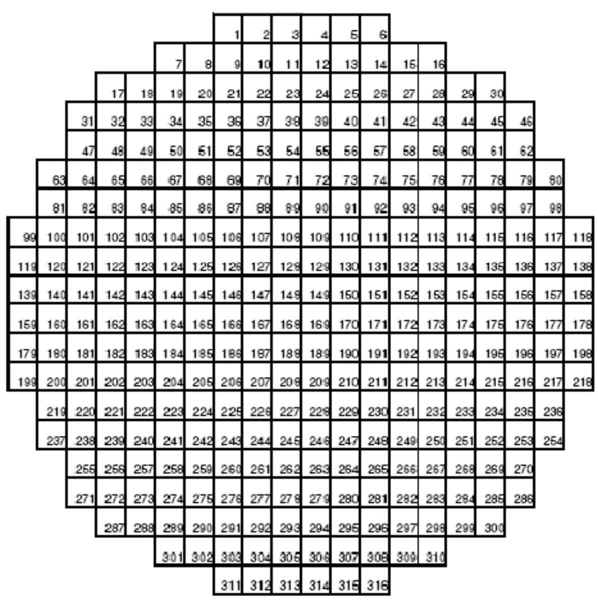

Figure 4-11: ERT tomographic image grid with 316 pixels

Ten groups of pixels were chosen for correlation. To distinguish between the groups, a unique color was assigned to each group. For example group 1 was colored red and group 10 was colored grey. Correlation between each of the 10 pixels within adjacent measurement planes resulted in evaluating 10 axial velocities. The color distribution of each group is shown below in Fig. 4-12.

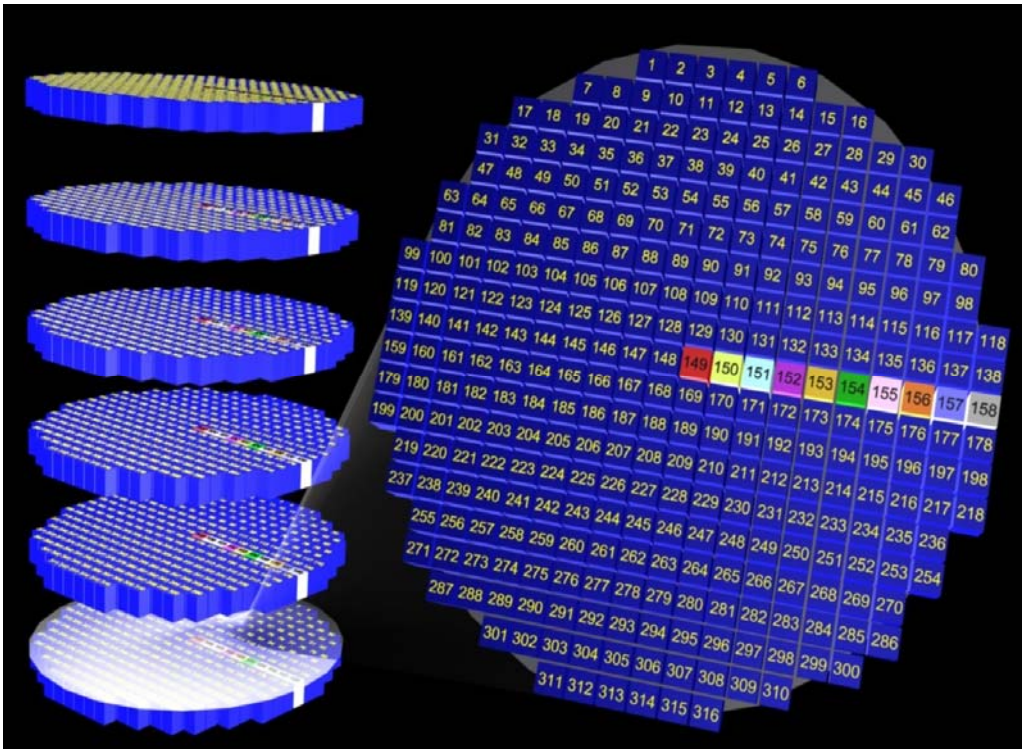

Figure 4-12: Tomographic image grid with pixel groupings in 6 planes

4.5. Liquid Distribution Measurement

Several techniques have been proposed in the literature to measure liquid distribution. In this study, electrical resistance tomography was employed to measure liquid distribution factor Mf. This method is based on pixel-pixel cross-correlation of electrical resistance tomography (ERT), to measure local liquid velocity of 10 groups of pixels through column cross section at equal spacing planes. In liquid distribution studies, a maldistribution factor is usually used to quantify the quality of flow through a packed bed. It is a measure of the severity of liquid maldistribution in a section of a packed column. When the liquid has a uniform distribution over the column cross section, Mf equal zero. A higher values of Mf means higher degree of liquid maldistribution

The liquid distribution factor proposed by Kouri and Sohlo (1987) was adapted in the present study. The factor is defined as an average standard deviation of individual liquid flows collected in the liquid collecting cells as below:

$$\mathrm{Mf} = \left(\frac{1}{\mathrm{n}}\sum_{\mathrm{i}=1}^{\mathrm{n}} \quad \left(1 - \frac{V_i}{V_{av}}\right)^2\right)^{0.5} \quad \ldots\ldots\ldots\ldots\ldots\ldots\ldots\ldots\ldots\ldots \quad (4.2)$$

Where V_i is the pixel group velocity, and V_{av} is the average velocity of the pixels through column cross section and n number of cells (where n equal 10 for the ERT method and 37 for the liquid collection method (LCM)).

For liquid collection method, a liquid collector was installed at the bottom of the column at 7.5 cm below the packing support as shown in the Figure 4-13. This was used for measuring flow distribution leaving the packed bed. It was designed to collect data not only over a cross sectional area of the bed, but also in various diagonal and concentric paths. The liquid collector was made of 37 collecting cells. Each collecting cell was a 15 cm high cylinder with a diameter of 3 cm. The bottom of each collecting cell was connected with a drain tube.

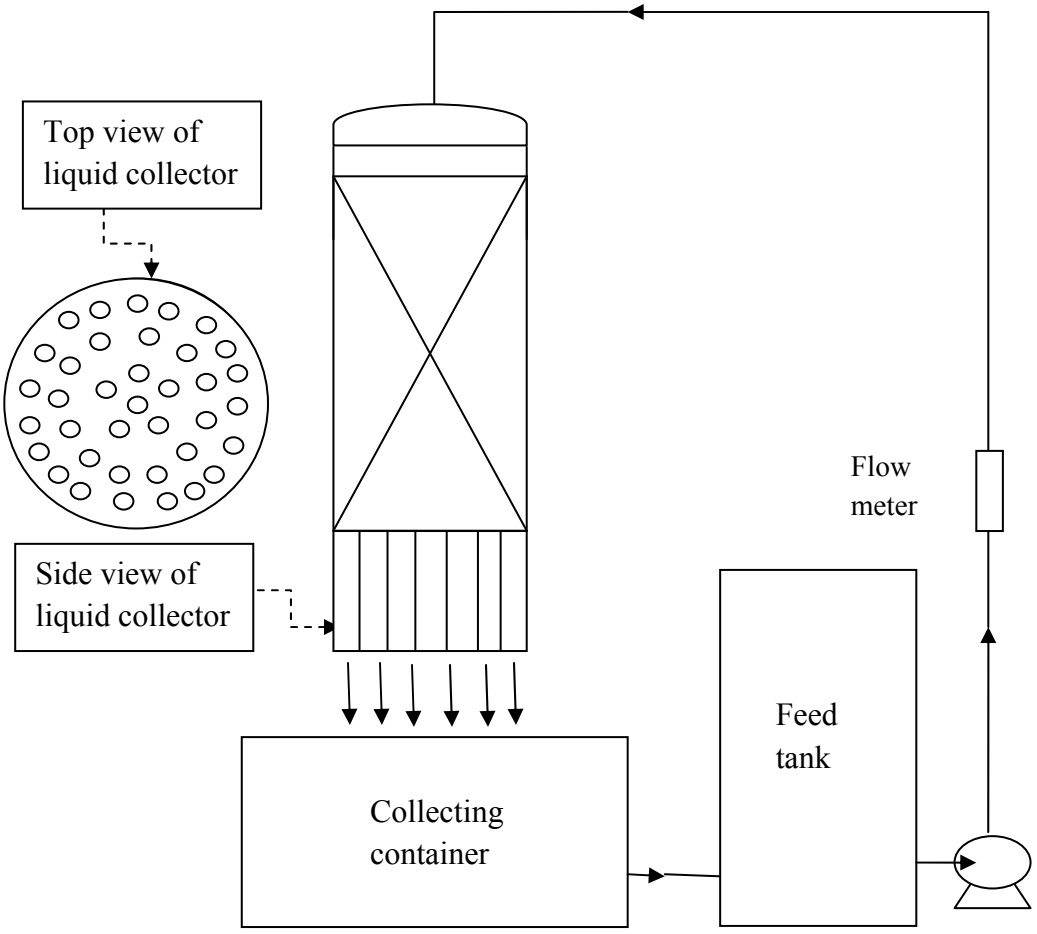

Figure 4-13: Schematic diagram of the collection method set-up

CHAPTER 5

5. RESULT AND DISCUSSION

5.1 Experimental Results for Velocity Measurements.

This section briefly discusses the findings of the experiments with a flow rate of 3gpm of trickle flow (top to the bottom flow) and for a flow rate of 3gpm of full liquid flow (bottom to the top flow).

The conductivity for group 1 in all six measurement planes for 3 gpm of trickle down-flow and full liquid up-flow for the duration of an experiment are shown below in Figure 5-1 and Figure 5-2 respectively.

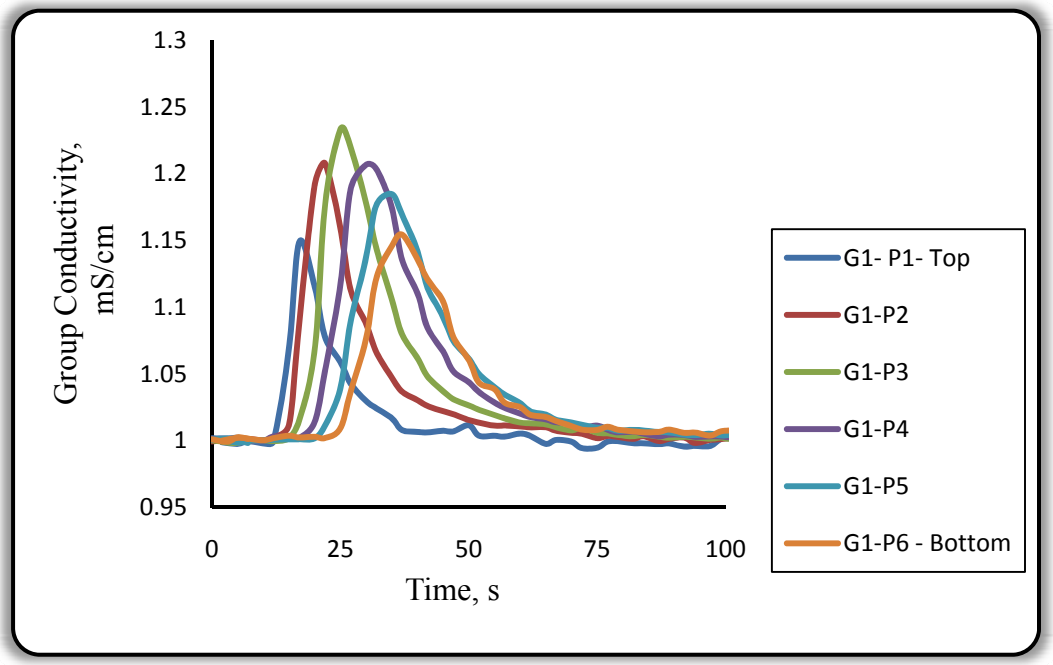

Figure 5-1: The conductivity of group 1, for liquid trickle down- flow at 3 gpm.

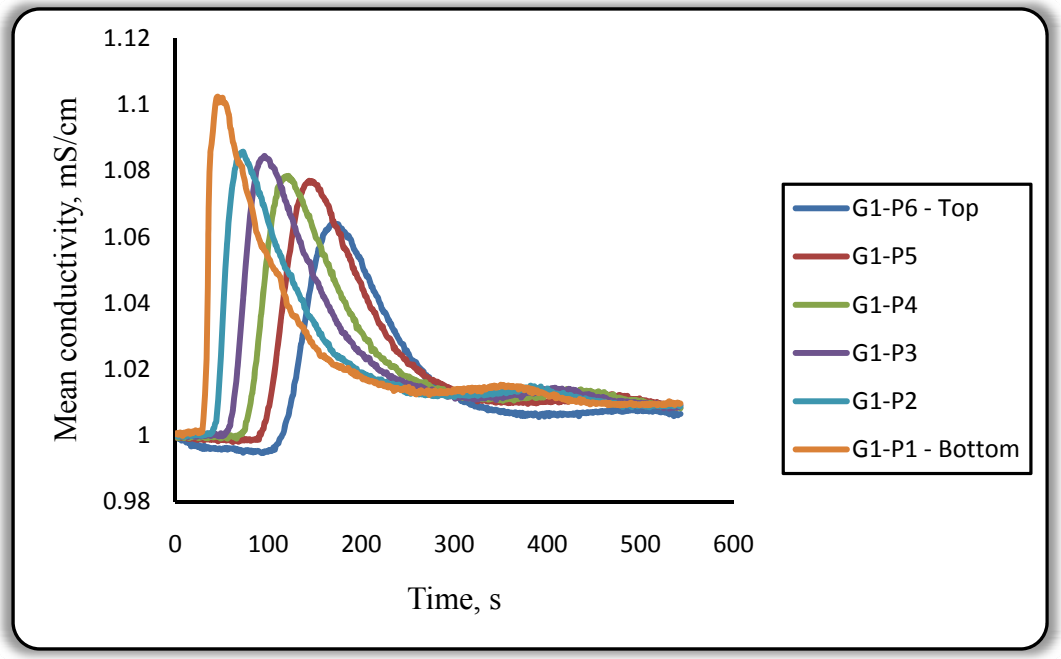

Figure 5-2: Mean conductivity of group 1, for full liquid up-flow at 3 gpm.

The maximum values of conductivity can be seen to follow the logical order of plane 1, through 6 as the high conductivity tracer moves vertically downwards from the injection point. These give the time duration for the maximum conductivity value to travel between given groups in adjacent planes, and thus knowing the distance between planes, it allows calculations of the local velocity from one plane to the next one.

The calculated velocities for group 1 for 3 gpm of full liquid up-flow and for trickle down-flow are shown below in Figure 5-3 and Figure 5-4. Similar plots can be obtained for groups 2-10. The data obtained for both types of flow modes with different liquid flow rates are tabulated in Appendix A and B.

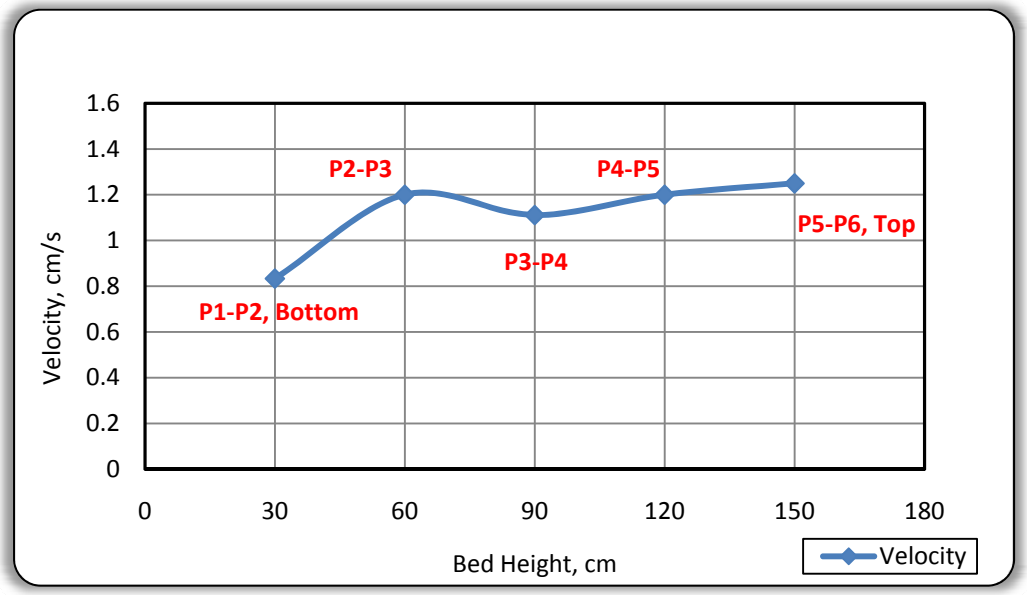

Figure 5-3: Velocity profile of group 1 for full liquid up-flow at 3 gpm.

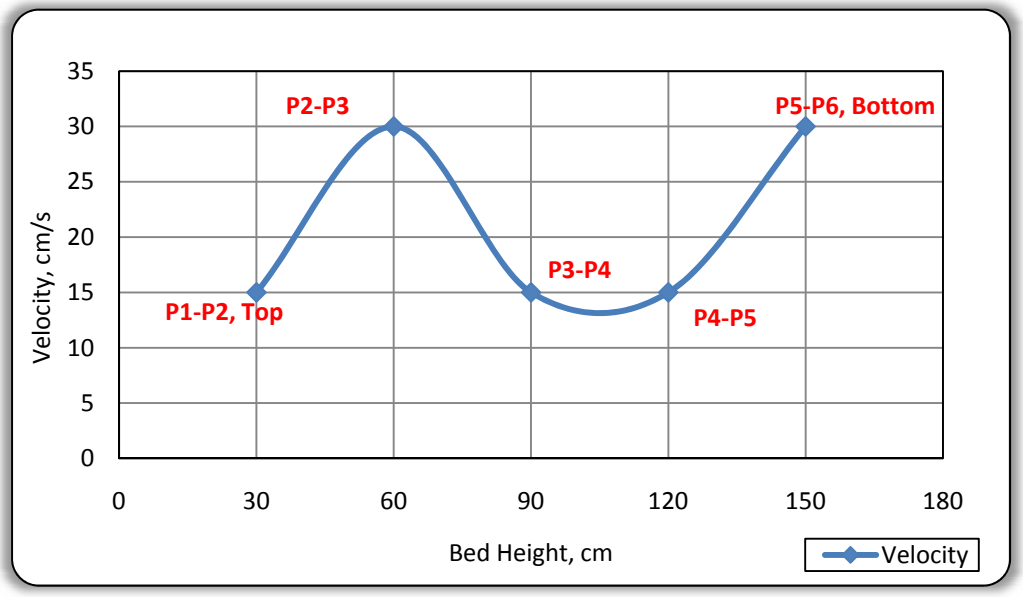

Figure 5-4: Velocity profile of group 1 for liquid trickle down-flow at 3 gpm.

The calculated velocities between adjacent measurement planes for the 10 groups of pixels at 3, 6, and 9 gpm for full liquid up flow and for trickle down flow are shown below in Figures 5-5, 5-6, 5-7, 5-8, and 5-9 respectively. The results of velocity profile for full liquid up-flow and trickle down-flow through the packings were far from uniform. The majority of velocity values of G1 to G10 (where G refer to group pixel) between plane 1 and 2 and plane 2 and 3 and so on were far from uniform towards column wall and top of the column, this finding supported by experimental work conducted on velocity distribution in packed beds that found the fluid flow is not uniform across a packed bed (Arthur et al., 1950; Morales et al., 1951; Schwartz and Smith, 1953; Bischoff, 1969, and Newell and Standish, 1973).

The explanation of the velocity profiles deviations from ideal flow due to the oscillation pattern of voidage through the packed bed resulting flow traveling at different velocities through the packed bed.

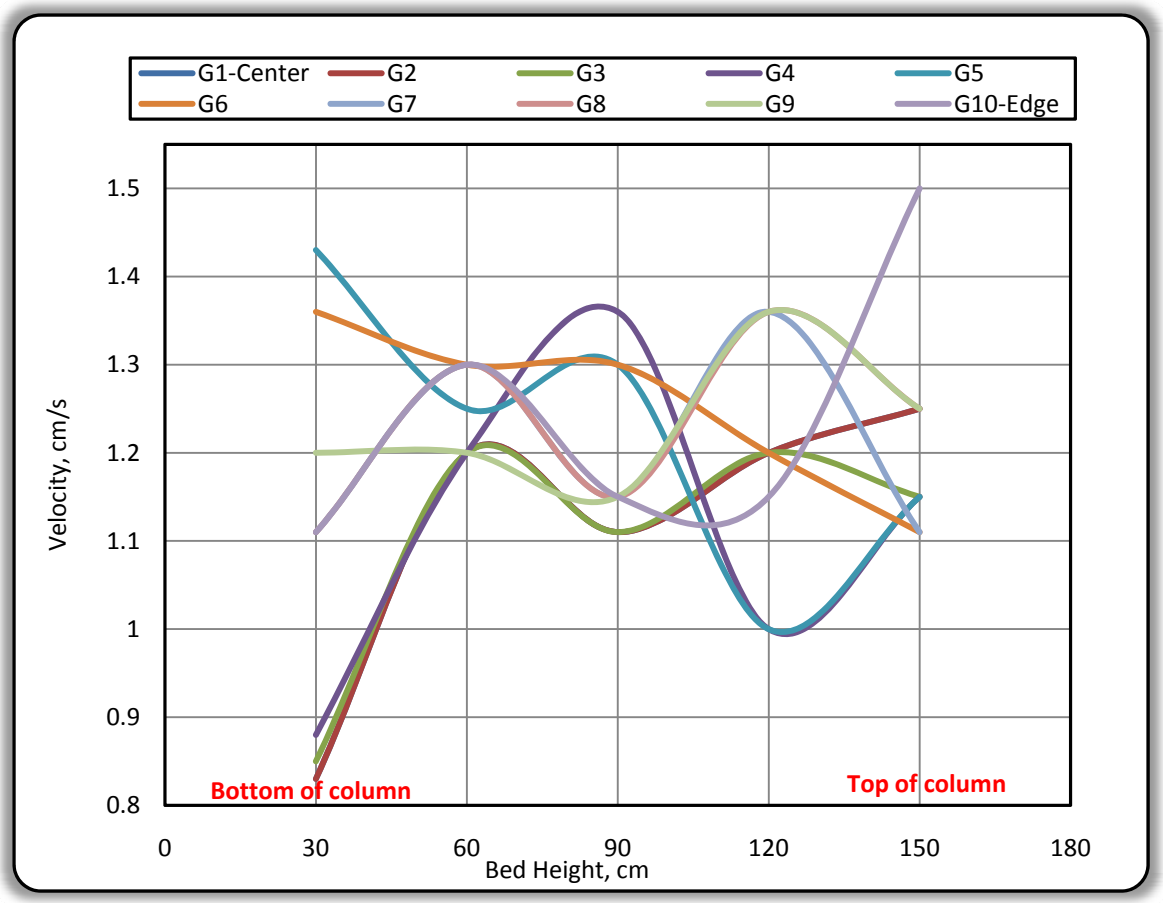

Figure 5-5: Velocity profile of 10 groups for full liquid up-flow at 3 gpm

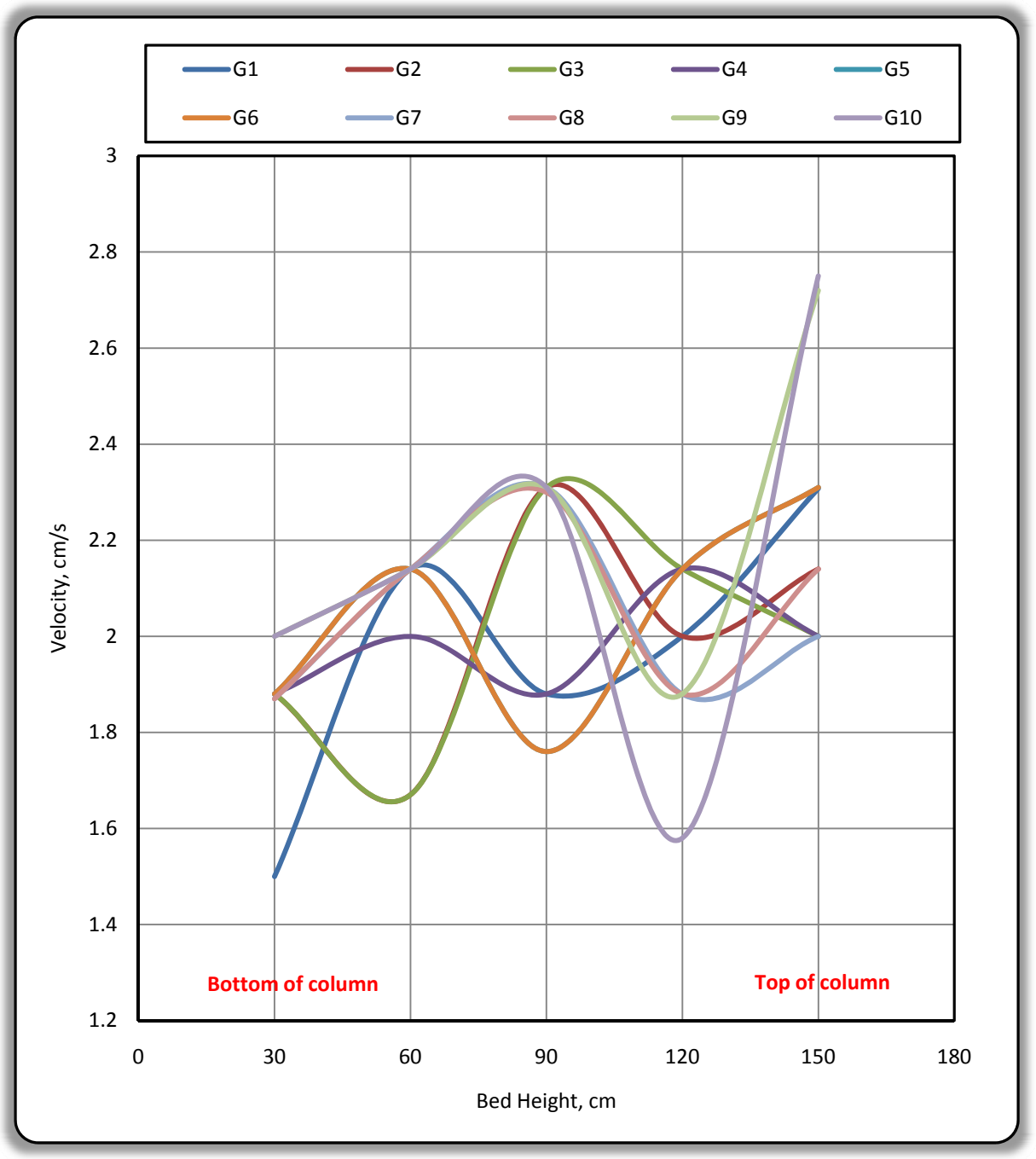

Figure 5-6: Velocity profile of 10 groups for full liquid up-flow at 6 gpm.

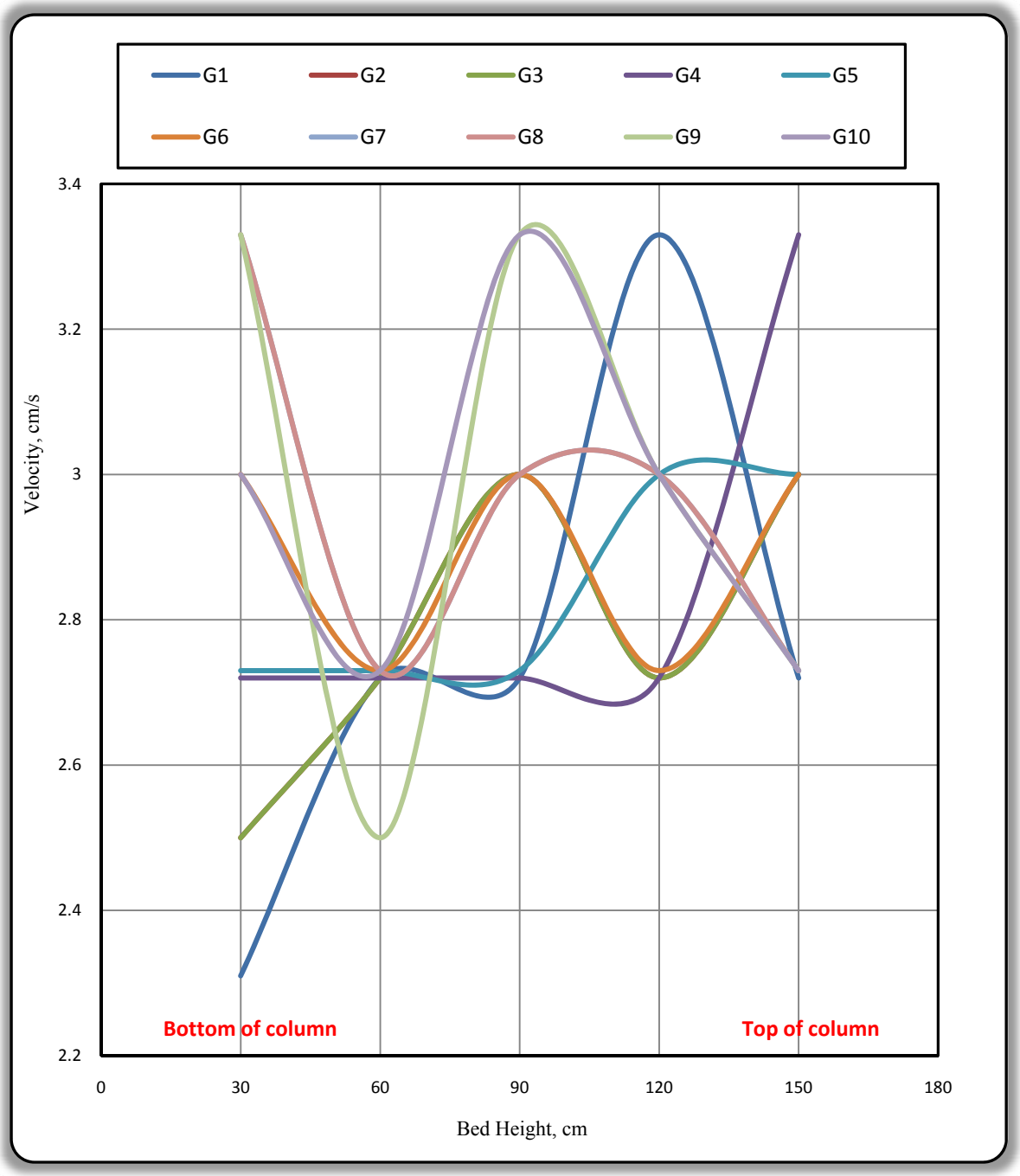

Figure 5-7: Velocity profile of 10 groups for full liquid up-flow at 9 gpm

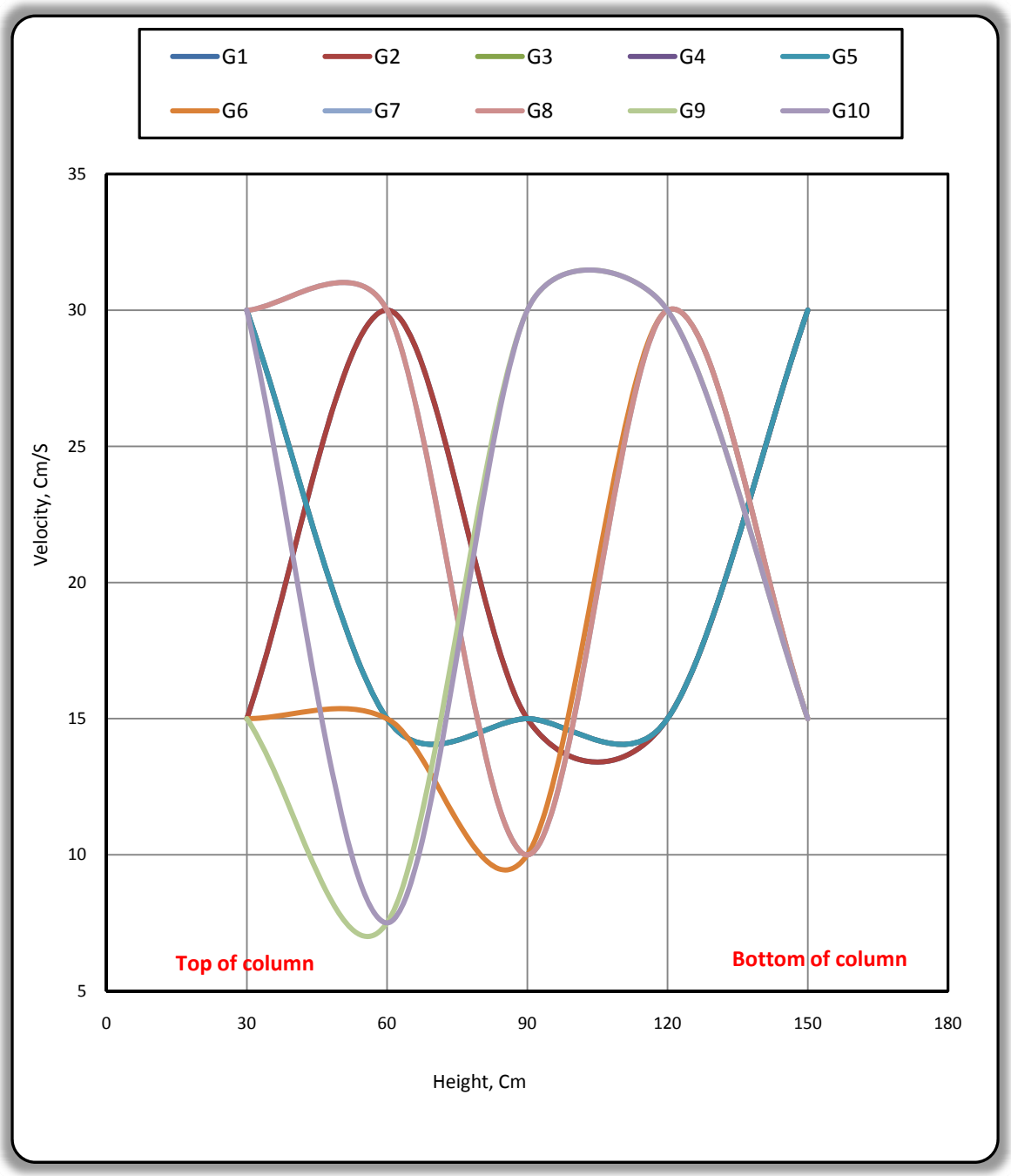

Figure 5-8: Velocity profile of 10 groups for liquid trickle down-flow at 3 gpm.

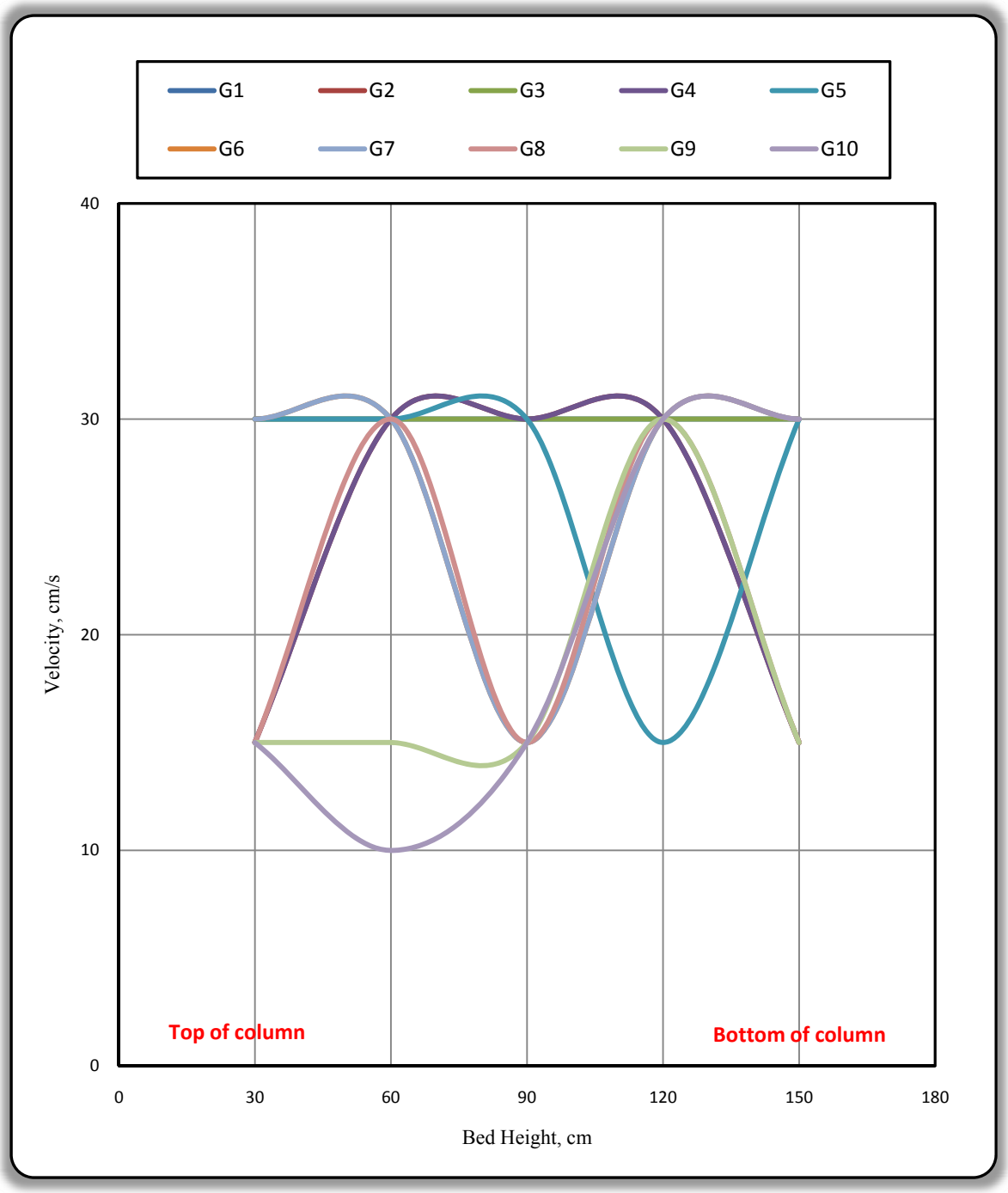

Figure 5-9: Velocity profile of 10 groups for liquid trickle down-flow at 6 gpm.

As shown in the Figure 2-3, Burdett et al., (1981) and Mak et al., (1991) explained the deviations from ideal flow can be classified in two types. In one type the elements of the flow travel through the apparatus at different velocities, causing channeling and dead zones.
For trickle down-flow, the velocity mgnitudes were higher than for the same flow rate of full liquid down-flow, as well as the velocity magnitudes through the bed are not distributed uniformly. The values of velocity for full liquid up-flow of 3 gpm were 0.83cm/s at (30cm), 1.2cm/s at (60cm) and 1.11 cm/s at (90cm) while the values of velocity for trickle down-flow of 3 gpm were 16.5 cm/s at (30cm), 22.5 cm/s at (60cm) and 24 cm/s at (90cm).

In the trickle flow regimes, the liquid is present as films, rivulets, pendular structures and liquid pockets over the packing particles, the latter two being highly stagnant in nature. Even for an "ideal" liquid distribution at the top of the column rivulets form downstream due to non-uniform porosity inside the packings that enhance channeling resulting in higher fluid velocity (Ravindra et. al., 1997).

The contact area between the sensors and the liquid is probably different for each sensor due to flow maldistribution. As well as at the point of contact between two packing particles, a pocket of stagnant liquid holdup is present. More neighboring particles result in an increase in the total stagnant liquid holdup held at the contact points. Therefore, there is an increase in the contact area between the probe and the stagnant liquid that result in different causing varied local velocities.

5.1.1 Accuracy of ERT Measurement

To approve the degree of precision of ERT measurements. The standard deviation determined between the computed velocity values of flow rates and velocity values measured by ERT technique. The standard deviation values at flow rates 3,6 and 9 gpm were 0.2, 0.14 and 0.12 respectively. This indicate the measured velocity by both methods is uniform (less dispersed) and acceptable. The standard deviation is less than or equal to the mean average of velocity values.

5.2 Experimental Results for Liquid Distribution Factor

The liquid flow distribution in packed column was measured by the maldistribution factor as a function of the packed bed height. The calculation of maldistribution factors was based on 10 pixels using ERT technique and 37 collecting cells using the liquid collection method (LC) over the column cross section. Maldistribution factors are calculated from the measured liquid velocities.

Figure 5-10 shows the calculated liquid maldistribution factors from velocities measured by ERT and LC respectively for a trickle down-flow at 3 and 6 gpm. The liquid distribution was far from uniform due to the radial variation of void through the packing

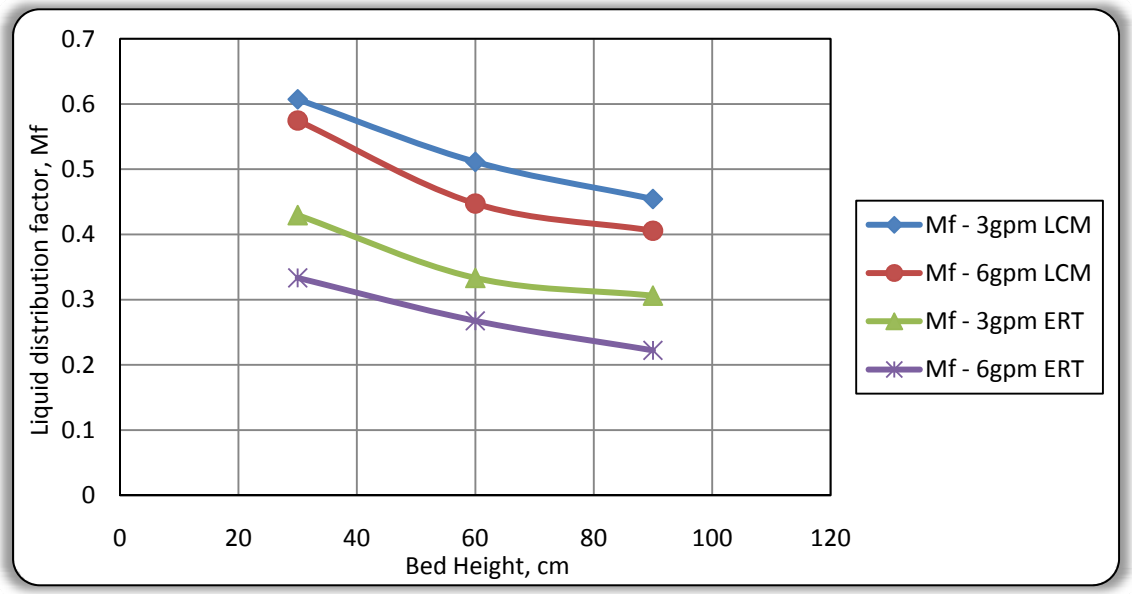

Figure 5-10: liquid distribution factor for a trickle down-flow at 3gpm and 6 gpm using ERT and LC

5.2.1 Effect of Bed Height on Liquid Distribution

The flow maldistribution studied by maldistribution factor (Mf) for different packed bed heights. The effect of bed height on the liquid distribution is shown in Figure 5-10 for the bed height 30 cm, 60 cm and 90 cm. As can be seen that Mf decreases with the bed height, at the packed bed height 90 cm, Mf reaches its minimum value of 0.45 and 0.30 at 3gpm for LC and ERT respectively. The behavior of maldistribution factor can be explained as: At the bottom of the column there is more liquid maldistribution, the liquid tend to move towards the column wall, and forms a higher wall flow resulting in a higher Mf. At about 90 cm the liquid flow distribution reaches a more developed state and the liquid wall flow reduced that result in a lower Mf. This result is in agreement with the result of Yin et al (2002) who showed that the bed height required for the liquid to reach its fully developed state.

5.2.2 Effect of Liquid Flow Rate on Liquid Distribution

The effect of liquid flow rate on liquid distribution is shown in the Figure 5-10 for the flow rates of 3gpm and 6gpm, respectively. The results shown in this figure that the liquid maldistribution reduced with the increase of liquid flow rate. At the top of the column, the value of Mf at 3gpm were 0.3 and 0.22 at 6gpm for ERT method and for LC method were 0.45 and 0.4. This observation is in agreement with the findings reported by Kouri and Sohlo (1987, 1996) and Al-Samadi et al (1989). Their results indicate that the higher flow rates tend to produce lower liquid wall flow. Thus, the liquid maldistribution will reduce accordingly and .

To shows how much variation or "dispersion" between ERT and LC measurement techniques. Standard deviation determined between the results for both methods. The standard deviation values at flow rates 3 and 6 gpm were 0.17and 0.21 respectively. The results of standard deviation indicates that the data points tend to be very close to each other that the values were less from the average of both methods as shown in appendix A and B.

5.3 Experimental Results for Liquid Distribution Symmetry

In order to investigate the symmetry of the liquid distribution profile, the radial liquid distribution was measured in two pathways for ERT and LC Methods, as shown in Figure 5-11 and Figure 5-12 respectively.

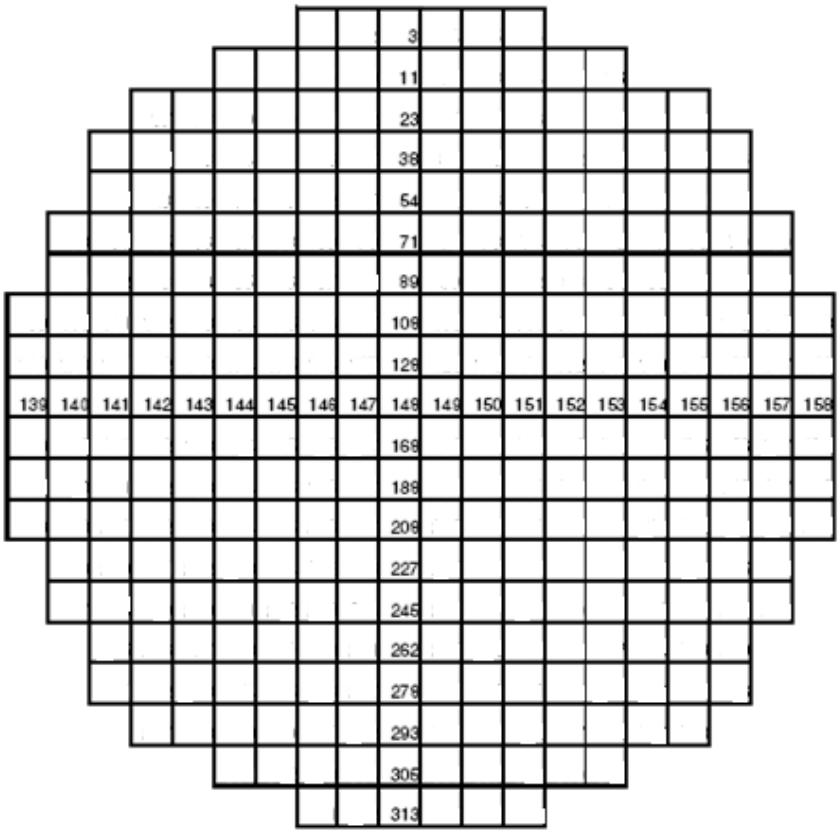

Figure 5-11: Radial paths of ERT method

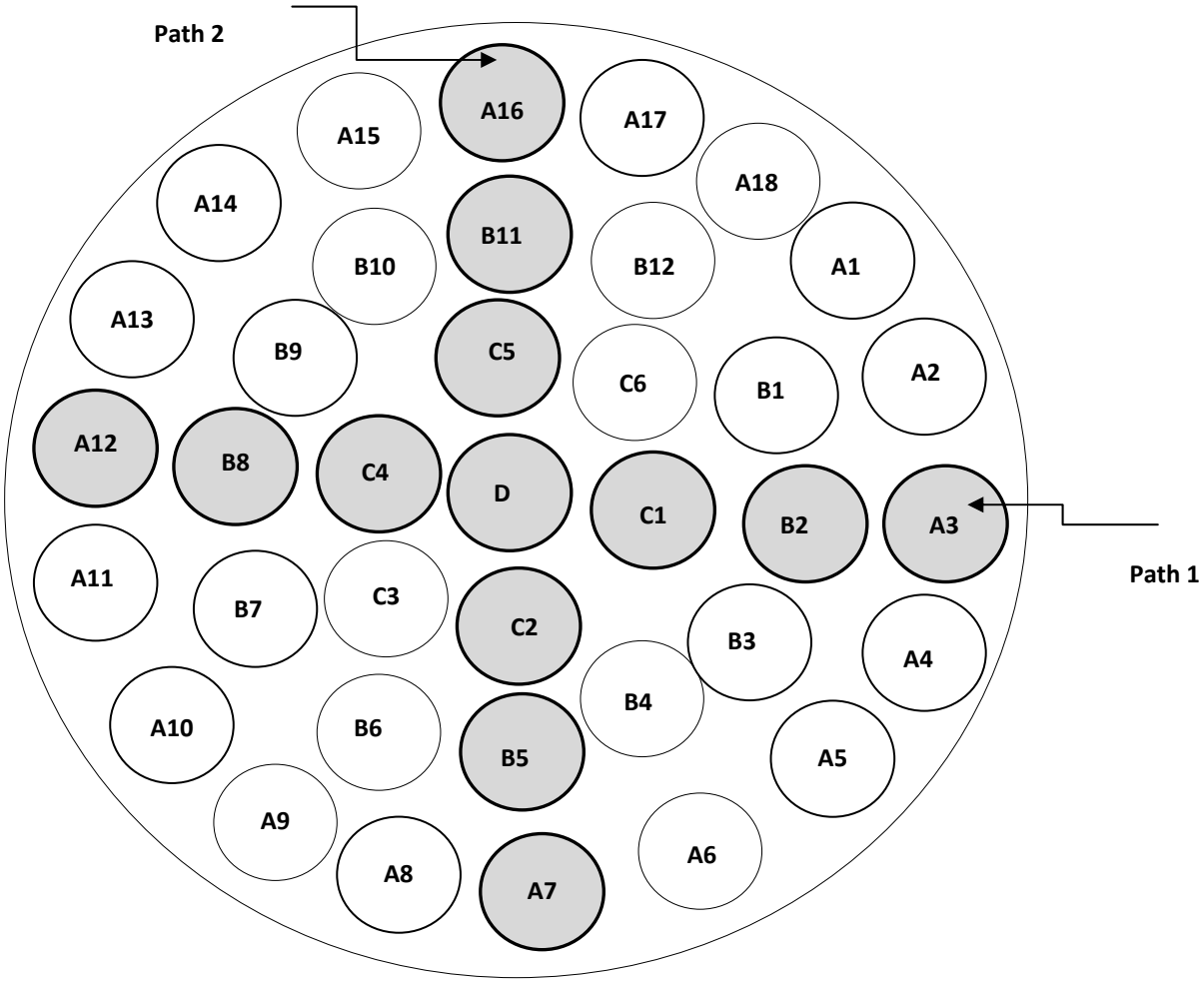

Figure 5-12: Radial paths of LC method

The results of liquid flow distribution measurement showed that the liquid distribution profile was not uniform. A plot of variation of liquid distribution with radial position is shown in Figures 5-13 and 5-14 for ERT and Figures 5-15 and 5-16 for LCM for two different liquid flow rates. Liquid distribution profile was based on 20 pixels using ERT technique and 7 cells collector using liquid collection method (LCM) over the column diameter. The figures reveal that the liquid distribution profiles are characterized by wavering behavior. Several investigators have obtained the same behavior of radial liquid distribution profile (Song et al., 1998; McGreavy et al., 1986; Ziolkowska et al., 1993).

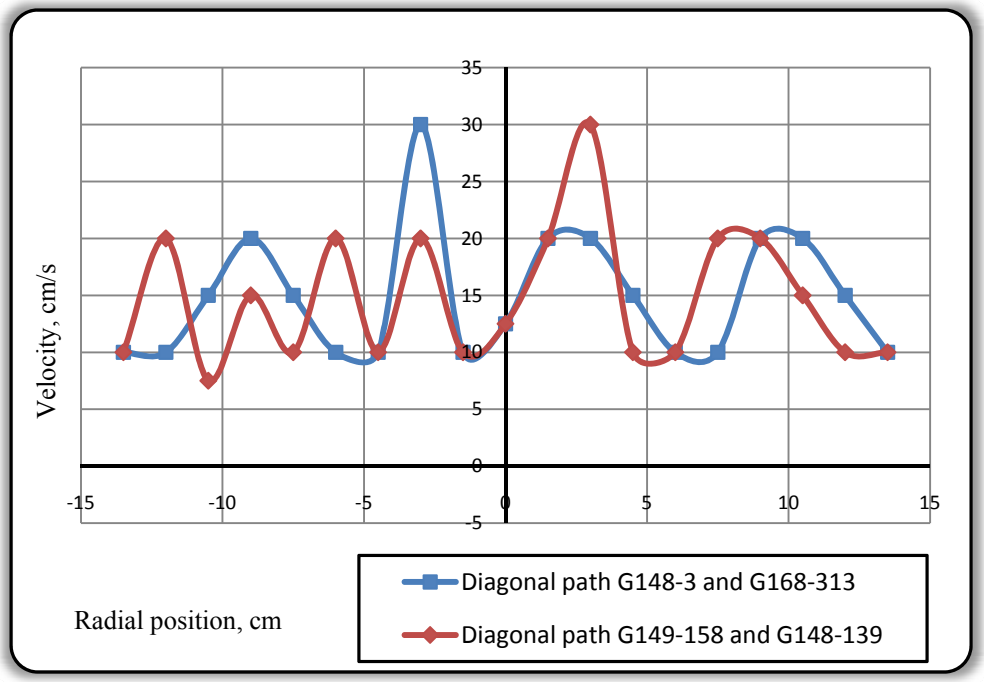

Figures 5-13: Liquid radial profile for 3 gpm of trickle down-flow, ERT method at bed height 90cm

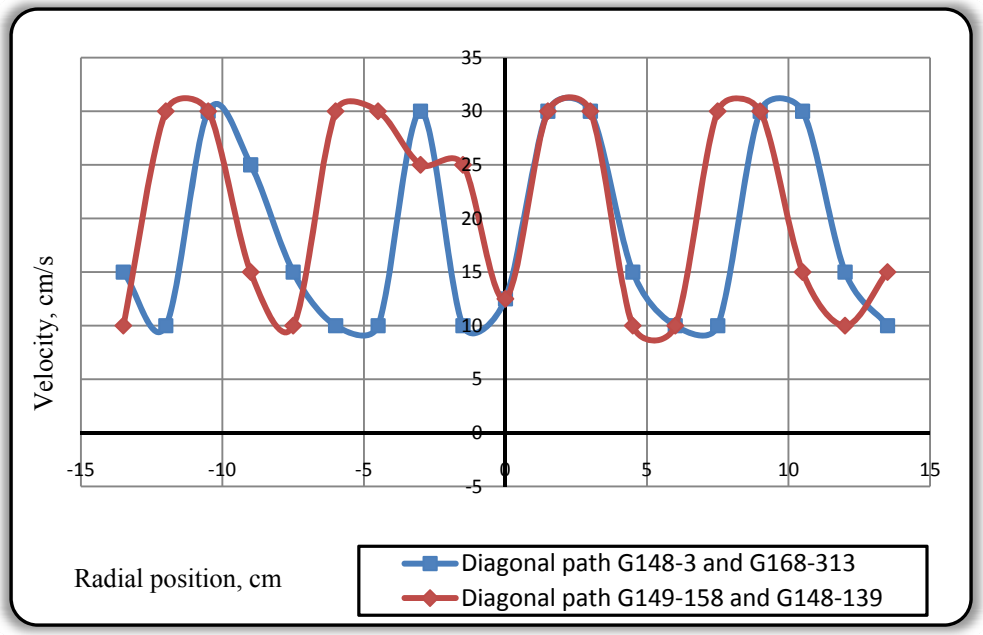

Figures 5-14: Liquid radial profile for 6 gpm of trickle down-flow, ERT method at bed height 90cm

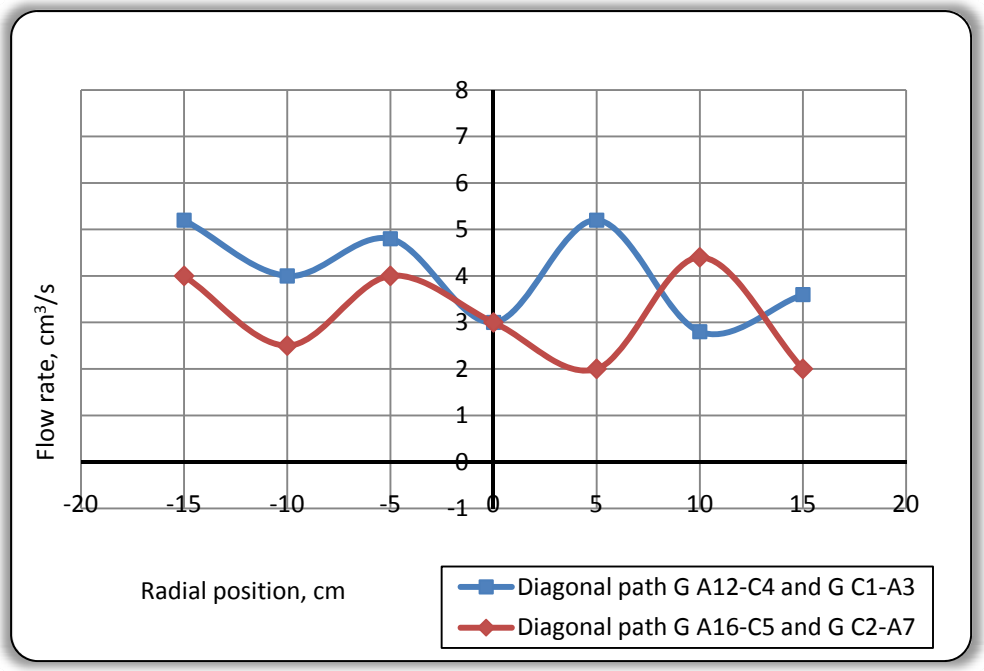

Figures 5-15: Liquid radial profile for 3 gpm of trickle down-flow, LC method at bed height 90cm

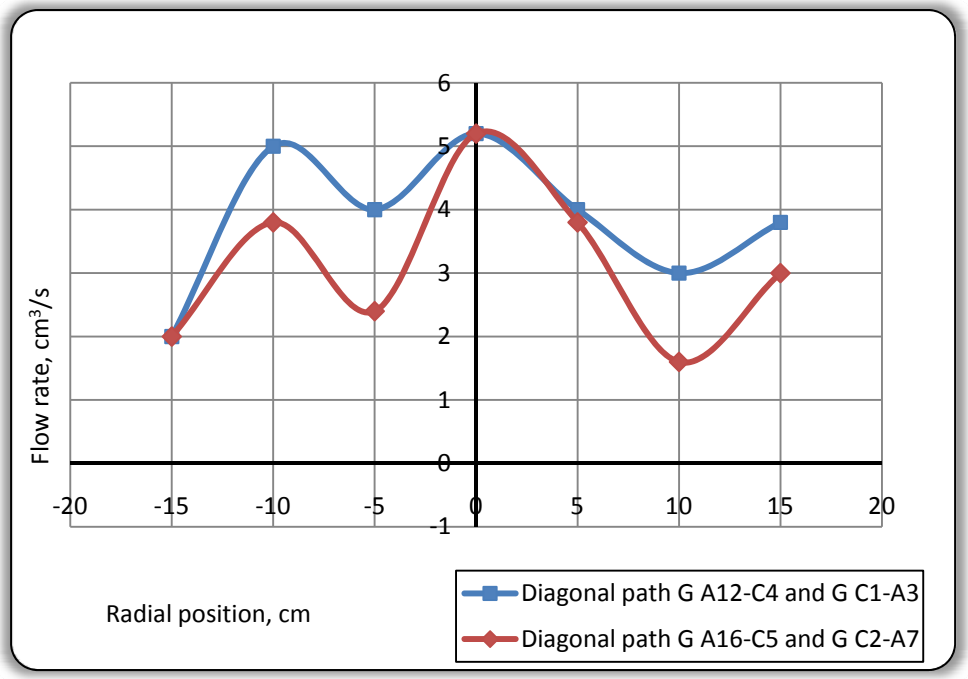

Figures 5-16: Liquid distribution profile for 6 gpm of trickle down-flow, LC method at bed height 90cm

Kunjummen et al., (2000) found that radial liquid velocity profile over any bed cross section was corresponded to the oscillation pattern of voidage at that radial direction. This finding was also supported by the mathematical model of velocity distribution of single-phase flow in packed beds, developed by Subaygo et al., (1998).

5.4 Flow Pattern Visualization

Flow visualization is a power tool in experimental fluid mechanics. The unique advantage of this technique is that certain properties of the flow field become directly accessible to visual perception and the insight into a physical process becomes clearer. Most fluids are transparent media and their motion remains invisible to the human eye during direct observations. However, the motion of such fluids can be recognized by making use of techniques by which the flow is made visible and such techniques are called flow visualization techniques.

The electrical resistance tomography (ERT) has been applied to visualize the flow pattern and distribution inside a random packed column. An image reconstruction algorithm is used to generate images of the distribution of materials within the sensing zone and data could be collected with sufficient temporal resolution to facilitate the tracking of an injected tracer and reconstruction of the flow patterns.

The conductivity tomogram displays a conductivity distribution for a circular sensor respectively. A color-scale is used to display the variation in conductivity. As shown in Figure 5-17.

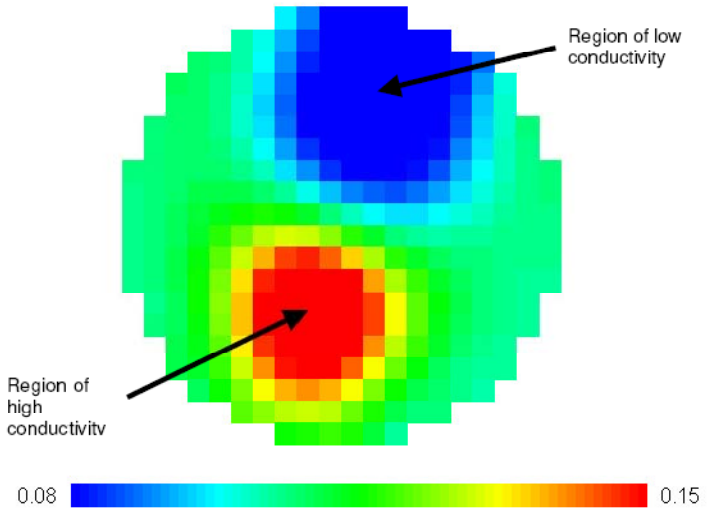

Figure 5-17: Tomogram shown region of high and low conductivity, (ITS, 2006).

Figure 5-18 shows sets of tomographic images representing slices through a packed column for a 6-plane of 3 gpm of full liquid up-flow, revealing the internal flow pattern.

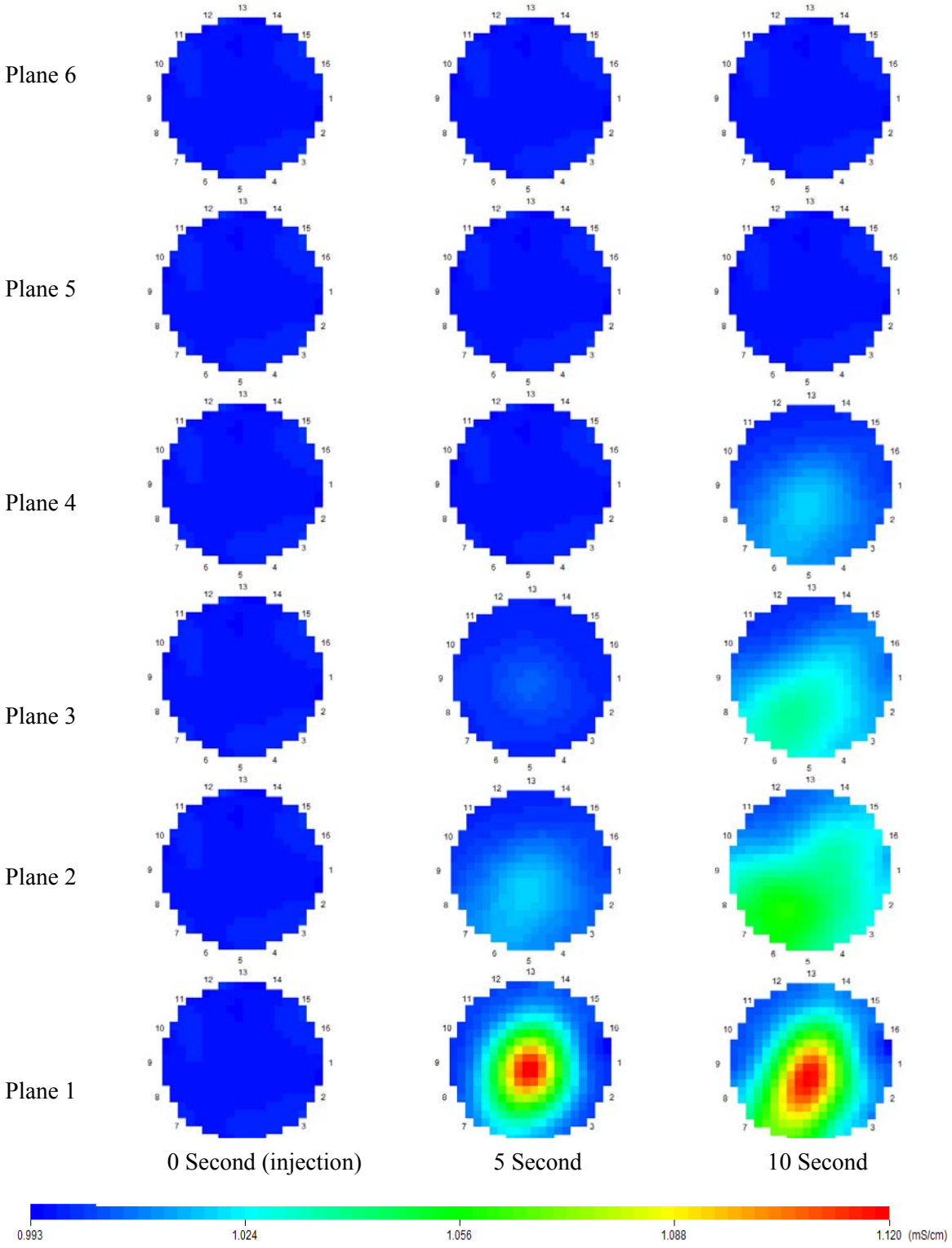

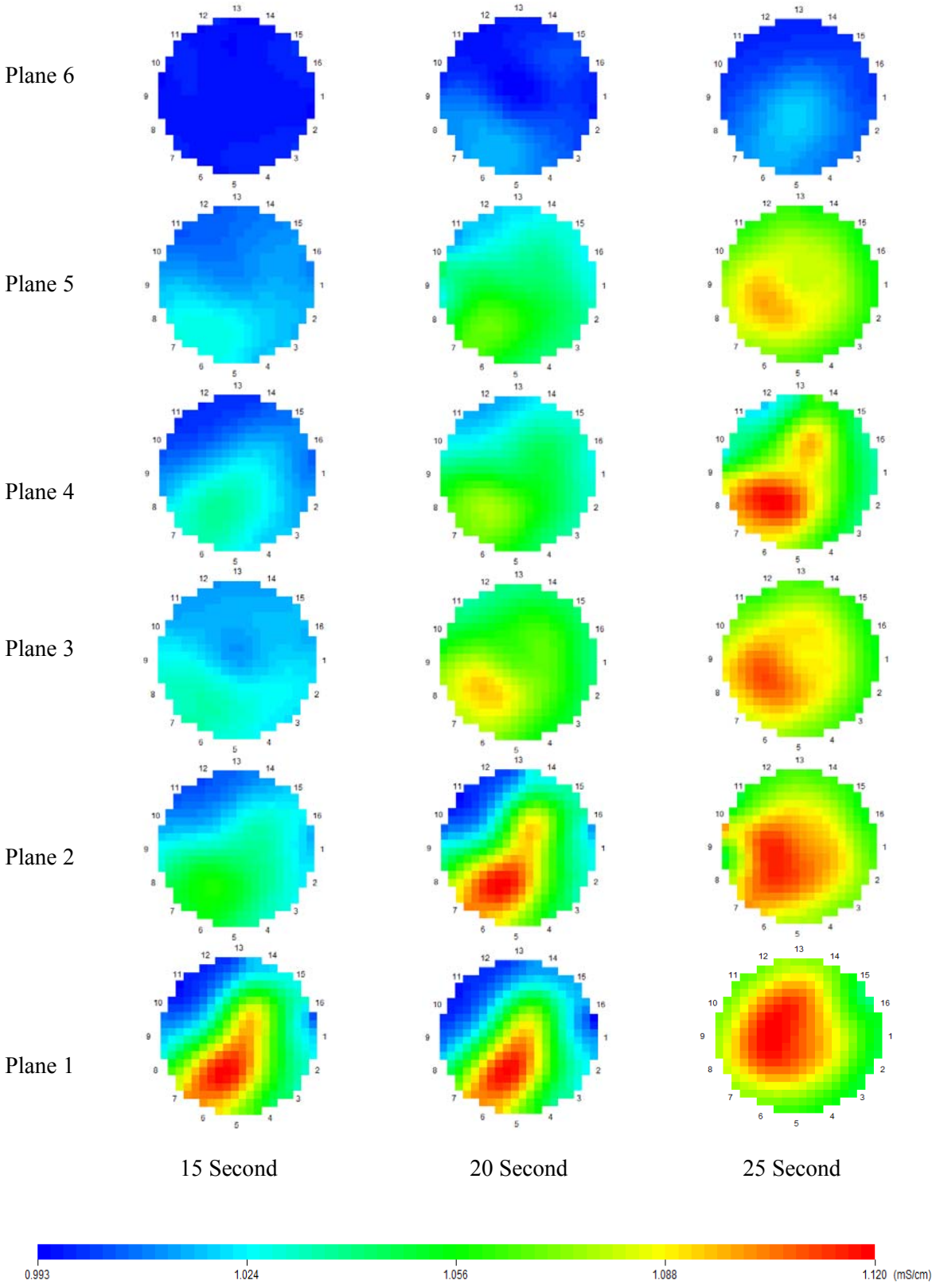
Plane 6
Plane 5
Plane 4
Plane 3
Plane 2
Plane 1
15 Second
20 Second
25 Second
0.993
1.024
1.056
1.088
1.120 (mS/cm)

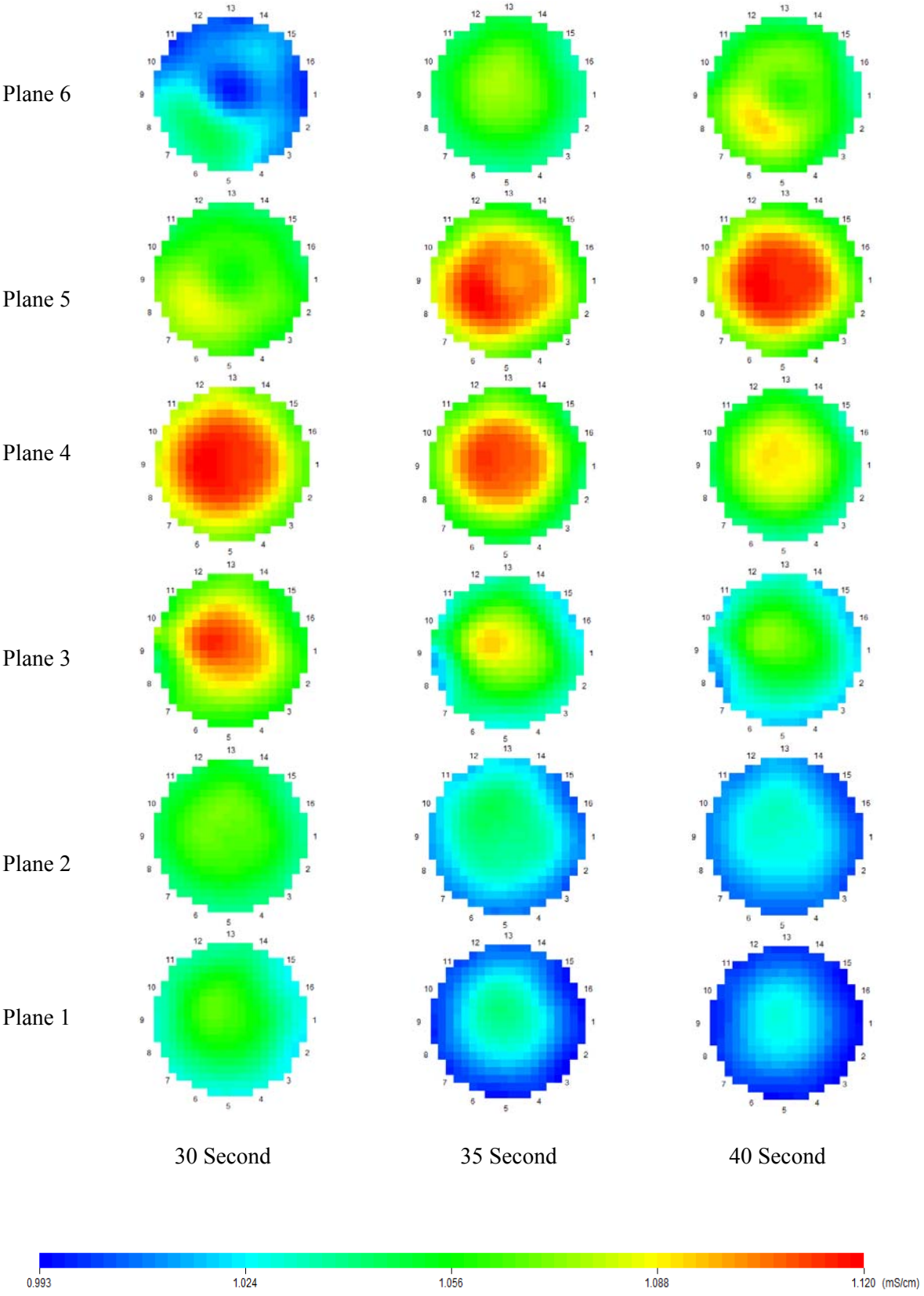
Plane 6
Plane 5
Plane 4
Plane 3
Plane 2
Plane 1
30 Second
35 Second
40 Second
0.993
1.024
1.056
1.088
1.120 (mS/cm)

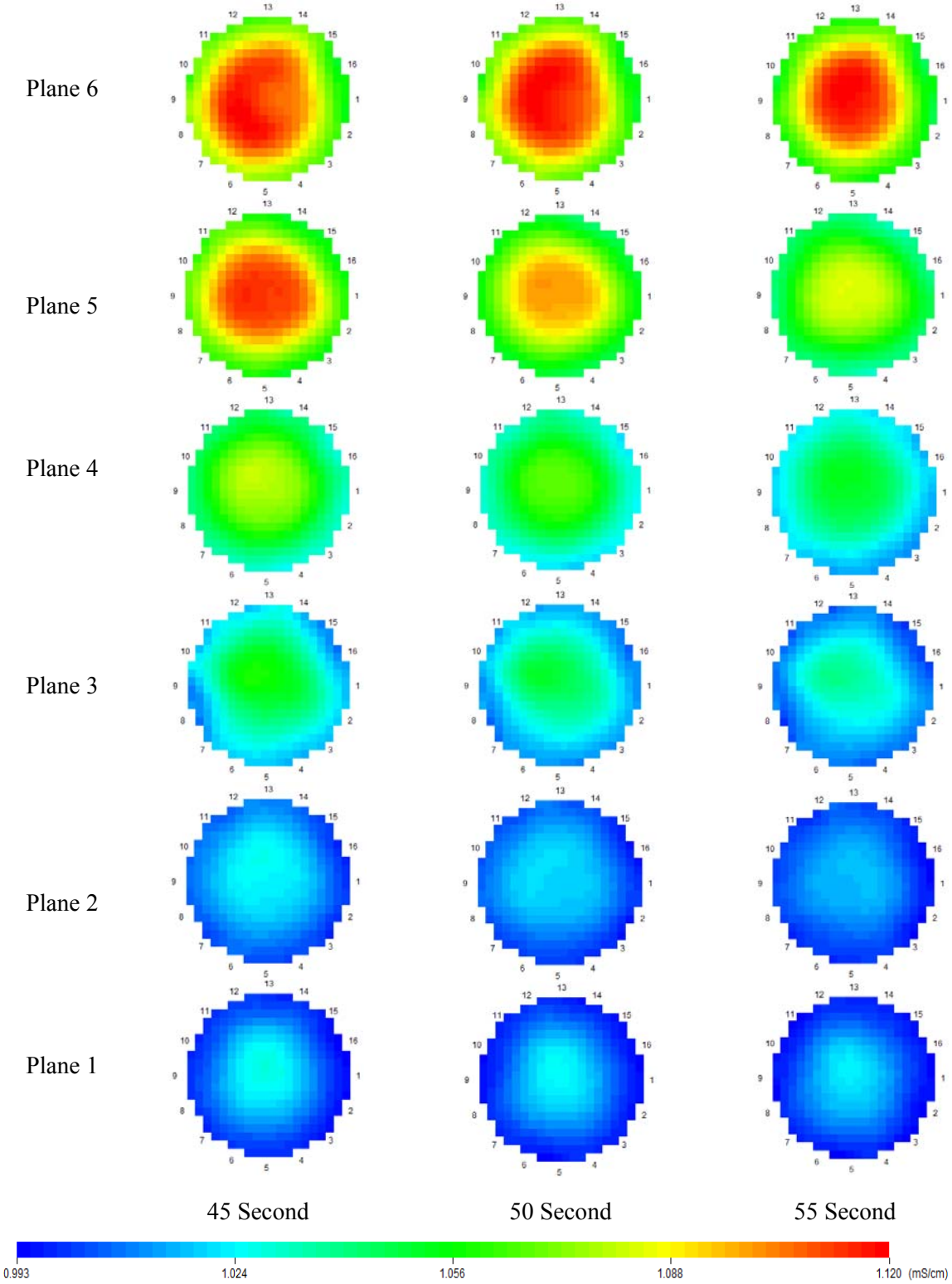

Figure 5-18: Sequence of ERT images showing liquid distribution inside the column of 3gpm of full liquid up-flow

Electrical resistance tomography was used for imaging electrical conductivity inside the packed column. Pulse injections of high conductivity tracer into the feed can be imaged as multiple tomographic images or 3D solid-body images that reveal the internal flow patterns.

In this study the flow and mixing of the tracer were tomographically captured in real time. The pulse progress was tracked as it enters the column and takes its tortuous but pre-determined path towards the exit.

A series of tomographic reconstructions for six measurement planes at equal intervals around the boundary of a circular column had been shown in Figure 5-18 and Figure 5-19. The image contains a region of high conductivity indicated by the color red and a region of low conductivity indicated by the color blue.

These visual images provide us with real flow patterns in various locations inside the packed column revealing the general nature of flow pattern. These series of tomograms provide significant information on flow phenomena and can play a key part in solving design problems, confirming the design intent and for improving column performance.

Figure 5-19 shows 3D contoured images for data from the measurement for a flow rate of 3 gpm of trickle down-flow, after the injection.

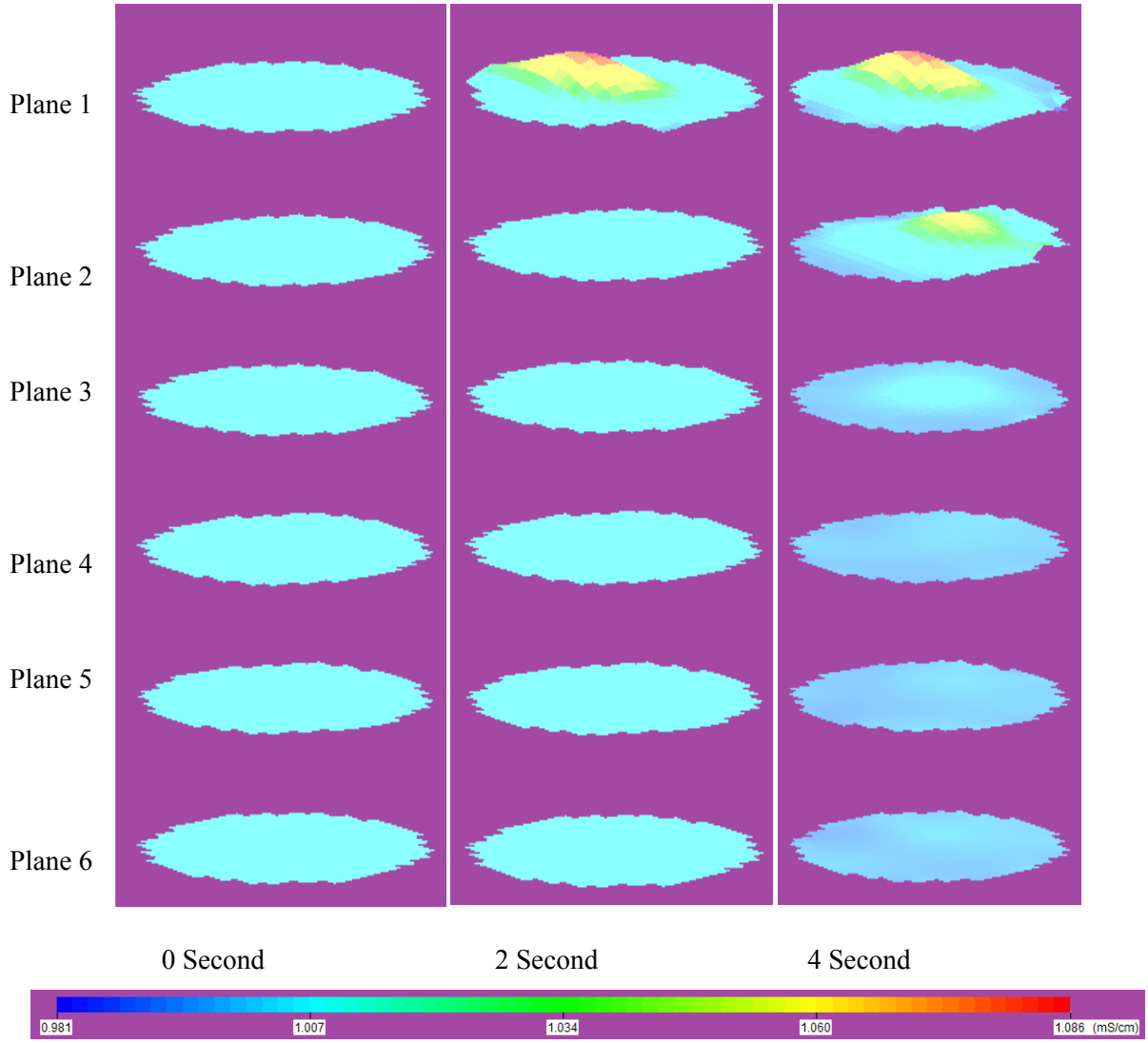

Figure 5-19: Time series of 3D contoured images following injection of high conductivity tracer into the inlet feed for 3 gpm of trickle down-flow.

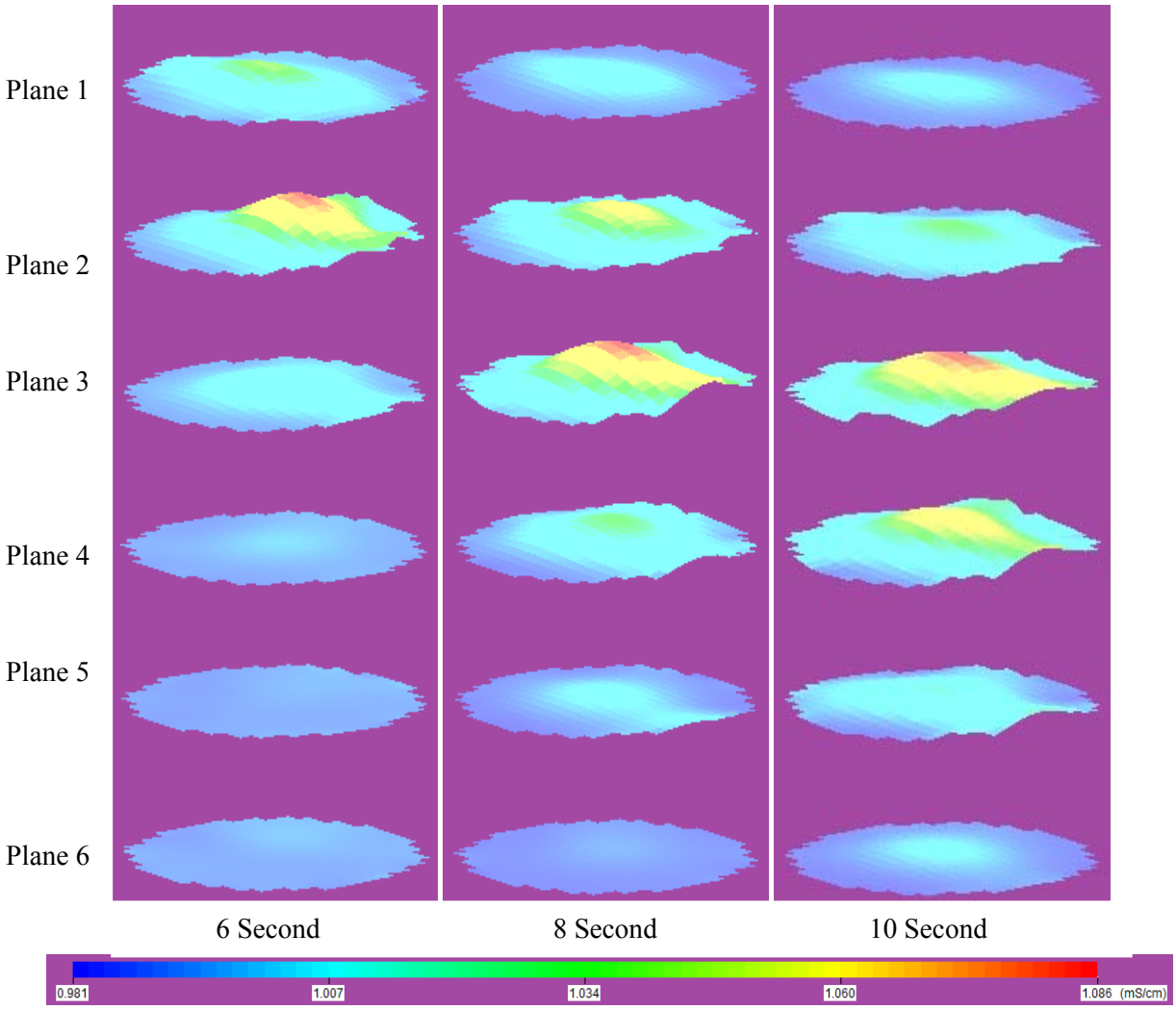

Figure 5-19: Time series of 3D contoured images following injection of high conductivity tracer into the inlet feed for 3 gpm of trickle down-flow (continued).

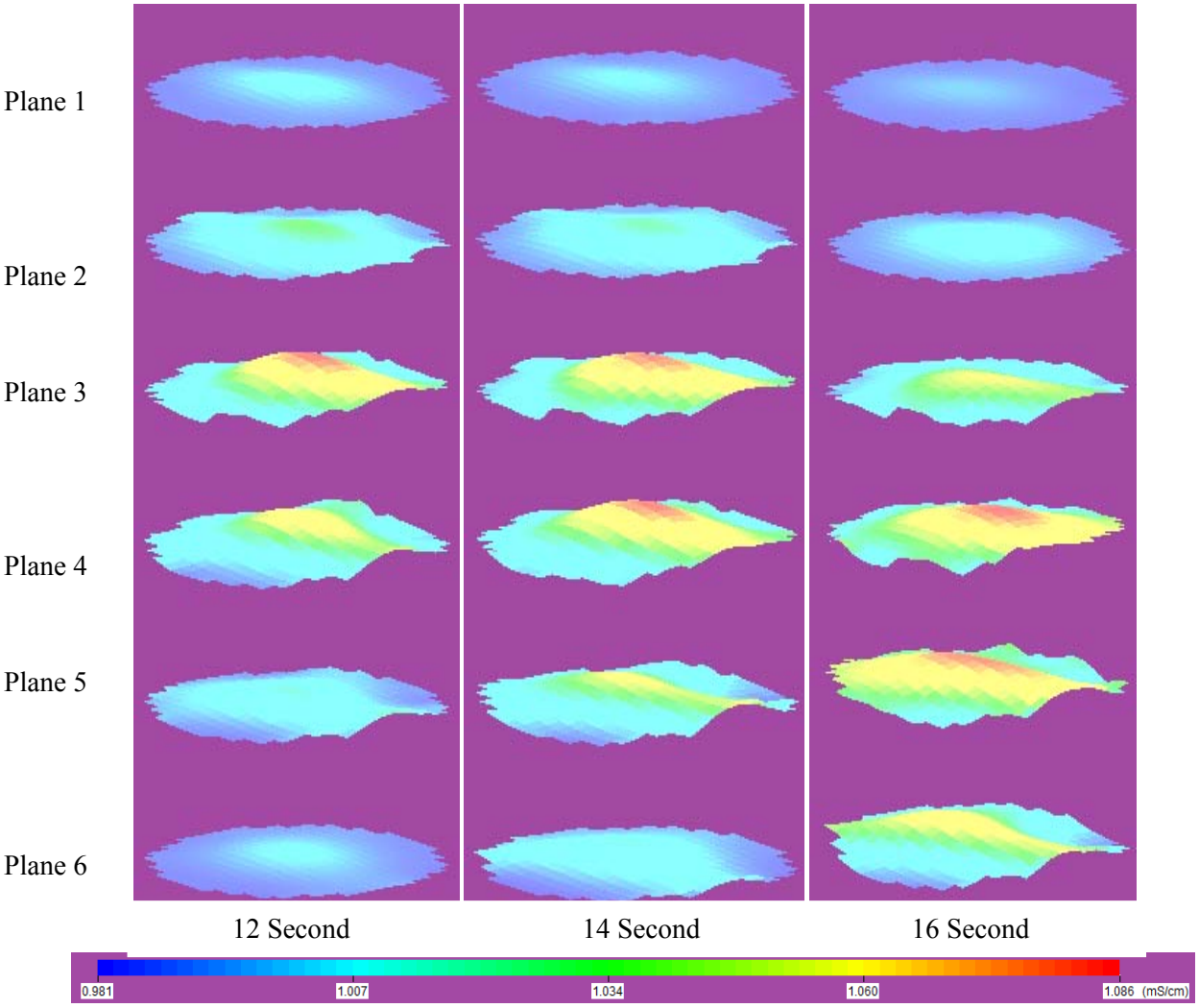

Figure 5-19: Time series of 3D contoured images following injection of high conductivity tracer into the inlet feed for 3 gpm of trickle down-flow (continued).

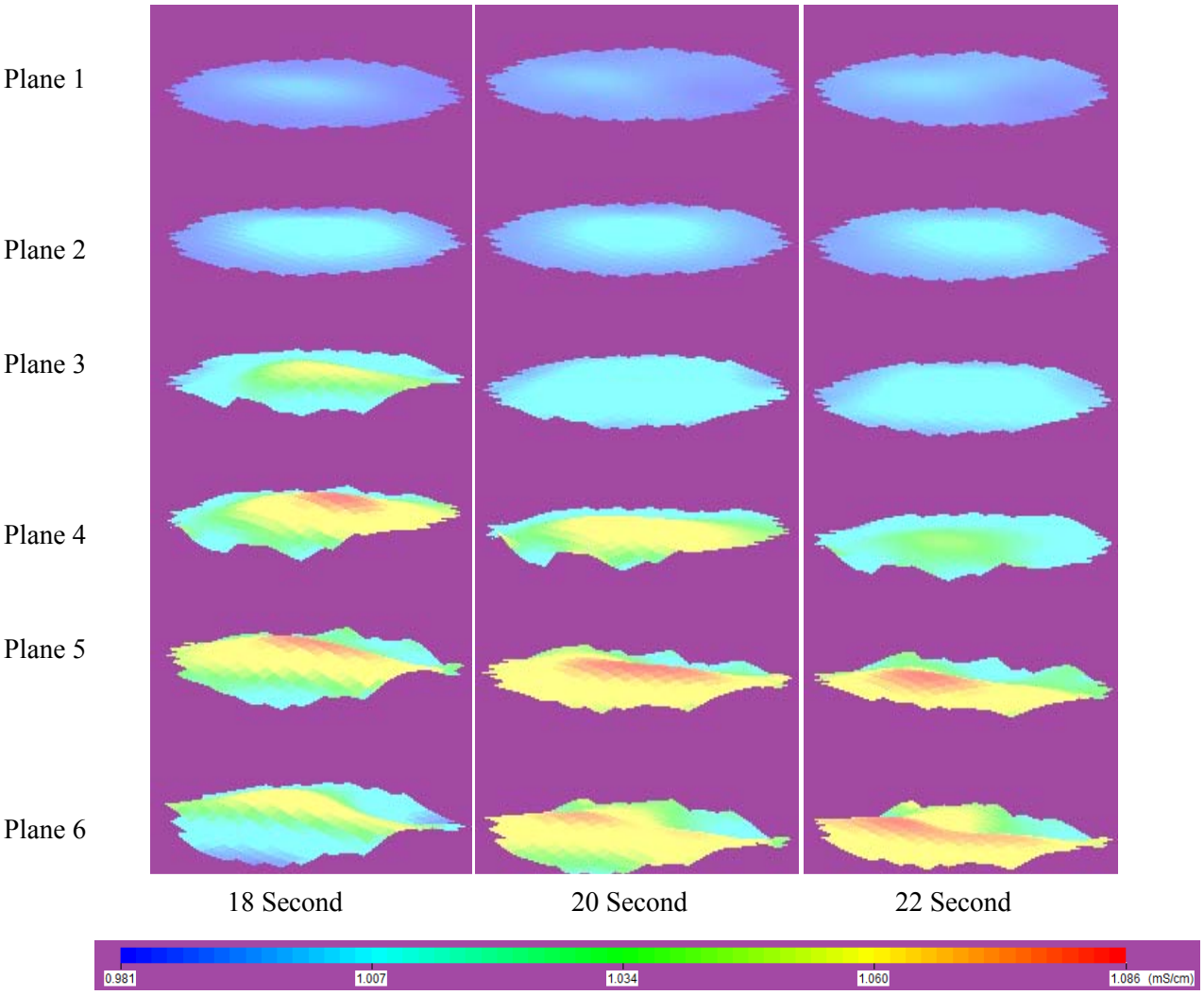

Figure 5-19: Time series of 3D contoured images following injection of high conductivity tracer into the inlet feed for 3 gpm of trickle down-flow (continued).

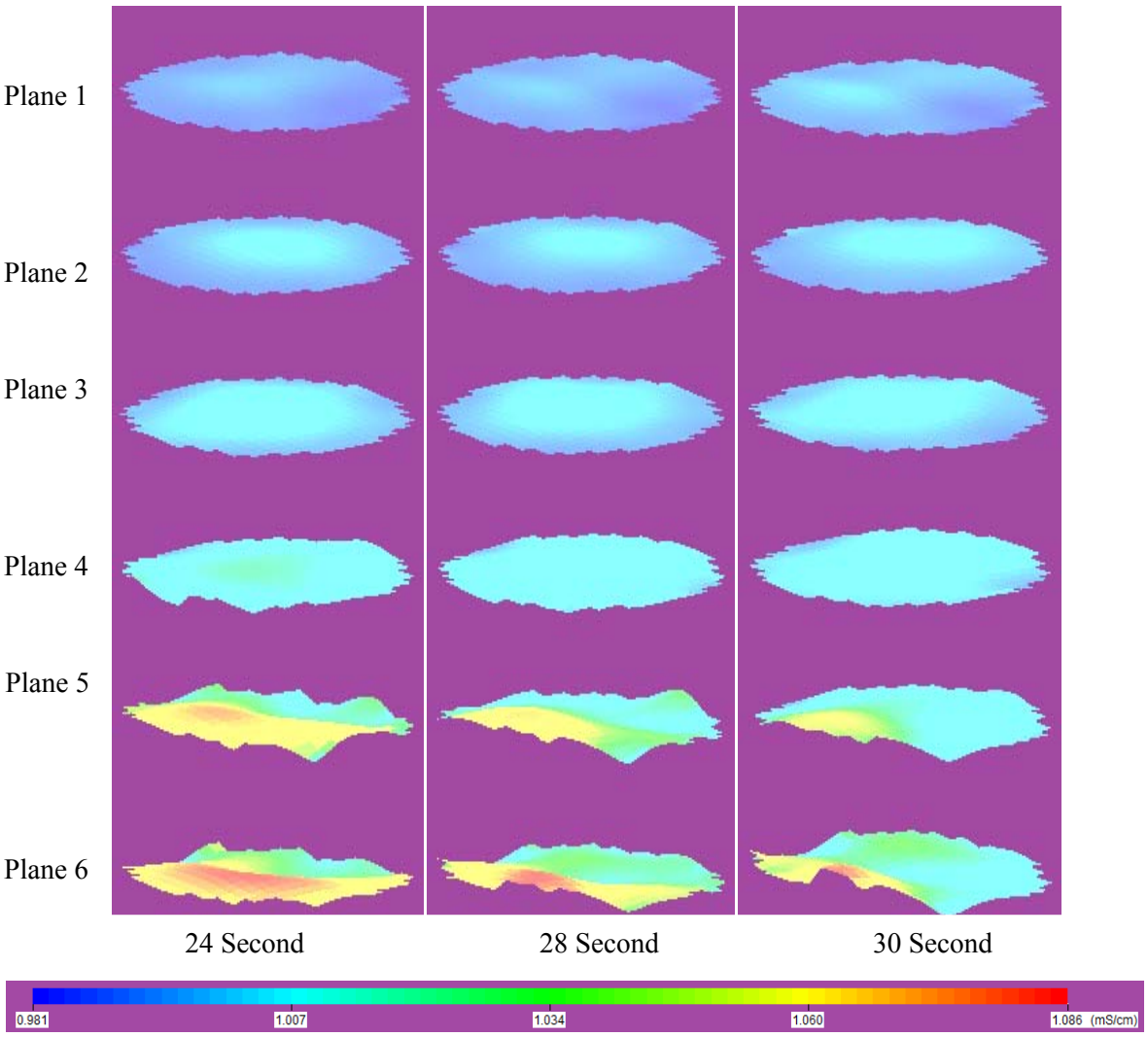

Figure 5-19: Time series of 3D contoured images following injection of high conductivity tracer into the inlet feed for 3 gpm of trickle down-flow (continued).

These successive tomograms show the buildup of the pulse near the center of the column, then moves towards the wall and the pulse is distributed right across the column section. The trailing edge of the pulse detaches from the wall and moves towards the axial exit zone and exit via the central collector is well demonstrated by these data.

The results were similar for each flow rate. The high conductivity tracer was detected initially in the center of plane 1 from where it moved up to planes 2, 3 and so on while simultaneously moving in towards the central collector.

CHAPTER 6

6. Conclusions and Recommendations

6.1 Conclusions

The objective of this study was to measure the factors affect local mass transfer at various axial positions in a random packed column. The study investigated liquid maldistribution, flow rate and flow pattern. Electrical resistance tomography technique (ERT) was employed to measure these factors.

Electrical resistance tomography was applied to visualize the flow pattern and to measure liquid distribution inside a random packed. Sets of tomographic images representing slices through a packed column were obtained for a six measurement planes, each containing 16 electrodes. The obtained tomographic images of conductivity distribution qualitatively demonstrated the flow pattern through the column.

It is believed that this is the first application of ERT to measuring liquid distribution inside packed column based on measuring local liquid velocity using pixel-pixel conductivity of cross-correlation of electrical resistance tomography (ERT), through column cross section at equal intervals planes

Experimental data for liquid flow distribution in a random packed column show that the liquid velocity profile is not uniform, as show all velocity figures as example in the figure 5-3 the value of velocity for group1 fluctuated through the bed height 0.83 (30cm), 1.2 (60cm), 1.11 (90cm), 1.2(120cm) and 1.25(150cm)) .

The good agreement between the experimental data and literature review for liquid flow distribution (proved that the flow distribution far from uniform, Mf have different values through the bed height, (0.61(30cm), 0.51(60cm), 0.45(90cm).

6.2 Recommendations for Future Work

The use of ERT imaging technique continues to have promise of measuring hydraulic parameters to predict the performance of the packed column. ERT can be used for further study in the future as below:

1. To predict the performance of column parameters of interest such as, liquid holdup and pressure drop should be considered because of these two variables affect packing hydraulics.

2. A study on the effects of a range of liquid distribution would be beneficial in investigating more thoroughly how the initial distribution affects the mass transfer. Increasing the number of nozzles would likely improve the liquid distribution.

3. Future work should be undertaken investigate the effect of the ratio of the column diameter to the particle diameter on the fluid dynamics in the column.

4. Further work can be made to evaluate the effect of bed structure (void fraction variation) in the column, since a void variation is one of the most important characteristics of a random packed column that effect the fluid dynamics in the column.

.

Nomenclature

Symbol	Description	
D	Column diameter	(cm)
L	Distance between planes	(cm)
V	Velocity	(cm/s)
Mf	Liquid distribution factor	
V_i	Pixel group velocity	(cm/s)
V_{av}	Average velocity of the pixels	(cm/s)
n	Number of cells	
σ_{est}	Estimated standard deviation	
ERT	Electrical resistance tomography	
LCM	Liquid collector methods	
ECT	Electrical capacitance tomography	
MRI	Magnetic resonance imaging	

References

Aboudheir, A., Tontiwachwuthikul, P., Chakma, A., and Idem, R., "Kinetics of the Reactive Absorption of carbon Dioxide in high CO_2 – loaded, Concentrated Aqueous Monoethanolamine Solutions." Chem. Eng. Sci., 58(2003a): 5195-5210.

Albright, M. A., "Packed Tower Distribution" Hydrocarbon Processing Sept., (1984): 173-177.

Al-Samadi, R., Gordon, C.,Fayed, M., Leva, M. " A Study of Liquid Distribution in an Industrial Scal Packed Tower." A.I.Chem.E. Spring National Meeting, Houston, Texas, U.S.A. April 3, (1989).

Aroonwilas, A., and Tontiwachwuthikul, P., "Mass Transfer Coefficients and Correlation for CO_2 Absorption into 2-Amino-2-methl-1-propanol (AMP) using Structured Packing." Chem. Eng. Sci., 37(2)(1998): 569-575.

Arthur, J., Linnett, J., Raynor, E. and Sington, E. "The Flow of an Air Stream Through a Layer of Granules. Trans. Faraday Soc. 46 (1950): 270-281.

Atta, A., Roy, S., Nigam, K. D. P., "Investigation of Liquid Maldistribution in Trickle-bed Reactors using Porous Media." Chem. Eng. Sci., 62(2007): 7033.

Azzi, M., Turlier, P., Bernard, J. R., Garnero, L., "Mapping Solid Concentration in a Circulating Fluid Bed Using Gammametry." Power Technology, 67 (1991): 27-36.

Babu, B. V., Shah, K. J., Govardhana Rao, V., "Lateral mixing in trickle bed reactor." Chem. Eng. Sci., 62(2007): 7053.

Baker, T., Chilton, T. H. and Vernon, H. C. " The Course of Liquid Flow in Packed Tower." Trans. AIChE., 31 (1935): 296-313

Barber, C. D. and Brown, B. H. " Applied Potential Tomography." J. of Phys. E: Sci. Instrum., 17 (9) (1984): 723-733.

Bemer, G. G. and Zuiderweg, F. J. Radial Liquid Spread and Maldistribution in Packed Columns Under Different Wetting Conditions. Chem. Eng. Sci., 33(1978): 1637-1643.

Bolles, w. L. and Fair, J. R., "Improved Mass-Transfer Model Enhances Packed-Column Design". Chem. Eng. July, (1982): 109-116.

Bolton, G. T. and Primrose, K. M., "An Overview of Electrical Tomography Measurements in Pharmaceutical and related application Areas.", AAPS Pharm.Sci.Tech., 6 (2)(2005), Article 21.

Bowman, J. D. " Use Column Scanning for Predictive Maintenance." Chem. Eng. Prog., 87 (2) (1991): 25-31.

Bowman, J. D. "Troubleshoot Packed Towers with Radioisotopes." Chem. Eng. Prog., 89(9) (1993): 34-41.

Burdett, I. D., Webb, D. R., Davies, G. A. " A New Technique for Studying Dispersion Flow, Hold-up and Axial mixing in Packed Extraction Columns." Chem. Eng. Sci., 36(12) (1981): 1915.

Bukhari, S.F.A. and Yang, W.Q., Tomographic Imaging Technique for Oil Separator Control 3rd International Symposium on Process Tomography. Poland, (2004)..

Charpentier, J.C. "Recent Progress in Two Phase Gas-liquid Mass Transfer in Packed Beds", Chem. Eng. J., 11 (1976): 161-181,

Dickin, F. and Wang,. M. "Electrical Resistance Tomography for Process Applications." Meas. Sci. Technol., 7 (1996): 247-260.

Dutkai, E. and Ruckenstein, E.,"New Experiments Concerning the Distribution of a Liquid in a Packed Column."Chem. Eng. Sei. 25, (1970): 483-488.

Dyakowski, T. " Process Tomography Applied to Multi-Component Measuremrnt." Meas. Sci. Techn., (1996): 343-353

Fukushima, S. and Kusaka, K. "Liquid Phase Volumetric Mass Transfer Coefficient and Boundary of Hydrodynamic Flow Region in Packed Column with Co-current Downward flow," J. Chem. Eng. Japan, 10 (1977): 468-474

Gladden, L. F., and Alexander, P. "Applications of Nuclear Magnetic Resonance Imaging in Process Engineering." Meas. Sci. Technol., 7 (1996): 423-435.

Grieve, B. D., Dyakowski, T., Mann, R., and Wang M. "Interfacing of EIT Into an Industrial Pressure Filter": Proceedings of the 1st World Congress on Industrial Process Tomography; Buxton, UK, April 14-17, (1999).

Grieve, B.D., Smit Q., Mann R., York T.A. "The Application of Electrical Resistance Tomography to a Large Volume Production Pressure Filter." Proceedings of the 2nd World Congress on Industrial Process Tomography; August 29-31, 2001; Hannover, Germany.

Hoek, P.J., Wesselingh, J. A., and Zuiderweg, F. J. " Small Scale and Large Scale Liquid Maldistribution in Packed Columns." Chem. Eng. Des., 64 (1986): 431-449

Holden, P. J., Wang, M., Mann, R., Dickin, F. J.,and Edwards R. B. " Imaging Stirred Vessel Macro-mixing Using Electrical Resistance Tomography." AIChE J., 44 (1998): 780-790

Huber, M. and Hiltbrunne, R., " Liquid Maldistribution in Packed Columns.". Chem. Eng. Sci., 21 (1966): 819-832.

Huang, S. M., Xie, C. G., Plaskowski A., Thorn R., Williams R. A., Hunt A., and Beck M. S. " Process Tomography for Identification, Design and Measurement in Industrial System" Power Technol., 69 (1992): 85-92

Kak, A. C. and M. Slaney "Principles of Computerized Tomographic Imaging." IEEE Press, Inc., New York, 1991.

Kister, H. Z. "Distillation Design" McGraw-Hill, New York, (1992).

Kouri, R. J. and Sohlo, J., "Liquid and Gas Flow Patterns in Random and Structured Packings.I." Chem. E. Symp. Ser . No. 104,B193-B211(1987).

Kouri, R. J. and Sohlo, J., "Liquid and Gas Flow Patterns in Random Packings." Chem. Eng.J., 61 (1996): 95-105.

Kunjummen,B., Prasad, T., and Sai, P., "Radial Liquid Distribution in Gas-Liquid Concurrent Downflow Through Packed Beds." Bioprocess Engineering, 22 (2000): 471-475.

Marcandelli, C., Lamine, A. S., Bernard, R., and Wild, G., "Liquid Distribution in Trickle Bed Reactor." Oil & Gas Science and Technology - Rev. IFP, 55(2000): 407.

Mak, S., Koning, C., Hamersma, J., and Fortun, H., "Axial Dispersion in Single-Phase Flow in a Pulsed Packed column containing Structured Packing" Chem. Eng. Sci., 46(3) (1991): 819.

Mann, R., Dickin, F.J., Wang, M., Dyakowski, T., Williams, R. A., Edwards, R. B., Forrest, A. E., and Holden, P. J. "Application of Electrical Resistance Tomography to Interrogate Mixing Processes at Plant Scale." Chem. Eng. Sci., 52(1997):2087-2097.

Manning, R. E. and Cannon, M. R., " Distillation Improvement by Control of Phase Channelling in Packed Columns." Ind. Eng. Chem., 49 (1957): 347-349.

McGreavy, C., E. A. Foumeny, and K. H. Javed; "Characterization of Transport Properties for Fixed Bed in terms of local Bed Structure and Flow Distribution." Chem. Eng. Sci., Vol. 41, (1986): 787-797.

McManus R.K., Funk G.A., Harold M.P. and Ng K.M., "Experimental study of reaction in trickle bed reactors with liquid maldistribution." Ind. Eng. Chem. Res., 32 (1993): 570.

Morales, M., Spinn, C. W. and Smith, J. M. "Velocities and Effective Thermal Conductivities in Packed Beds." Ind. Eng. Chem. 43(1951): 225-232.

Mullin, J. W., " The Effect of Mal-distribution on the Performance of packed Columns." Ind. Chem., 33 (1957): 408-417.

Newell, R. and Standish, N. Velocity Distribution in Rectangular Packed Beds and Non-ferrous Blast Furnaces. Met. Trans. 4B(1973) : 1851-1857.

Nutter, D.E., Silvey, F. C. and Stober B. K., "Random Packing performance in Light Ends Distillation." Chem. E. Symp. Ser .No. 128 (1992): A99-A107

Onda, K., Takeuchi, H., Maeda, Y. and Takeuchi, N., "Liquid Distribution in a Packed Column." Chem. Eng. Sei.,28 (1973): 1677-1683.

Olujic, Z. and de Graauw J., "Appearance of Maldistribution in Distillation Columns Equipped with High Performance Packings." Chem. Biochem. Eng., 4 (1989): 181-196.

Porter, K. E. and Templeman, J. J., "Liquid Flow in Packed Column. Part III: Wall flow." Trans. Inst. Chem. Engrs., 46(1968): T86-T94.

Rao, V.G. and Drinkenburg, A. A. H. "Solid-Liquid Mass Transfer in Packed Beds with Co-Current Gas-Liquid Down-flow." AIChE J., 31(1985): 1059-1068

Ravindra, P.V., Rao, D.P. and Rao, M.S. “Liquid Flow Texture in Trickle-Bed: An Experimental Study” Ind. Eng. Chem. Res., 36 (1997): 5133-5145

Reinecke, N., Mewes, D. “ Tomographic Imaging of Trickle-Bed Reactors.” Chem. Eng. Sci., 51 (1996): 2131-2138.

Reinecke, N., and Mewes, D. “Investigation of the Two-Phase Flow in Trickle-Bed Reactors Using Capacitance Tomography.” Chem. Eng. Sci., 52 (1997): 2111-2127.

Ricard, F., Brechtelsbauer, C., Xu, X. Y., and Lawrence, C. J. “Monitoring of Multiphase Pharmaceutical Processes Using Electrical Resistance Tomography.” Trans IChem E., 83 (part-A7) (2005): 794-805.

Scott, A. H. “ Liquid Distribution in Packed Tower.” Trans. Inst. Chem. Engrs., 13 (1935): 211-217

Schwartz, C. E. and Smith, J. M. “Flow distributionn in packed beds.” Ind. Eng. Chem. 45(1953): 1205-1218.

Schertz, W. W. and Bischoff, K. B. “Thermal and Material Transport in Non-isothermal Packed Beds.” AIChE J., 15(1969): 597-604.

Sederman, A. J., Johns, M. L., Bramley, A. S., Alexander, P., Gladden, L. F. “ Magnetic Resonance Imageing of Liquid Flow and Pore Structure within Packed Beds. Chem. Eng. Sci., 52 (1997): 2239-2250

Severance, W. A. N. “Advances in Radiation Scanning of Distillation columns.” Chem. Eng. Prog., 77 (9) (1981): 38-41.

Sie, S.T., Calis, H.P., “Parallel-passage and Lateral Flow Reactors. In: Cybulski, A., Moulijn, J.A. (Eds.), Structured Catalysts and Reactors. Marcel Dekker Inc”, New York, p. 339 (1996) (Chapter 12).

Song, M., F. H. Yin, K. T. Chung, and K. Nandakumer, “A Stochastic Model for the Simulation of the Natural Flow in Radom Packed Columns”, Canadian Journal of Chemical Engineering, Vol. 76, (1998): 183-189

Smith, G. B., Gamblin, B. R., and Newton, D. “ X-ray Imaging of Slurry Bubble Column Reactors: the Effects of System Pressure and Scale. Trans.” IchemE. , 73 (1995): 632-636.

Stanley SJ, Mann R, Primrose KM. Interrogation of a Precipitation reaction by Electrical Resistance Tomography. AIChE J., 51 (2005): 607-614.

Stichlmair, J. and Stemmer, A., “Influence of Maldistribution on Mass Transfer in Packed Columns.” I. Chem. E. Symp. Ser. No. 104., (1987): B213-B224

Subaygo, N. Standish, and G.A. Brooks. “A new Model of Velocity Distribution of Single Fluid Flowing in packed beds”. Chem. Eng. Sci., Vol. 53, (1988): 1375-1385

Sun, C. G., Yin, F. H., Afacan, A., Nandakumar, K. and Chuang, K. T., “Modeling and Simulation of Flow Maldistribution in Random Packed Columns with Gas-Liquid Countercurrent Flow,” Trans. IChem E., 78 (2000): 378-388

Tapp, H. S. and Williams, R. A.,” Status and Applications of Micro-electrical Resistance Tomography.” Chem. Eng. Sci., 77 (2000): 119-125.

Treybal, R. E., Mass-Transfer Operations, McGraw-Hill (1987).

Vlaev D., Wang M., Dyakowski T., Mann R., and Grieve, D., "Detecting Filter Cake Pathologies in Solid-Liquid Filtration: Semi-Tech Scale Demonstration Using Electrical Resistance Tomography." Chem. Eng J., 77 (2000): 87-92.

Wang, M. "Measurement Science and Technology," (Vol. 13) (2002): 101-117.

Wang, M., Jia, X., and Williams, R.A., "Electrical Tomographic Imaging for Bubble Column Measurement and Control." In: McCann H, Scott DM, eds. Proceedings of SPIE,; Bellingham, WA: SPIE; Volume: 4188 (2001): 114-121.

Williams, R.A. and Beck, M.S. "Process tomography: Principles, Techniques and Applications." Butterworth-Heinemann, Oxford, (1995).

Williams, R.A., Jia, X., West, R. M., and Roberts K. J. "On Line Measurement of Solids Distribution in Stirred Tanks and Crystallizers using Electrical Computed Tomography." International Conference on Mixing and Crystallisation.; Tioman Island, Malaysia, April 22-25, (1998) .

Yin, F., Afacan, A., Nanadakumar, K., and Chuang, K. "Liquid Holdup Distribution in Packed Columns: Gama Ray Tomography and CFD Simulation". Chem. Eng and Proce., Vol. 42, (2002): 473-483.

Ziolkowska, I. and Ziolkowski, " Modeling of Gas Interstitial Velocity Radial Distribution over a Cross section of a Tube Packed with a Granular Catalyst Bed". Chem. Eng. Sci., No. 48, (1993): 3283-3292

Zuiderweg, F. J., Kunesh, J. G., and King, D. W. " A Model for the Calculation of the Effect of Mal-distribution on the Efficiency of a Packed Column." Trans. IChemE., 71 (1993): 38-44.

APPENDICES

APPENDIX A

Experimental Results for

Full Liquid Up-flow and Trickle Down-Flow

Experimental results of velocity profile for trickle down-flow of 3, and 6 gpm for 10 groups are shown in the Tables below.

Table A1: Axial velocity of group 1 for full liquid up-flow at 3 gpm

Plane no.	Time, s	Max Conductivity, mS/cm
1	36	1.16969
2	72	1.10342
3	97	1.11454
4	124	1.09478
5	149	1.08854
6	173	1.08087

Plane no	Time, s	Bed Height, cm	Velocity cm/s
P1-P2	36	30	0.83
P2-P3	25	60	1.2
P3-P4	27	90	1.11
P4-P5	25	120	1.2
P5-P6	24	150	1.25

Table A2: Axial velocity of group 2 for full liquid up-flow at 3 gpm

Plane no.	Time, s	Max Conductivity mS/cm
1	36	1.17076
2	72	1.10294
3	97	1.11161
4	124	1.09447
5	149	1.08854
6	173	1.08

Plane no	Time, s	Bed Height cm	Velocity cm/s
P1-P2	36	30	0.83
P2-P3	25	60	1.2
P3-P4	27	90	1.11
P4-P5	25	120	1.2
P5-P6	24	150	1.25

Table A3: Axial velocity of group 3 for full liquid up-flow at 3 gpm

Plane no.	Time, s	Max Conductivity, mS/cm
1	37	1.16043
2	72	1.10276
3	97	1.10863
4	124	1.09413
5	149	1.08879
6	175	1.07913

Plane no	Time, s	Bed Height cm	Velocity cm/s
P1-P2	35	30	0.85
P2-P3	25	60	1.2
P3-P4	27	90	1.11
P4-P5	25	120	1.2
P5-P6	26	150	1.15

Table A4: Axial velocity of group 4 for full liquid up-flow at 3 gpm

Plane no.	Time, s	Max Conductivity, mS/cm
1	38	1.14326
2	72	1.10164
3	97	1.10483
4	119	1.09282
5	149	1.08828
6	175	1.07749

Plane no	Time, s	Bed Height, cm	Velocity, cm/s
P1-P2	34	30	0.88
P2-P3	25	60	1.2
P3-P4	22	90	1.36
P4-P5	30	120	1
P5-P6	26	150	1.15

Table A5: Axial velocity of group 5 for full liquid up-flow at 3 gpm

Plane no.	Time, s	Max Conductivity, mS/cm
1	51	1.12384
2	72	1.09851
3	96	1.0995
4	119	1.08993
5	149	1.08616
6	175	1.07438

Plane no	Time, s	Bed Height, cm	Velocity, cm/s
P1-P2	21	30	1.42
P2-P3	24	60	1.25
P3-P4	23	90	1.30
P4-P5	30	120	1
P5-P6	26	150	1.15

Table A6: Axial velocity of group 6 for full liquid up-flow at 3 gpm

Plane no.	Time, s	Max Conductivity, mS/cm
1	51	1.11345
2	73	1.093
3	96	1.09263
4	119	1.08492
5	144	1.08231
6	171	1.06972

Plane no	Time, s	Bed Height, cm	Velocity, cm/s
P1-P2	22	30	1.36
P2-P3	23	60	1.30
P3-P4	23	90	1.30
P4-P5	25	120	1.2
P5-P6	27	150	1.11

Table A7: Axial velocity of group 7 for full liquid up-flow at 3 gpm

Plane no.	Time, s	Max Conductivity, mS/cm
1	46	1.10232
2	73	1.08574
3	96	1.08449
4	122	1.07839
5	144	1.07696
6	171	1.06404

Plane no	Time, s	Bed Height, cm	Velocity, cm/s
P1-P2	27	30	1.11
P2-P3	23	60	1.30
P3-P4	26	90	1.15
P4-P5	22	120	1.36
P5-P6	27	150	1.11

Table A8: Axial velocity of group 8 for full liquid up-flow at 3 gpm

Plane no.	Time, s	Max Conductivity, mS/cm
1	46	1.09257
2	73	1.07763
3	96	1.0761
4	122	1.07145
5	144	1.07092
6	168	1.05811

Plane no	Time, s	Bed Height, cm	Velocity, cm/s
P1-P2	27	30	1.11
P2-P3	23	60	1.30
P3-P4	26	90	1.15
P4-P5	22	120	1.36
P5-P6	24	150	1.25

Table A9: Axial velocity of group 9 for full liquid up-flow at 3 gpm

Plane no.	Time, s	Max Conductivity, mS/cm
1	46	1.08405
2	71	1.07024
3	96	1.06877
4	122	1.06523
5	144	1.06536
6	168	1.05306

Plane no	Time, s	Bed Height, cm	Velocity, cm/s
P1-P2	25	30	1.2
P2-P3	25	60	1.2
P3-P4	26	90	1.15
P4-P5	22	120	1.36
P5-P6	24	150	1.25

Table A10: Axial velocity of group 10 for full liquid up-flow at 3 gpm

Plane no.	Time, s	Max Conductivity, mS/cm
1	46	1.07831
2	73	1.06491
3	96	1.06381
4	122	1.06099
5	148	1.0616
6	168	1.04986

Plane no	Time, s	Bed Height, cm	Velocity, cm/s
P1-P2	27	30	1.11
P2-P3	23	60	1.30
P3-P4	26	90	1.15
P4-P5	26	120	1.15
P5-P6	20	150	1.5

Table B1: Axial velocity of group 1 for full liquid up-flow at 6 gpm

Plane no.	Time, s	Max Conductivity, mS/cm
1	31	1.36987
2	51	1.12793
3	65	1.14008
4	81	1.11756
5	96	1.1107
6	109	1.10887

Plane no	Time, s	Bed Height, cm	Velocity, cm/s
P1-P2	20	30	1.5
P2-P3	14	60	2.14
P3-P4	16	90	1.87
P4-P5	15	120	2
P5-P6	13	150	2.30

Table B2: Axial velocity of group 2 for full liquid up-flow at 6 gpm

Plane no.	Time, s	Max Conductivity, mS/cm
1	31	1.40107
2	47	1.13283
3	65	1.13991
4	78	1.12
5	93	1.11272
6	107	1.10963

Plane no	Time, s	Bed Height, cm	Velocity, cm/s
P1-P2	16	30	1.87
P2-P3	18	60	1.66
P3-P4	13	90	2.30
P4-P5	15	120	2
P5-P6	14	150	2.14

Table B3: Axial velocity of group 3 for full liquid up-flow at 6 gpm

Plane no.	Time, s	Max Conductivity, mS/cm
1	31	1.39464
2	47	1.13839
3	65	1.13906
4	78	1.1223
5	92	1.11586
6	107	1.11033

Plane no	Time, s	Bed Height, cm	Velocity, cm/s
P1-P2	16	30	1.87
P2-P3	18	60	1.66
P3-P4	13	90	2.30
P4-P5	14	120	2.14
P5-P6	15	150	2

Table B4: Axial velocity of group 4 for full liquid up-flow at 6 gpm

Plane no.	Time, s	Max Conductivity, mS/cm
1	31	1.35696
2	47	1.14064
3	62	1.13687
4	78	1.12265
5	92	1.11768
6	107	1.10945

Plane no	Time, s	Bed Height, cm	Velocity, cm/s
P1-P2	16	30	1.87
P2-P3	15	60	2
P3-P4	16	90	1.87
P4-P5	14	120	2.14
P5-P6	15	150	2

Table B5: Axial velocity of group 5 for full liquid up-flow at 6 gpm

Plane no.	Time, s	Max Conductivity, mS/cm
1	31	1.3036
2	47	1.13841
3	61	1.13245
4	78	1.11986
5	92	1.11659
6	105	1.10629

Plane no	Time, s	Bed Height, cm	Velocity, cm/s
P1-P2	16	30	1.87
P2-P3	14	60	2.14
P3-P4	17	90	1.76
P4-P5	14	120	2.14
P5-P6	13	150	2.30

Table B6: Axial velocity of group 6 for full liquid up-flow at 6 gpm

Plane no.	Time, s	Max Conductivity, mS/cm
1	31	1.24949
2	47	1.13171
3	61	1.12466
4	78	1.11373
5	92	1.1121
6	105	1.10056

Plane no	Time, s	Bed Height, cm	Velocity, cm/s
P1-P2	16	30	1.87
P2-P3	14	60	2.14
P3-P4	17	90	1.76
P4-P5	14	120	2.14
P5-P6	13	150	2.30

Table B7: Axial velocity of group 7 for full liquid up-flow at 6 gpm

Plane no.	Time, s	Max Conductivity, mS/cm
1	31	1.20345
2	47	1.1218
3	61	1.11445
4	74	1.10537
5	90	1.10491
6	105	1.0928

Plane no	Time, s	Bed Height, cm	Velocity, cm/s
P1-P2	16	30	1.87
P2-P3	14	60	2.14
P3-P4	13	90	2.30
P4-P5	16	120	1.87
P5-P6	15	150	2

Table B8: Axial velocity of group 8 for full liquid up-flow at 6 gpm

Plane no.	Time, s	Max Conductivity, mS/cm
1	31	1.16824
2	47	1.11067
3	61	1.10348
4	74	1.09634
5	90	1.09633
6	104	1.0845

Plane no	Time, s	Bed Height, cm	Velocity, cm/s
P1-P2	16	30	1.87
P2-P3	14	60	2.14
P3-P4	13	90	2.30
P4-P5	16	120	1.87
P5-P6	14	150	2.14

Table B9: Axial velocity of group 9 for full liquid up-flow at 6 gpm

Plane no.	Time, s	Max Conductivity, mS/cm
1	32	1.14462
2	47	1.10043
3	61	1.09352
4	74	1.08817
5	90	1.08814
6	101	1.07705

Plane no	Time, s	Bed Height, cm	Velocity, cm/s
P1-P2	15	30	2
P2-P3	14	60	2.14
P3-P4	13	90	2.30
P4-P5	16	120	1.87
P5-P6	11	150	2.72

Table B10: Axial velocity of group 10 for full liquid up-flow at 6 gpm

Plane no.	Time, s	Max Conductivity, mS/cm
1	32	1.12837
2	47	1.09275
3	61	1.08598
4	74	1.08271
5	93	1.08239
6	101	1.07201

Plane no	Time, S	Bed Height, cm	Velocity, cm/s
P1-P2	15	30	2
P2-P3	14	60	2.14
P3-P4	13	90	2.30
P4-P5	19	120	1.57
P5-P6	8	150	3.75

Table C1: Axial velocity of group 1 for full liquid up-flow at 9 gpm

Plane no.	Time, s	Max Conductivity, mS/cm
1	29	1.25227
2	42	1.09129
3	53	1.09763
4	64	1.08058
5	73	1.07289
6	84	1.06862

Plane no	Time, s	Bed Height, cm	Velocity, cm/s
P1-P2	13	30	2.30
P2-P3	11	60	2.72
P3-P4	11	90	2.72
P4-P5	9	120	3.33
P5-P6	11	150	2.72

Table C2: Axial velocity of group 2 for full liquid up-flow at 9 gpm

Plane no.	Time, s	Max Conductivity, mS/cm
1	29	1.24554
2	41	1.09385
3	52	1.09511
4	62	1.08201
5	73	1.07565
6	83	1.06906

Plane no	Time, s	Bed Height, cm	Velocity, cm/s
P1-P2	12	30	2.5
P2-P3	11	60	2.72
P3-P4	10	90	3
P4-P5	11	120	2.72
P5-P6	10	150	3

Table C3: Axial velocity of group 3 for full liquid up-flow at 9 gpm

Plane no.	Time, s	Max Conductivity, mS/cm
1	29	1.24554
2	41	1.09385
3	52	1.09511
4	62	1.08201
5	73	1.07565
6	83	1.06906

Plane no	Time, s	Bed Height, cm	Velocity, cm/S
P1-P2	12	30	2.5
P2-P3	11	60	2.72
P3-P4	10	90	3
P4-P5	11	120	2.72
P5-P6	10	150	3

Table C4: Axial velocity of group 4 for full liquid up-flow at 9 gpm

Plane no.	Time, s	Max Conductivity, mS/cm
1	29	1.21319
2	40	1.09374
3	51	1.09251
4	62	1.0815
5	73	1.07612
6	82	1.06875

Plane no	Time, s	Bed Height, cm	Velocity, cm/s
P1-P2	11	30	2.72
P2-P3	11	60	2.72
P3-P4	11	90	2.72
P4-P5	11	120	2.72
P5-P6	9	150	3.33

Table C5: Axial velocity of group 5 for full liquid up-flow at 9 gpm

Plane no.	Time, s	Max Conductivity, mS/cm
1	29	1.1734
2	40	1.09103
3	51	1.08813
4	62	1.07908
5	72	1.07493
6	82	1.06694

Plane no	Time, s	Bed Height, cm	Velocity, cm/s
P1-P2	11	30	2.72
P2-P3	11	60	2.72
P3-P4	11	90	2.72
P4-P5	10	120	3
P5-P6	10	150	3

Table C6: Axial velocity of group 6 for full liquid up-flow at 9 gpm

Plane no.	Time, s	Max Conductivity, mS/cm
1	30	1.14258
2	40	1.08563
3	51	1.08184
4	61	1.07489
5	72	1.07182
6	82	1.06343

Plane no	Time, s	Bed Height, cm	Velocity, cm/s
P1-P2	10	30	3
P2-P3	11	60	2.72
P3-P4	10	90	3
P4-P5	11	120	2.72
P5-P6	10	150	3

Table C7: Axial velocity of group 7 for full liquid up-flow at 9 gpm

Plane no.	Time, s	Max Conductivity, mS/cm
1	31	1.11864
2	40	1.07829
3	51	1.07425
4	61	1.06926
5	71	1.06738
6	82	1.05868

Plane no	Time, s	Height, cm	Velocity, cm/s
P1-P2	9	30	3.33
P2-P3	11	60	2.72
P3-P4	10	90	3
P4-P5	10	120	3
P5-P6	11	150	2.72

Table C8: Axial velocity of group 8 for full liquid up-flow at 9 gpm

Plane no.	Time, s	Max Conductivity, mS/cm
1	31	1.10323
2	40	1.07031
3	51	1.06641
4	61	1.06313
5	71	1.06227
6	82	1.05353

Plane no	Time, s	Bed Height, cm	Velocity, cm/s
P1-P2	9	30	3.33
P2-P3	11	60	2.72
P3-P4	10	90	3
P4-P5	10	120	3
P5-P6	11	150	2.72

Table C9: Axial velocity of group 9 for full liquid up-flow at 9 gpm

Plane no.	Time, s	Max Conductivity, mS/cm
1	31	1.09088
2	40	1.06304
3	52	1.05964
4	61	1.05762
5	71	1.05753
6	82	1.04892

Plane no	Time, s	Bed Height, cm	Velocity, cm/s
P1-P2	9	30	3.33
P2-P3	12	60	2.5
P3-P4	9	90	3.33
P4-P5	10	120	3
P5-P6	11	150	2.72

Table C10: Axial velocity of group 10 for full liquid up-flow at 9 gpm

Plane no.	Time, s	Max Conductivity, mS/cm
1	31	1.08226
2	41	1.05777
3	52	1.05499
4	61	1.05382
5	71	1.05415
6	82	1.04569

Plane no	Time, s	Bed Height, cm	Velocity, cm/s
P1-P2	10	30	3
P2-P3	11	60	2.72
P3-P4	9	90	3.33
P4-P5	10	120	3
P5-P6	11	150	2.72

Experimental results of velocity profile for trickle down-flow of 3 and 6 gpm for 10 groups are shown in the tables below.

Table D1: Axial velocity of group 1 for trickle up-flow at 3 gpm

Plane no.	Time, s	Max Conductivity, mS/cm
1	33	1.14874
2	35	1.20783
3	36	1.23319
4	38	1.20667
5	40	1.18469
6	41	1.15432

Plane no	Time, s	Bed Height, cm	Velocity, cm/s
P1-P2	2	30	15
P2-P3	1	60	30
P3-P4	2	90	15
P4-P5	2	120	15
P5-P6	1	150	30

Table D2: Axial velocity of group 2 for trickle up-flow at 3 gpm

Plane no.	Time, s	Max Conductivity, mS/cm
1	33	1.12225
2	35	1.20608
3	36	1.22811
4	38	1.20328
5	40	1.1691
6	41	1.13824

Plane no	Time, s	Bed Height, cm	Velocity, cm/S
P1-P2	2	30	15
P2-P3	1	60	30
P3-P4	2	90	15
P4-P5	2	120	15
P5-P6	1	150	30

Table D3: Axial velocity of group 3 for trickle up-flow at 3 gpm

Plane no.	Time, s	Max Conductivity, mS/cm
1	33	1.08965
2	34	1.19829
3	36	1.20985
4	38	1.1896
5	40	1.14865
6	41	1.119

Plane no	Time, s	Bed Height, cm	Velocity, cm/s
P1-P2	1	30	30
P2-P3	2	60	15
P3-P4	2	90	15
P4-P5	2	120	15
P5-P6	1	150	30

Table D4: Axial velocity of group 4 for trickle up-flow at 3 gpm

Plane no.	Time, s	Max Conductivity, mS/cm
1	33	1.05916
2	34	1.185
3	36	1.18271
4	38	1.16879
5	40	1.12692
6	41	1.09936

Plane no	Time, s	Bed Height, cm	Velocity, cm/s
P1-P2	1	30	30
P2-P3	2	60	15
P3-P4	2	90	15
P4-P5	2	120	15
P5-P6	1	150	30

Table D5: Axial velocity of group 5 for trickle up-flow at 3 gpm

Plane no.	Time, s	Max Conductivity, mS/cm
1	33	1.03622
2	34	1.16512
3	36	1.15189
4	38	1.14465
5	40	1.10703
6	41	1.08146

Plane no	Time, s	Bed Height, cm	Velocity, cm/s
P1-P2	1	30	30
P2-P3	2	60	15
P3-P4	2	90	15
P4-P5	2	120	15
P5-P6	1	150	30

Table D6: Axial velocity of group 6 for trickle up-flow at 3 gpm

Plane no.	Time, s	Max Conductivity, mS/cm
1	32	1.0216
2	34	1.14211
3	36	1.12185
4	39	1.12464
5	40	1.09111
6	42	1.06956

Plane no	Time, S	Bed Height, cm	Velocity, cm/s
P1-P2	2	30	15
P2-P3	2	60	15
P3-P4	3	90	10
P4-P5	1	120	30
P5-P6	2	150	15

Table D7: Axial velocity of group 7 for trickle up-flow at 3 gpm

Plane no.	Time, s	Max Conductivity, mS/cm
1	34	1.0117
2	35	1.11842
3	36	1.09548
4	39	1.10798
5	40	1.08019
6	42	1.06245

Plane no	Time, S	Bed Height, cm	Velocity, cm/s
P1-P2	1	30	30
P2-P3	1	60	30
P3-P4	3	90	10
P4-P5	1	120	30
P5-P6	2	150	15

Table D8: Axial velocity of group 8 for trickle up-flow at 3 gpm

Plane no.	Time, s	Max Conductivity, mS/cm
1	34	1.00558
2	35	1.09563
3	36	1.07403
4	39	1.09465
5	40	1.07439
6	42	1.0583

Plane no	Time, s	Bed Height, cm	Velocity, cm/s
P1-P2	1	30	30
P2-P3	1	60	30
P3-P4	3	90	10
P4-P5	1	120	30
P5-P6	2	150	15

Table D9: Axial velocity of group 9 for trickle up-flow at 3 gpm

Plane no.	Time, s	Max Conductivity, mS/cm
1	32	1.00262
2	34	1.07455
3	38	1.06101
4	39	1.08521
5	40	1.07328
6	42	1.05701

Plane no	Time, s	Bed Height, cm	Velocity, cm/s
P1-P2	2	30	15
P2-P3	4	60	7.5
P3-P4	1	90	30
P4-P5	1	120	30
P5-P6	2	150	15

Table D10: Axial velocity of group 10 for trickle up-flow at 3 gpm

Plane no.	Time, s	Max Conductivity, mS/cm
1	33	1.00247
2	34	1.05354
3	38	1.05571
4	39	1.08035
5	40	1.07736
6	42	1.05899

Plane no	Time, s	Bed Height, cm	Velocity, cm/s
P1-P2	1	30	30
P2-P3	4	60	7.5
P3-P4	1	90	30
P4-P5	1	120	30
P5-P6	2	150	15

Table E1: Axial velocity of group 1 for trickle up-flow at 6 gpm

Plane no.	Time, s	Max Conductivity, mS/cm
1	28	1.20487
2	29	1.20976
3	30	1.33968
4	31	1.36539
5	32	1.31417
6	33	1.22379

Plane no	Time, s	Bed Height, cm	Velocity, cm/s
P1-P2	1	30	30
P2-P3	1	60	30
P3-P4	1	90	30
P4-P5	1	120	30
P5-P6	1	150	30

Table E2: Axial velocity of group 2 for trickle up-flow at 6 gpm

Plane no.	Time, s	Max Conductivity, mS/cm
1	28	1.19614
2	29	1.20258
3	30	1.32047
4	31	1.34029
5	32	1.28367
6	34	1.19968

Plane no	Time, s	Bed Height, cm	Velocity, cm/s
P1-P2	1	30	30
P2-P3	1	60	30
P3-P4	1	90	30
P4-P5	1	120	30
P5-P6	2	150	15

Table E3: Axial velocity of group 3 for trickle up-flow at 6 gpm

Plane no.	Time, s	Max Conductivity, mS/cm
1	28	1.16681
2	29	1.18756
3	30	1.28343
4	31	1.29761
5	32	1.24067
6	33	1.16996

Plane no	Time, s	Bed Height, cm	Velocity, cm/S
P1-P2	1	30	30
P2-P3	1	60	30
P3-P4	1	90	30
P4-P5	1	120	30
P5-P6	1	150	30

Table E4: Axial velocity of group 4 for trickle up-flow at 6 gpm

Plane no.	Time, s	Max Conductivity, mS/cm
1	28	1.12607
2	29	1.16673
3	30	1.23699
4	31	1.24585
5	32	1.19332
6	34	1.13909

Plane no	Time, s	Bed Height, cm	Velocity, cm/s
P1-P2	1	30	30
P2-P3	1	60	30
P3-P4	1	90	30
P4-P5	1	120	30
P5-P6	2	150	15

Table E5: Axial velocity of group 5 for trickle up-flow at 6 gpm

Plane no.	Time, s	Max Conductivity, mS/cm
1	28	1.08451
2	29	1.13937
3	30	1.18928
4	31	1.19317
5	33	1.1529
6	34	1.12229

Plane no	Time, s	Bed Height, cm	Velocity, cm/s
P1-P2	1	30	30
P2-P3	1	60	30
P3-P4	1	90	30
P4-P5	2	120	15
P5-P6	1	150	30

Table E6: Axial velocity of group 6 for trickle up-flow at 6 gpm

Plane no.	Time, s	Max Conductivity, mS/cm
1	28	1.04966
2	29	1.11012
3	30	1.14601
4	32	1.15053
5	33	1.12276
6	34	1.10538

Plane no	Time, s	Bed Height, cm	Velocity, cm/s
P1-P2	1	30	30
P2-P3	1	60	30
P3-P4	2	90	15
P4-P5	1	120	30
P5-P6	1	150	30

Table E7: Axial velocity of group 7 for trickle up-flow at 6 gpm

Plane no.	Time, s	Max Conductivity, mS/cm
1	28	1.02476
2	29	1.08238
3	30	1.11028
4	32	1.12662
5	33	1.097
6	34	1.0894

Plane no	Time, s	Bed Height, cm	Velocity, cm/s
P1-P2	1	30	30
P2-P3	1	60	30
P3-P4	2	90	15
P4-P5	1	120	30
P5-P6	1	150	30

Table E8: Axial velocity of group 8 for trickle up-flow at 6 gpm

Plane no.	Time, s	Max Conductivity, mS/cm
1	28	1.00962
2	29	1.05838
3	30	1.08341
4	32	1.10814
5	33	1.07675
6	35	1.07671

Plane no	Time, s	Bed Height, cm	Velocity, cm/s
P1-P2	1	30	30
P2-P3	1	60	30
P3-P4	2	90	15
P4-P5	1	120	30
P5-P6	2	150	15

Table E9: Axial velocity of group 9 for trickle up-flow at 6 gpm

Plane no.	Time, s	Max Conductivity, mS/cm
1	27	1.00901
2	28	1.03974
3	30	1.06593
4	32	1.09639
5	33	1.06272
6	35	1.06916

Plane no	Time, s	Bed Height, cm	Velocity, cm/s
P1-P2	1	30	30
P2-P3	2	60	15
P3-P4	2	90	15
P4-P5	1	120	30
P5-P6	2	150	15

Table E10: Axial velocity of group 10 for trickle up-flow at 6 gpm

Plane no.	Time, s	Max Conductivity, mS/cm
1	27	1.01217
2	28	1.02816
3	31	1.06029
4	32	1.09423
5	33	1.05605
6	35	1.06536

Plane no	Time, s	Bed Height, cm	Velocity, cm/s
P1-P2	1	30	30
P2-P3	3	60	10
P3-P4	1	90	30
P4-P5	1	120	30
P5-P6	2	150	15

Standard deviation between ERT and LC at flow rates 3 and 6gpm for trickle down flow. Where is the estimated standard deviation.

Standard deviation between ERT and LC at 3 gpm				
Height bed, cm	Mf of LC	Mf of ERT	(Mf_1-Mf_2)	$(Mf_1-Mf_2)^2$
30	0.61	0.43	0.18	0.0324
60	0.51	0.33	0.18	0.0324
90	0.45	0.31	0.14	0.0196
sum				0.0844
N	3			
			σ_{est}	0.17

Standard deviation between ERT and LC at 6 gpm				
Height bed, cm	Mf_1 of LC	Mf_2 of ERT	(Mf_1-Mf_2)	$(Mf_1-Mf_2)^2$
30	0.571	0.33	0.241	0.058081
60	0.45	0.27	0.18	0.0324
90	0.41	0.22	0.19	0.0361
sum				0.126581
N	3			
			σ_{est}	0.21

Standard deviation of measured interstitial velocity and ERT velocity values for full liquid up flow at flow rates of 3, 6, and 9gpm.

Standard deviation of measured interstitial velocity and ERT velocity for full liquid up flow at 3 gpm				
Height bed, cm	V_1 ERT average velocity	V_2 measured velocity	(V_1-V_2)	$(V1-V2)^2$
30	1.11	0.82	0.29	0.0841
60	1.11	0.82	0.29	0.0841
90	1.11	0.82	0.29	0.0841
120	1.11	0.82	0.29	0.0841
150	1.11	0.82	0.29	0.0841
sum				0.4205
N	5		σ_{est}	0.29

Standard deviation of measured interstitial velocity and ERT velocity for full liquid up flow at 6 gpm				
Height bed, cm	V_1 ERT average velocity	V_2 measured velocity	(V_1-V_2)	$(V1-V2)^2$
30	1.96	1.64	0.32	0.1024
60	1.96	1.64	0.32	0.1024
90	1.96	1.64	0.32	0.1024
120	1.96	1.64	0.32	0.1024
150	1.96	1.64	0.32	0.1024
sum				0.512
N	5		σ_{est}	0.32

Standard deviation of measured interstitial velocity and ERT velocity for full liquid up flow at 9 gpm				
Height bed, cm	V_1 ERT average velocity	V_2 measured velocity	(V_1-V_2)	$(V1-V2)^2$
30	2.75	2.42	0.33	0.1089
60	2.75	2.42	0.33	0.1089
90	2.75	2.42	0.33	0.1089
120	2.75	2.42	0.33	0.1089
150	2.75	2.42	0.33	0.1089
sum				0.5445
N	5		σ_{est}	0.33

APPENDIX B

Sample of Calculations

Table 1 shows an example of one such table data that using in calculations for 3 gpm of full liquid up-flow that exported as numerical data in MS Excel format by using 'File/ export data' parameter in the menu bar of P2000 software window of ERT technique as shown in figure 4-9.

Table 1: Mean conductivity of group1 for trickle down-flow at 3 gpm

Time, s	G1,P1	G1,P2	G1,P3	G1,P4	G1,P5	G1,P6
1	1.00172	0.999277	1.00014	1.00125	1.0006	1.00085
2	1.00157	1.00068	0.998518	1.00056	1.00153	0.999056
3	1.00208	0.999511	0.998145	0.999537	1.00028	1.00242
4	1.00077	1.00055	1.00094	0.999797	0.998114	1.00117
5	1.00262	1.00009	0.999708	1.00044	0.999602	0.998382
6	0.997197	1.0007	0.999965	0.998726	0.99978	1.00211
7	1	1.00085	1.00157	1.00022	0.999145	1.00146
8	0.999819	0.99822	1.00197	1.00025	1.00047	1.00172
9	1.00202	0.999805	1.00014	1.00055	0.999663	1.00299
10	1.00139	0.99822	0.998903	0.99961	0.998946	1.00241
11	1.00358	0.997465	0.998641	0.999581	0.998469	1.00251
12	1.00245	1.00131	0.999919	1.00034	1.00058	1.00055
13	1.00027	1.00055	1.00201	0.999587	0.999193	1.00016
14	1.00262	0.998612	1.00025	1.00053	0.999449	0.998119
15	0.999377	1.00032	0.998591	1.00042	1.00107	1.00115
16	1.0005	0.999925	0.999961	0.999914	0.998659	1.00128
17	0.997624	1.00036	1.00091	0.999627	0.99939	1.00045
18	0.997998	1.00141	1.00002	0.99933	1.00039	1.00115
19	0.998609	0.999375	0.999247	1.00204	1.00081	1.00077
20	0.999155	1.00045	0.998657	1.00082	0.999283	1.00176
21	1.00033	0.998872	0.999446	1.00005	1.00177	1.00092
22	1.00112	0.999075	1.0005	1.00188	0.997887	1.00008
23	1.00154	1.00051	1.00087	1.00188	0.999058	1.00054
24	0.999918	0.999968	1.00083	1.0013	0.999975	0.999659
25	1.00193	0.99905	0.999262	1.00096	1.00166	1.00223
26	0.9981	0.999052	1.00034	1.00057	1.00054	1.00043
27	0.9987	0.998892	0.999472	1.00057	1.00076	0.999952

Time, s	G1,P1	G1,P2	G1,P3	G1,P4	G1,P5	G1,P6
28	0.997459	1.0005	0.999229	0.999645	0.998405	1.00203
29	0.999677	1.00128	0.999368	0.999593	0.999797	1.00141
30	0.997905	1.00013	1.0001	0.999782	1.00004	1.00006
31	0.999523	1.00228	0.999546	1.00307	1.00059	1.00177
32	1.0688	1.01173	1.00185	1.00208	1.00083	1.00356
33	1.14874	1.08874	1.01512	1.00202	1.00094	1.00223
34	1.11547	1.1914	1.06722	1.01388	1.00161	1.00279
35	1.07777	1.20783	1.17567	1.0518	1.01108	1.00183
36	1.0589	1.15951	1.23319	1.11646	1.03903	1.00908
37	1.0427	1.11296	1.21973	1.18834	1.08889	1.03658
38	1.02969	1.08761	1.17817	1.20667	1.13681	1.07613
39	1.02419	1.0663	1.1442	1.20359	1.17631	1.12158
40	1.01683	1.04732	1.10612	1.17507	1.18469	1.1456
41	1.00789	1.03668	1.07978	1.13571	1.16932	1.15432
42	1.00651	1.03029	1.06187	1.11055	1.14211	1.13601
43	1.00611	1.02578	1.04785	1.08427	1.1142	1.12045
44	1.00732	1.02205	1.03698	1.06688	1.09279	1.1042
45	1.00682	1.01968	1.03092	1.05183	1.07468	1.07758
46	1.01147	1.01534	1.02632	1.04384	1.06147	1.06059
47	1.00361	1.01339	1.023	1.03632	1.0498	1.04331
48	1.0036	1.01109	1.01906	1.02849	1.04009	1.0385
49	1.00291	1.01129	1.01658	1.02446	1.03438	1.02824
50	1.00522	1.01055	1.01341	1.02017	1.02805	1.02505
51	1.00343	1.00989	1.0129	1.01758	1.02185	1.01924
52	0.997513	1.00994	1.01214	1.01585	1.01944	1.01763
53	1.00047	1.00729	1.00995	1.01372	1.01556	1.0146
54	0.999126	1.00578	1.00762	1.01286	1.01352	1.0108
55	0.994332	1.0051	1.00955	1.00964	1.01181	1.00815
56	0.9946	1.00176	1.00581	1.01118	1.00965	1.00787
57	0.999198	1.00346	1.00536	1.00818	1.00952	1.0103
58	0.999532	1.00268	1.00422	1.00606	1.00728	1.00813
59	0.997988	1.00125	1.00318	1.00675	1.00807	1.00684
60	0.997979	1.00318	1.00417	1.00514	1.00748	1.00619
61	0.997249	0.999596	1.00293	1.00316	1.00641	1.0064
62	0.997843	1.00126	1.00208	1.0044	1.0061	1.00812
63	0.995427	1.00217	1.00285	1.0042	1.00444	1.00567
64	0.995963	0.998166	1.00231	1.00274	1.00402	1.00594
65	0.995895	1.00044	1.00132	1.00313	1.00505	1.0037
66	1.00109	1.00103	1.0022	1.00302	1.00383	1.00675
67	1.00338	1.00192	1.00118	1.00257	1.00418	1.00741

Time, s	G1,P1	G1,P2	G1,P3	G1,P4	G1,P5	G1,P6
68	1.00284	1.00364	1.00252	1.00463	1.00394	1.00688
69	1.00171	1.00345	1.0025	1.00367	1.00323	1.00583
70	1.00766	1.00246	1.00259	1.00311	1.00335	1.00665
71	1.00405	1.00236	1.00279	1.00304	1.00305	1.00588
72	0.998913	1.00252	1.00252	1.00416	1.00362	1.00444
73	1.00099	1.00194	1.00341	1.00339	1.0037	1.0015
74	1.00325	1.00264	1.00143	1.00404	1.00383	1.00233
75	1.00179	1.00215	1.0013	1.00189	1.00375	1.00345
76	1.00013	0.999925	1.00299	1.00306	1.00254	1.00303
77	1.0036	1.00162	1.00214	1.00386	1.00181	1.00261
78	1.00304	1.00332	1.00085	1.0022	1.00262	1.00105
79	1.00262	1.00125	1.00385	1.00327	1.00393	1.00316
80	1.00371	1.00236	1.00375	1.00216	1.00366	1.00192
81	1.00223	1.00368	1.00277	1.00222	1.0038	1.00239
82	1.00251	1.0044	1.00492	1.00241	1.00215	1.00113
83	1.00279	1.0023	1.00315	1.00384	1.00314	1.0018
84	1.00085	1.004	1.00324	1.00269	1.00216	1.00397
85	1.00126	1.00409	1.00311	1.004	1.00217	1.00382
86	1.00467	1.00275	1.00316	1.00272	1.00245	1.0025
87	1.00045	1.0045	1.0016	1.00329	1.00282	1.00088
88	1.00305	1.00337	1.00328	1.00183	1.00349	1.0032
89	1.00176	1.00228	1.00175	1.00218	1.00228	1.00349
90	0.999767	1.00183	1.00201	1.00169	1.00178	1.00288
91	1.0015	1.00061	1.00156	1.00162	1.00281	1.00138
92	0.996513	1.00133	1.00074	1.00284	1.00171	1.00004
93	0.998989	1.00066	1.00011	1.00131	1.00419	1.0006
94	0.997321	1.00152	1.00201	1.00154	1.00339	1.00321
95	0.999993	1.00278	1.00134	1.00201	1.00248	1.00203
96	1.00492	1.00146	1.00266	1.00282	1.00199	1.00227
97	1.00165	1.00114	1.00032	1.00179	1.00097	1.00188
98	1.00002	1.00108	1.00037	1.00117	1.00153	1.00081
99	0.99731	1.00115	1.0017	1.00184	1.00183	1.00143
100	0.998256	1.00103	0.999344	1.00175	1.0033	1.00461
101	1.00114	1.00088	1.00293	1.00202	1.00112	1.00239
102	0.997585	1.00234	1.0004	1.00274	1.00218	1.00225
103	1.00068	1.00126	1.00166	1.00179	1.00137	1.00123
104	0.999617	0.999628	1.00081	1.00222	1.00191	1.00264
105	0.996966	1.0016	0.999656	1.00195	1.00243	1.00316
106	0.998011	1.00047	1.00075	1.00189	0.999958	1.00247
107	0.998213	0.999849	1.00094	1.0028	1.00241	1.00315

Time, s	G1,P1	G1,P2	G1,P3	G1,P4	G1,P5	G1,P6
108	0.997627	0.999521	1.001	1.00271	1.00436	1.00304
109	0.999624	1.00089	1.00061	1.00155	1.00264	1.00293
110	0.994887	0.999278	1.00205	1.00186	1.00331	1.0015
111	0.994632	0.99983	1.00143	1.00215	1.00244	1.00026
112	0.992039	0.99839	1.00021	1.00286	1.00257	1.0012
113	0.995013	0.998674	1.00062	1.00194	1.00195	0.999658
114	0.994135	0.998965	0.999021	1.00161	1.00211	1.00049
115	0.994095	0.998563	0.999843	1.00189	1.00244	0.999248
116	0.997546	0.999118	1.00043	1.0012	1.00146	1.00108
117	0.998292	0.998965	0.999366	1.00308	1.00176	1.00094
118	0.994212	0.999237	0.999652	1.00218	1.00238	0.999402
119	1.00174	1.00054	0.999453	1.00223	1.00091	1.00153
120	0.998874	0.999412	0.998742	1.00143	1.00297	1.00083
121	0.999384	0.999612	0.999322	1.00265	1.00107	1.00066
122	1.0019	0.999013	0.999601	1.00198	1.00165	1.00235
123	1.00059	1.00136	1.00117	1.00204	1.00214	1.00241
124	0.999869	0.998524	1.00074	1.00234	1.00393	1.0026
125	1.00224	0.999131	0.999424	0.999871	1.0027	1.00283
126	1.00039	1.00121	0.998615	1.00227	1.00181	1.00141
127	1.00214	0.999323	0.999379	1.00216	1.00312	1.00217
128	1.00136	1.00108	1.00069	1.00332	1.00305	1.00282
129	1.00115	1.00079	1.0007	1.00274	1.00208	1.00291
130	0.9969	1.00163	0.999841	1.00374	1.00204	1.00162
131	0.997312	0.999157	1.00237	1.00104	0.999656	1.00136
132	1.00435	1.00011	0.999167	1.00271	1.00052	1.00015
133	1.00192	1.00093	1.00285	1.00228	1.00148	1.00032
134	1.0053	1.00219	1.00015	1.00356	1.00132	1.0005
135	0.99778	1.00376	1.00115	1.00118	1.00032	1.00187
136	1.00141	1.00104	1.00098	1.00312	1.00073	0.997328
137	1.0011	1.00146	1.00014	1.00238	1.00075	0.998903
138	1.00116	0.999294	1.00055	1.00157	0.999497	0.99892
139	0.997205	1.00275	1.00101	1.00224	0.999823	0.997909
140	1.00056	1.0023	1.00019	1.00239	0.999903	0.998764
141	1.00024	1.00245	1.0013	1.00302	0.998982	0.998539
142	0.999029	1.00076	1.00149	1.00201	1.00073	0.997265
143	0.998889	1.00125	1.00105	1.00308	0.999865	0.997227
144	0.993241	1.00083	1.0013	1.0039	1.00091	0.997967
145	0.991772	0.99993	1.00066	1.00196	1.00033	0.998092
146	0.993665	1.00121	0.999127	1.00233	1.00029	0.998736
147	0.992445	1.00002	1.00073	1.0025	0.999573	1.0003

Time, s	G1,P1	G1,P2	G1,P3	G1,P4	G1,P5	G1,P6
148	0.99382	0.999367	1.00061	1.00261	1.00094	0.999521
149	0.993824	0.99884	0.997963	1.00088	0.999027	1.001
150	0.994066	0.997891	0.998869	1.00192	0.998488	0.998159
151	0.992655	0.996576	0.999393	1.0029	0.999634	0.999927
152	0.993168	0.999133	1.00021	1.00227	1.00032	0.999646
153	0.993036	0.999384	0.999675	1.00153	1.00149	0.998921
154	0.992277	1.00051	0.999995	1.00194	1.00042	0.998837
155	0.992046	0.99569	0.999446	1.00188	1.00022	1.00028
156	0.991264	0.997447	1.00019	1.00048	0.998898	0.998554
157	0.993551	0.997582	1.00044	1.00218	1.0011	0.99728
158	0.99123	0.998423	0.999005	1.00257	0.9995	0.998501
159	0.992415	0.997259	0.997994	1.00035	1.00106	0.997632
160	0.993217	0.9987	1.00046	1.0022	0.999783	0.997765

Calculation of velocity using ERT

Sample of calculation for velocity of group 1 for trickle up-flow at 3 gpm

Plane no.	Time, s	Max Conductivity, mS/cm
1	33	1.14874
2	35	1.20783
3	36	1.23319
4	38	1.20667
5	40	1.18469
6	41	1.15432

Plane no	Time, s	Bed Height, cm	Velocity, cm/s
P1-P2	2	30	15
P2-P3	1	30	30
P3-P4	2	30	15
P4-P5	2	30	15
P5-P6	1	30	30

Calculation of superficial velocity and interstitial velocity

Superficial Velocity (Vs)

$$Vs = Q / A$$

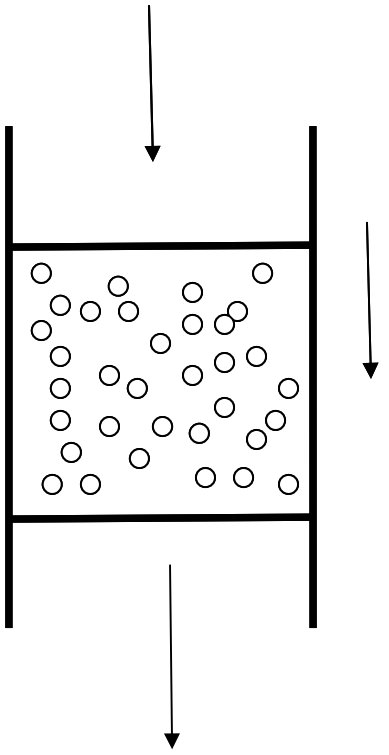

Interstitial Velocity (V)

Porosity = ϵ

$V = Vs / \epsilon$

- ✓ Q Is the measured fluid flow rate through the bed (cm^3/s)
- ✓ Column diameter = 30 cm
- ✓ A is the bed cross sectional area (cm^2) = $\pi * r^2 = 3.14 * (15)^2 = 706\ cm^2$
- ✓ Vs is the superficial velocity (cm/s)
- ✓ V is the interstitial velocity within the bed (cm/s)

Porosity calculation

1. Column was chosen with the same diameter of experimental column (30cm) with height 15cm and the volume of column (10597.5 cm^3)

2. Filled with the same packing (2.0cm plastic spheres).

4. The size of pores being invaded by water = 3500cm^3

ϵ = Volume of void-space of column / Volume of the column

= 3500 / 10597.5

= 0.33

Flow rate (gpm)	Flow rate(cm^3/S)	Vs (cm/s)	V (cm/s)
3	189.25	0.27	0.82
6	378.5	0.54	1.64
9	567.8	0.80	2.42

3 gpm/bed height= 30/t= 40s				
Cell no.	Liquid height, cm	Flow rate, cm3/s, = (h*Ac/t) = (H*16/40)	1- V_i / V_{av}	$(1-Vi/Vav)^2$
A1	2	0.8	0.56	0.31
A2	7	2.8	-0.54	0.29
A3	1	0.4	0.78	0.60
A4	5	2.0	-0.1	0.01
A5	6	2.4	-0.32	0.10
A6	1	0.4	0.78	0.60
A7	7	2.8	-0.54	0.29
A8	3	1.2	0.34	0.11
A9	8	3.2	-0.76	0.58
A10	3	1.2	0.34	0.11
A11	7	2.8	-0.54	0.29
A12	6	2.4	-0.32	0.10
A13	1	0.4	0.78	0.60
A14	2	0.8	0.56	0.31
A15	3	1.2	0.34	0.11
A16	7	2.8	-0.54	0.29
A17	5	2.0	-0.10	0.01
A18	9	3.6	-0.98	0.96
B1	5	2.0	-0.10	0.01
B2	2	0.8	0.56	0.31
B3	1	0.4	0.78	0.60
B4	5	2.0	-0.10	0.01
B5	1	0.4	0.78	0.60
B6	7	2.8	-0.54	0.29
B7	2	0.8	0.56	0.31
B8	1	0.4	0.78	0.60
B9	8	3.2	-0.76	0.58
B10	2	0.8	0.56	0.31
B11	9	3.6	-0.98	0.96
B12	4	1.6	0.12	0.01
C1	1	0.4	0.78	0.60
C2	7	2.8	-0.54	0.29
C3	8	3.2	-0.76	0.58
C4	6	2.4	-0.32	0.10
C5	9	3.6	-0.98	0.96
C6	1	0.4	0.78	0.60
D	6	2.4	-0.32	0.10
Ave		1.8		13.63

1. Sample calculation of liquid distribution factor at bed height 30 cm at flow rate 3gpm of trickle down flow using liquid collection method with experimental data of 3 and 6 gpm.

$$Mf = \left(\frac{1}{37} * \ 13.63\right)^{0.5} \quad = \ 0.60$$

2. Sample calculation of liquid distribution factor at bed height 30 cm at flow rate 3gpm of trickle down flow using electrical resistance tomography.

Group no.	Velocity, cm/s	$1- V_i / V_{av}$	$(1-Vi/Vav)^2$
G1	15	0.09	0.01
G2	15	0.09	0.01
G3	15	0.09	0.01
G4	15	0.09	0.01
G5	15	0.09	0.01
G6	10	0.39	0.16
G7	10	0.39	0.16
G8	10	0.39	0.16
G9	30	-0.81	0.67
G10	30	-0.81	0.67
Sum			1.85

$$Mf = \left(\frac{1}{10} * \ 1.85\right)^{0.5} \quad = \ 0.42$$

3. Sample calculation of standard deviation between ERT and LC at flow rate 3gpm for trickle down flow. Where σ_{est} is the estimated standard deviation.

Standard deviation between ERT and LC at 3 gpm				
Bed Height, cm	Mf of LC	Mf of ERT	$(Mf_1\text{-}Mf_2)$	$(Mf_1\text{-}Mf_2)^2$
30	0.61	0.43	0.18	0.03
60	0.51	0.33	0.18	0.03
90	0.45	0.31	0.14	0.01
sum				0.084

$$\sigma_{est} = \left(\left(\frac{\sum \quad (Mf_1 - \mathrm{Mf_2})^2}{\mathrm{N}}\right)\right)^{0.5}$$

$$\sigma_{est} = (0.084/3)^{0.5}$$

$$= 0.17$$

4. Sample calculation of standard deviation of measured interstitial velocity and ERT velocity values for full liquid up flow at 3gpm.

Standard deviation of measured interstitial velocity and ERT velocity for full liquid up flow at 3 gpm				
Height bed, cm	V_1 ERT average velocity	V_2 measured velocity	(V_1-V_2)	$(V1-V2)^2$
30	1.11	0.82	0.29	0.08
60	1.11	0.82	0.29	0.08
90	1.11	0.82	0.29	0.08
120	1.11	0.82	0.29	0.08
150	1.11	0.82	0.29	0.08
sum				0.4205
N	5		σ_{est}	0.29